NNT : 9921A41076W

THÈSE DE DOCTORAT

Soutenue à Aix-Marseille Université
le 21 Novembre 2024 par

Federica PAPPALARDO

Optical properties of tungsten under deuterium and helium plasma irradiation

Discipline
Physique et Sciences de la matière

Spécialité
Energie, rayonnement et plasma

École doctorale
ED352

Laboratoire/Partenaires de recherche
PIIM (Physique des Interactions Ioniques et Moléculaires)
ANR (Agence Nationale de la Recherche)

Composition du jury

Pere ROCA I CABARROCAS Directeur de Recherche CNRS LPICM (Ecole Polytechnique)	Rapporteur
David DELLASEGA Associate Professor NanoLab (Politecnico di Milano)	Rapporteur
Mireille RICHARD Directrice de Recherche CNRS IMN(Université de Nantes)	Presidente du jury
Laurent GALLAIS Professeur Institut Fresnel (Centrale Méditerranée)	Examinateur
Régis BISSON Maître de Conference HDR PIIM (Aix-Marseille Université)	Directeur de thèse
Marco MINISSALE Chargé de recherche HDR CNRS, PIIM (CNRS)	Co-directeur de thèse

Affidavit

I, undersigned, Federica Pappalardo, hereby declare that the work presented in this manuscript is my own work, carried out under the scientific supervision of Régis Bisson and Marco Minissale, in accordance with the principles of honesty, integrity and responsibility inherent to the research mission. The research work and the writing of this manuscript have been carried out in compliance with both the French national charter for Research Integrity and the Aix-Marseille University charter on the fight against plagiarism.

This work has not been submitted previously either in this country or in another country in the same or in a similar version to any other examination body.

Marseille, 16 septembre 2024



Cette œuvre est mise à disposition selon les termes de la Licence Creative Commons Attribution - Pas d'Utilisation Commerciale - Pas de Modification 4.0 International.

Liste de publications et/ou brevets et participation aux conférences

1) Liste des publications et/ou brevet [3] réalisées dans le cadre du projet de thèse :

   1. **F. Pappalardo**, F. Romero Lairado, C. Louis de Canonville, G. Serin, G. Giacometti, C. Martin, E. Salomon, T. Angot, L. Gallais, R. Bisson, M. Minissale, Optical properties of tungsten: a parametric study to characterize the role of roughness, surface composition and temperature, *MDPI Optics* **2022**, 3, 216-224. https://doi.org/10.3390/opt3030021
   2. M. Minissale, E. Salomon, **F. Pappalardo**, C. Martin, M. Muntwiler, T. Angot, G. Le Lay, The renaissance and golden age of epitaxial dry germanene, *MDPI Crystals* **2023**, 13, 221 (co-author) https://doi.org/10.3390/cryst13020221
   3. **F. Pappalardo**, L. Rayneau, M. Cabie, C. Martin, E. Salomon, T. Angot, G. Cartry, R. Bisson, M. Minissale, In-situ monitoring of tungsten oxides reduction during deuterium plasma exposure by spectroscopic ellipsometry, *Journal of Nuclear Materials and Energy* , vol. 41, p. 101751, 2024
   4. M. Minissale, **F. Pappalardo**, C. Martin, A. Campos, G. Cartry, M. Alfazza, Grain orientation and temperature dependence of helium-bubble bursting on tungsten surfaces upon helium plasma exposure, *Journal of Nuclear Materials and Energy* , vol. 42, p. 101883, 2025.

2) Participation aux conférences[4] et écoles d'été au cours de la période de thèse :
   1. PSI-25 International Conference on Plasma Surface Interaction in Controlled Fusion Devices, online, 2022 (poster presentation)
   2. PCAM Summer School and ECOSS 35 Conference on Surface Science, University of Luxembourg, Esch-sur-Alzette, 2022 (poster presentation)
   3. PFMC-19 International Conference on Plasma-Facing Materials and Components for Fusion Applications, FZJ, Bonn, Germany, 2023 (poster presentation)
   4. 26ème Congrès Général de la SFP, Cité de la Science et de l'Industrie, Paris, France, 2023 (poster presentation)
   5. PSI-26 International Conference on Plasma Surface Interaction in Controlled Fusion Devices, Marseille, France, 2024 (poster presentation)

[3] Cette liste comprend les articles publiés, les articles soumis à publication et les articles en préparation ainsi que les livres, chapitres de livre et/ou toutes formes de valorisation des résultats des travaux propres à la discipline du projet de thèse. La référence aux publications doit suivre les règles standards de bibliographie et doit être conforme à la charte des publications d'AMU.

[4] Le terme « conférence » est générique. Il désigne à la fois « conférence », « congrès », « workshop », « colloques », « rencontres nationales et/ou internationales » … etc.

Indiquer si vous avez fait une présentation orale ou sous forme de poster.

6. 19th Hydrogen Workshop, Chamonix, France, 2024 (oral presentation)
7. 19ème Journées de la Matière Condensée, Marseille, France, 2024 (oral presentation)

Abstract

The surface temperature measurement of plasma-facing components (PFCs) is a crucial issue in a tokamak environment like ITER, as it relies on non-contact optical diagnostics (pyrometers and IR cameras) whose response is based on the accurate knowledge of the material's optical properties (such as emissivity and reflectivity). Such optical properties depend on multiple factors such as the surface state (e.g., the roughness) or the chemical composition of the studied materials. In the divertor region of ITER, where PFCs are made of tungsten (W), the high heat and high fluxes of low energy (<50 eV) particles will surely induce material modifications, which can then evolve upon thermal annealing (<1273 K). In particular, deuterium (D) ions should have a milder effect on W morphology and can also rise fuel retention problems, while helium (He) ions are known to create more damage, in particular by forming sub-surface voids (so-called He bubbles) and increasing W surface roughness. It is therefore of fundamental importance, in order to retrieve accurate thermography measurements, to evidence the changes of W optical properties due to the morphological and structural modifications induced by plasma-wall interactions.

In this PhD thesis, we aim to monitor W surface evolution in-situ and in real time during plasma exposure, using optical diagnostic (mainly spectroscopic ellipsometry) in the optical range 400-1000 nm. During the first year of the PhD, we performed a preliminary study to characterize the role of roughness on the reflectivity of W samples while simultaneously heating them. The samples roughness was tailored ad-hoc by chemical etching, in order to simulate the effect induced by He plasmas on W without directly exposing the samples. As expected, we found a lower specular reflectivity with increasing roughness and higher reflectivity upon multiple annealing cycles up to 1073 K. This reflectivity increase is attributed to native oxide reduction and chemical impurities desorption (measured with XPS). During the second year, we passed to a proper plasma exposure, starting with a D plasma, as the interaction of D ions with W is not supposed to induce a considerable roughness variation. We observe an increase of W reflectivity during plasma exposure, and we attribute such evolution to the presence of trapped D. Coupling ellipsometry results and macroscopic rate equations models we eventually estimate the amount of D trapped in the sub-surface.

In addition, as surface oxide growth on W PFCs at high temperatures rises concerns on their lifetime, we also perform ellipsometry measurements on W oxide layers thermally grown on W. We observe that the synergistic effect of temperature and plasma irradiation determines the oxide evolution, leading to a more or less pronounced oxide reduction by D ions. With ellipsometry, we observe the change of the oxide optical constants n,k and in particular an increase of the extinction coefficient k towards value typical of a metal. By coupling those results to ex-situ techniques (FIB-SEM and XPS), we find that the extension in depth of such oxide reduction strongly depends on the temperature conditions during plasma, and that ellipsometry manages to highlight the oxygen depletion of the near-surface even when it is below the resolution of microscopy techniques (<5 nm).

Eventually, during the last year of PhD, we studied W reflectivity evolution during He plasma exposure, creating the experimental conditions known to produce defects (in particular, He bubbles) and roughness evolution in W. The evolution of opti-

cal properties and surface morphology is measured during plasma exposure by in-situ spectroscopic ellipsometry and is used to gain insight on the kinetics of bubbles growth. Performing exposures at different temperatures and ion fluxes, from ex-situ microscopy analysis (SEM) we observe bigger bubbles size with increasing temperature, and bubbles density that varies with W crystal orientation. We also find that ion flux does not play a big role in determining the bubbles size, while surface state of the sample (previous recrystallization or not) does. We try to reconstruct the kinetics of He bubbles formation by modelling ellipsometry data with an effective-medium approximation (EMA) layer, which describes the surface porous layer where He bubbles are created. We model the temporal evolution of bubbles fraction in the layer as well as surface roughness, which we compare with the experimental values measured with ex-situ microscopy.

Résumé

La mesure de la température de surface des composants face au plasma (PFC) est un enjeu crucial dans un environnement tokamak comme ITER, car elle repose sur des diagnostics optiques sans contact (pyromètres et caméras IR) dont la réponse est basée sur la connaissance précise des propriétés optiques du matériau (comme l'émissivité et la réflectivité). De telles propriétés optiques dépendent de multiples facteurs tels que l'état de surface (par exemple, la rugosité) ou la composition chimique des matériaux étudiés. Dans la région du divertor d'ITER, où les PFC sont en tungstène (W), la chaleur élevée et les flux élevés des particules de faible énergie (<50 eV) induiront sûrement des modifications, qui pourront ensuite évoluer lors du recuit thermique (<1273 K). En particulier, les ions de deutérium (D) auraient un effet plus modéré sur la morphologie du W et pourraient également augmenter les problèmes de rétention de carburant, tandis que les ions d'hélium (He) sont connus pour créer plus de dommages, notamment en formant des trous sous la surface (appelés bulles d'He) et en augmentant la rugosité de la surface du W. Il est donc d'une importance fondamentale, afin d'obtenir des mesures thermographiques précises, de mettre en évidence les changements des propriétés optiques du W dus aux modifications morphologiques et structurelles induites par les interactions plasma-paroi. Dans cette thèse de doctorat, nous visons à suivre l'évolution de la surface du W in situ et en temps réel pendant l'exposition au plasma, en utilisant un diagnostic optique (principalement l'ellipsométrie spectroscopique) dans la gamme optique 400-1000 nm. Au cours de la première année de doctorat, nous avons réalisé une étude préliminaire pour caractériser le rôle de la rugosité sur la réflectivité des échantillons de W tout en les chauffant simultanément. La rugosité des échantillons a été ajustée ad-hoc par gravure chimique, afin de simuler l'effet induit par les plasmas He sur W sans exposer directement les échantillons. Comme prévu, nous avons trouvé une réflectivité spéculaire plus faible avec l'augmentation de la rugosité et une réflectivité plus élevée lors de multiples cycles de recuit jusqu'à 1073 K. Cette augmentation de la réflectivité est attribuée à la réduction de l'oxyde natif et à la désorption des impuretés chimiques (mesurée avec XPS). Au cours de la deuxième année, nous passons à une exposition au plasma, en commençant par un plasma D, car l'interaction des ions D avec W n'est pas censée induire une variation considérable de la rugosité. Nous observons une augmentation de la réflectivité du W pendant l'exposition au plasma, et nous attribuons cette évolution à la présence de D piégé. En couplant les résultats de l'ellipsométrie et les modèles d'équations macroscopiques, nous estimons finalement la quantité de D piégé dans la sous-surface. De plus, comme la croissance d'oxyde de surface sur les PFC W à haute température soulève des questions sur leur durée de vie, nous effectuons également des mesures d'ellipsométrie sur des couches d'oxyde W développées thermiquement sur W. Nous observons que l'effet synergétique de la température et de l'irradiation plasma détermine l'évolution de l'oxyde, conduisant à une réduction d'oxyde plus ou moins prononcée par les ions de D. Avec l'ellipsométrie, nous observons le changement des constantes optiques n,k de l'oxyde et en particulier une augmentation du coefficient d'extinction k vers une valeur typique d'un métal. En couplant ces résultats à des techniques ex-situ (FIB-SEM et XPS), nous constatons que l'extension en profondeur de cette réduction d'oxyde dépend fortement des conditions de température pendant

le plasma, et que l'ellipsométrie parvient à mettre en évidence l'appauvrissement en oxygène de la surface proche même lorsqu'il est inférieur à la résolution des techniques de microscopie (<5 nm). Finalement, au cours de la dernière année de thèse, nous avons étudié l'évolution de la réflectivité du W pendant l'exposition au plasma d'He, créant les conditions expérimentales connues pour produire des défauts (en particulier, des bulles d'He) et l'évolution de la rugosité dans le W. L'évolution des propriétés optiques et de la morphologie de surface est mesurée pendant l'exposition au plasma par ellipsométrie spectroscopique in situ et est utilisée pour obtenir un aperçu de la cinétique de la croissance des bulles. En effectuant des expositions à différentes températures et flux ioniques, à partir d'une analyse par microscopie ex situ (SEM), nous observons des bulles de plus en plus grosses avec l'augmentation de la température, et une densité de bulles qui varie avec l'orientation du cristal W. Nous constatons également que le flux ionique ne joue pas un grand rôle dans la détermination de la taille des bulles, alors que l'état de surface de l'échantillon (recristallisation antérieure ou non) le fait. Nous essayons de reconstruire la cinétique de formation des bulles d'He en modélisant les données d'ellipsométrie avec une couche d'approximation du milieu effectif (EMA), qui décrit la couche poreuse de surface où les bulles d'He sont créées. Nous modélisons l'évolution temporelle de la fraction de bulles dans la couche ainsi que la rugosité de surface, que nous comparons aux valeurs expérimentales mesurées par microscopie ex-situ.

Résumé étendu

Le besoin de fournir des alternatives aux combustibles fossiles devient de plus en plus urgent. Bien que d'énormes progrès aient été réalisés dans les domaines des sources renouvelables telles que l'énergie solaire, éolienne et hydrothermale, elles ne sont toujours pas en mesure de fournir une densité énergétique élevée de manière constante. La fusion nucléaire consiste à combiner des noyaux légers pour former des noyaux plus lourds et libérer de l'énergie. Pour réaliser les réactions de fusion sur Terre, l'une des idées est de développer des réacteurs pour confiner un plasma à l'aide de champs magnétiques et atteindre les conditions physiques nécessaires pour déclencher la fusion. La réaction de fusion qui combine une section efficace élevée avec une faible énergie d'entrée est la réaction deutérium-tritium (D-T), se produisant entre les deux isotopes lourds de l'hydrogène, qui produit des particules α de 3,5 MeV ($^4He^{2+}$) et des neutrons de 14 MeV:

$$D^+ + T^+ \rightarrow^4 He^{2+} + n \tag{1}$$

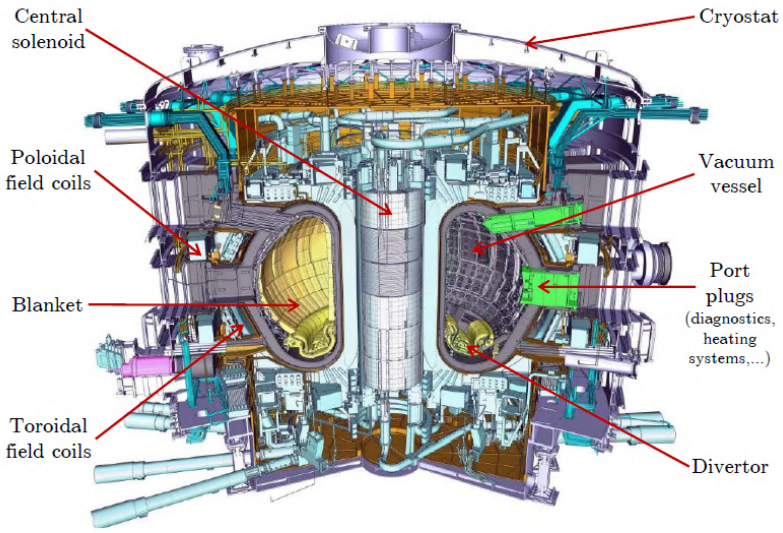


Figure 1: Représentation schématique des composants du tokamak ITER.

Les combustibles nécessaires à la réaction sont disponibles sur Terre et théoriquement inépuisables. Le deutérium peut être extrait de l'eau par distillation, tandis que le tritium est un isotope rare de l'hydrogène (avec une proportion naturelle de 10^{-18}) et est radioactif. Mais parmi les objectifs de la fusion nucléaire par réaction D-T, il y a aussi la génération du tritium basée sur l'interaction entre les neutrons de fusion et le lithium, disponible en grande partie dans l'eau de mer, qui sera présent sur les parois de la machine. La réaction D-T ne génère ni gaz à effet de serre ni déchet radioactif à long terme. Sa sécurité vient du fait que, même en cas d'accident, le plasma se refroidit et la réaction s'arrête.

Dans la réaction de fusion décrite ci-dessus, les neutrons, qui transportent 80% de l'énergie, quittent le plasma sans interagir avec lui et convertissent l'énergie en chaleur dans le système de couverture de génération. Les particules α peuvent transférer

leur énergie au plasma par collisions. La réaction de fusion devient auto-entretenue lorsque toutes les pertes d'énergie sont compensées par l'échauffement des particules α et qu'un chauffage externe n'est pas nécessaire (on parle alors de "plasma brûlant"). La condition pour un plasma auto-entretenu (ou "allumage") est décrite par le critère de Lawson, résumé par le triple produit suivant :

$$n_i \cdot T_i \cdot \tau > 5 \cdot 10^{21} keV \cdot s \cdot m^{-3} \tag{2}$$

où n_i est la densité ionique (en m^{-3}), T_i est la température du plasma (en keV) et τ est le temps de confinement de l'énergie (en s). Pour réaliser cette condition, plusieurs combinaisons des trois quantités sont théoriquement possibles. L'une se rencontre dans le cœur des étoiles et consiste en des n_i et τ très élevés, qui permettent à la réaction d'avoir lieu à un T_i relativement faible. Dans les dispositifs de confinement inertiel, une cible combustible est chauffée et comprimée par des impulsions laser ultra-courtes à haute énergie, pour obtenir des n_i et T_i élevés avec un τ court. Enfin, dans les dispositifs de confinement magnétique que nous avons décrits jusqu'à présent, des champs magnétiques sont utilisés pour maintenir un plasma avec des n_i relativement faibles, des T_i et τ élevés (dans ITER, par exemple, n_i=10^{20} m^{-3}, T_i= 8 keV dans le cœur, et τ est de quelques s).

Parmi les différentes configurations de dispositifs de fusion à confinement magnétique, la plus courante est le tokamak, qui signifie chambre toroïdale avec bobines magnétiques. Les bobines toroïdales créent un champ magnétique en forme de tore qui confine les particules de plasma à l'intérieur de la chambre à vide. Dans une telle configuration, les ions et les électrons ont tendance à diverger et le plasma est poussé vers l'extérieur. C'est pourquoi un champ poloïdal est ajouté en faisant passer un courant à travers le plasma, généré par le solénoïde central, ce qui rend les lignes de champ magnétique hélicoïdales. Cette configuration donne lieu à un mode de fonctionnement pulsé car il repose sur la génération de courant par le solénoïde central, qui peut généralement supporter des décharges allant jusqu'à plusieurs centaines de s. Enfin, les bobines poloïdales extérieures sont utilisées pour définir la position et la forme du plasma. La perte de confinement magnétique (qui peut survenir pour de multiples raisons, par exemple la perte de chaleur causée par la présence d'impuretés dans le plasma) est appelée disruption. Le principal défi et la complexité de la configuration du tokamak sont d'optimiser les performances du plasma tout en minimisant les pertes de confinement magnétique.

ITER (figure 1) est un réacteur de type tokamak qui est en cours de construction dans le sud de la France, après un accord signé en 1986 par l'Union européenne, le Japon, l'Union soviétique et les États-Unis, et qui regroupe aujourd'hui 35 nations avec l'objectif commun de démontrer la faisabilité scientifique et technique de la fusion nucléaire contrôlée. L'objectif final d'ITER est de produire un plasma avec une amplification de puissance Q>10 (où Q est le rapport entre la puissance de sortie et la puissance d'entrée). Jusqu'à présent, seule la condition Q<1 a été atteinte par certains réacteurs actuels tels que JET (Joint European Torus) et TFTR (Tokamak Fusion Test Reactor).

Les principaux composants du tokamak ITER sont représentés sur la figure 1. La cuve à vide est une chambre métallique toroïdale en acier inoxydable, contenant un divertor et une couverture. Le divertor est situé au fond de la cuve et extrait la chaleur et les particules produites par la réaction de fusion (particules α transportées par le

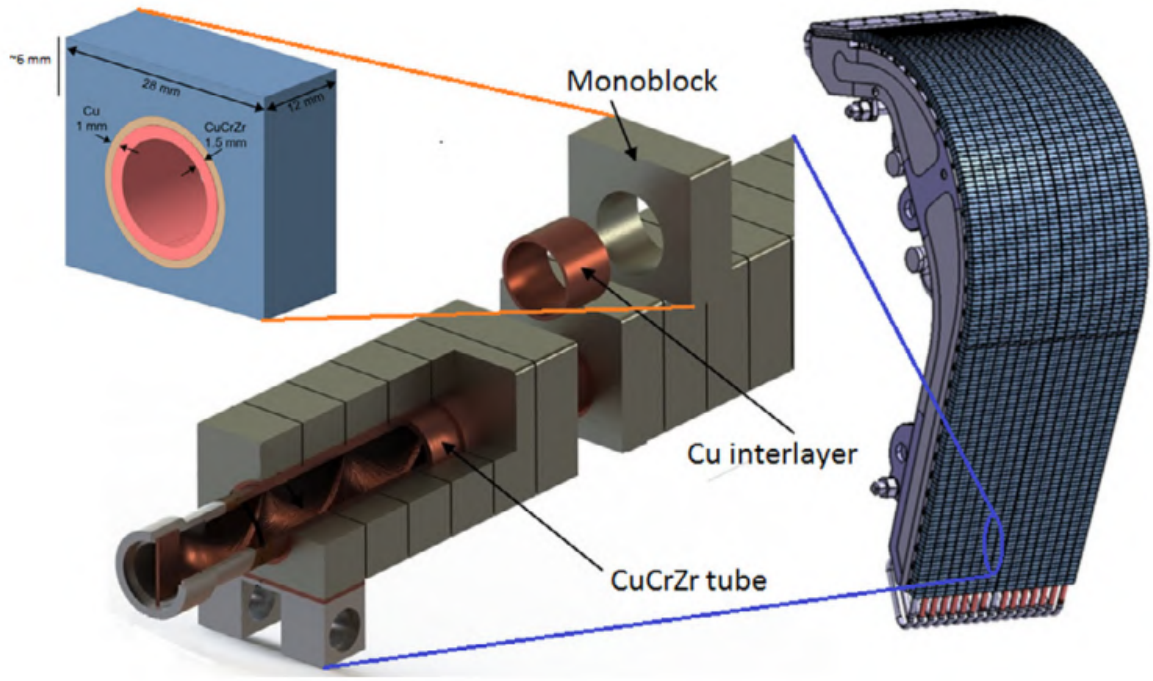


Figure 2: Représentation schématique d'un monoblock en W, sa taille caractéristique et sa position dans la structure du divertor.

plasma), les particules de combustible n'ayant pas subi de réaction de fusion et les impuretés du cœur du plasma. Le divertor est composé de 54 cassettes fabriquées à partir de monoblocs en tungstène (W) (figure 2). Chaque monobloc contient un tube CuCrZr recouvert d'une couche de Cu pour un refroidissement actif par un fluide caloporteur, qui transférera la chaleur radiative et neutronique aux tours de refroidissement d'ITER. La cuve à vide est recouverte d'une couverture qui était initialement censée être en béryllium (Be), grâce à ses propriétés de faible contamination du plasma, de rétention du combustible et d'activation des neutrons. Pour des raisons de sécurité et de toxicité, le Be est toutefois remplacé par le W. Il sera refroidi pour le transfert de chaleur (80 % de l'énergie de fusion totale transportée par les neutrons) vers les tours de refroidissement d'ITER.

Le choix des composants face au plasma (PFC) est d'une importance cruciale pour maximiser les performances du plasma et assurer le bon fonctionnement de la machine. A l'origine, ce choix pour les composants du divertor s'est orienté vers des matériaux à faible numéro atomique (Z), principalement le carbone, en raison de leurs propriétés avantageuses, telles qu'une faible contamination du plasma. Le carbone, en particulier, a été choisi pour son point de sublimation élevé (> 3900 K), permettant aux PFC de résister à des charges thermiques élevées, ainsi qu'une bonne tolérance du plasma aux impuretés de carbone. Cependant, le principal problème du carbone est l'érosion chimique, qui est élevée même à faible énergie des particules incidentes. De plus, dans les couches co-déposées d'isotopes d'hydrogène (HI)-carbone, la rétention de combustible augmente, ce qui soulève des questions de sûreté nucléaire concernant le piégeage du tritium. Pour toutes ces raisons, le choix du carbone pour les PFC des divertors a été mis de côté et les efforts de la communauté se sont plutôt concentrés sur les matériaux à haut Z, en particulier sur la catégorie des métaux réfractaires, proposée

pour la première fois en 1992. Le choix du tungstène (W) comme PFC vient de sa faible pulvérisation chimique et physique, ainsi que de sa faible rétention de combustible par rapport aux matériaux à bas Z tels que le carbone et le béryllium. Il a également la température de fusion la plus élevée ($\simeq$3687 K) parmi les métaux réfractaires, et possède une conductivité thermique et une résistance mécanique élevées. Cependant, le W est cassant à température ambiante, avec le risque possible de créer des microfissures pendant le processus de fabrication ou pendant le fonctionnement du plasma. De plus, il a une forte affinité chimique avec l'oxygène, ce qui pose des problèmes concernant l'oxydation des PFC en W (en particulier à haute température). De plus, l'interaction avec les ions hélium (He) peut modifier de manière significative la morphologie de surface du W, avec des conséquences possibles sur la rétention des HI.

Dans la région du divertor d'ITER, les flux ioniques et neutres attendus seront de l'ordre de $\simeq 10^{24}$ particules $m^{-2}s^{-1}$. Considérant une décharge de 400 s, la fluence de particules pour chaque décharge sera de $\geq 10^{26}$ particules m^{-2}. L'énergie cinétique de l'ion incident devrait être comprise entre 10 et 100 eV, tandis que la température de surface sera comprise entre 800 et 1300 K. Les principales impuretés devraient être : l'oxygène (impureté dominante), l'eau (eau lourde, eau tritiée), le carbone (<1,5%). Dans le contexte de la fusion nucléaire, des avancées scientifiques sont nécessaires dans plusieurs domaines, notamment les matériaux résistants aux radiations capables de fonctionner à haute température et le développement de diagnostics in situ compatibles et fiables. La surveillance des PFC pendant les opérations plasma doit prendre en compte leurs modifications de surface dues aux flux intenses d'éléments légers, tels que HI et He, ainsi que les neutrons, les impuretés et l'oxydation possible. En particulier, étant donné qu'ITER et de nombreux autres dispositifs de fusion évoluent vers des composants métalliques de première paroi, mener de telles études sur des matériaux comme le W dans une gamme plus large de températures et d'énergies devient de plus en plus urgent et essentiel.

Les diagnostics *in-situ* et en temps réel jouent un rôle essentiel dans la surveillance des processus d'interaction plasma-paroi, tels que l'érosion et la redéposition, qui soulèvent de graves problèmes car ils peuvent réduire la durée de vie des PFC et augmenter la rétention du combustible et la contamination du plasma. De plus, comme le plasma modifie continuellement la surface, de nouveaux défauts sont créés dans le matériau qui peuvent modifier la rétention HI. Pour les machines qui reposent sur un mélange de D et de T, la perméation de T à travers les matériaux pose d'important questions de sécurité nucléaire. La mise en œuvre des diagnostics in situ est difficile dans les conditions du tokamak car la plupart des techniques ne sont pas compatibles avec l'environnement typique des dispositifs de confinement magnétique, ce qui rend nécessaire l'extraction du matériau exposé de la machine et la réalisation d'une analyse post mortem à l'aide de méthodes ex situ. Pour le moment, les diagnostics in situ les plus fiables sont principalement des techniques optiques et laser. Les exemples incluent la spectroscopie d'ablation induite par laser (LIBS) et la spectroscopie de désorption induite par laser (LIDS), qui permettent d'analyser la composition de surface et la rétention d'HI localement, car la zone d'interaction laser-surface typique est de l'ordre d'un millimètre ou moins.

Un point crucial pour assurer la durée de vie des PFC ainsi que leur bon fonctionnement en cours d'exploitation est la mesure de leur température de surface, réalisée grâce à des diagnostics optiques sans contact (la figure 3 représente une partie du diag-

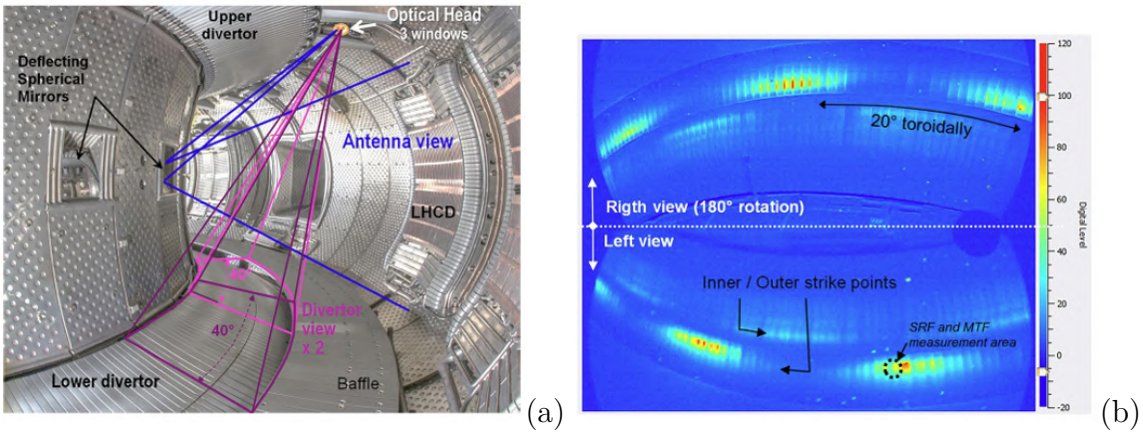


Figure 3: Lignes de vue de l'endoscope supérieur dans le tokamak WEST (a) et image IR de la zone du divertor lors d'une décharge plasma (b).

nostic optique du tokamak WEST, situé dans le sud de la France). De tels instruments (pyromètres, caméras IR) sont capables de reconstituer en temps réel la distribution des charges thermiques sur des monoblocs de PFC en W pendant la décharge et de surveiller avec précision la température des PFC à partir du rayonnement émis. Pour cette raison, il est d'un intérêt fondamental d'accroître la connaissance de l'émissivité de surface des PFC, qui dépend de plusieurs facteurs tels que la longueur d'onde et la température ainsi que des conditions de surface (rugosité, fissure, présence de contaminants).

Dans cette thèse, nous utilisons des expériences de laboratoire qui incluent des expositions au plasma et des techniques optiques, afin d'étudier l'interaction fondamentale entre la surface du W et les ions (D et He) provenant du plasma. L'objectif de la thèse est de prouver la faisabilité et l'avantage de l'utilisation de techniques optiques (à la fois ex-situ et in-situ pendant le plasma) pour obtenir un aperçu de l'interaction plasma-paroi indirectement à partir des propriétés optiques.

Pour commencer, le chapitre 2 donne un aperçu des méthodes expérimentales et des modèles théoriques utilisés pendant les trois années du doctorat pour réaliser nos études. Ensuite, le travail peut être vu comme composé de trois études logiquement consécutives, chacune réalisée chaque année du doctorat :

- Au chapitre 3, une première étude préliminaire a été réalisée avant l'exposition au plasma, en effectuant une mesure directe de la réflectivité du W dans des conditions contrôlées, en simulant l'effet de l'irradiation au plasma He (augmentation de la rugosité) en adaptant de manière *ad-hoc* la rugosité de surface par gravure chimique. De cette manière, il a été possible de réaliser une étude paramétrique sur l'évolution de la réflectivité du W avec la température (au cours de multiples cycles de recuit, dans la gamme 300-1073 K) et en fonction d'une rugosité contrôlée (dans la gamme 20-100 nm).

- L'étude suivante, discutée au chapitre 4, a été réalisée en utilisant une technique optique *in-situ* (ellipsométrie spectroscopique) afin de suivre l'évolution de la surface du W lors de l'exposition au plasma. Nous effectuons quelques premières expériences en utilisant du plasma D, car, dans nos gammes de travail d'énergie ionique, de flux et de température, il n'est pas supposé induire de changements

considérables dans la morphologie de surface. De cette manière, nous avons pu nous concentrer sur la modification de la réponse électronique et optique du W en raison de l'effet combiné de l'augmentation de la température (jusqu'à 600 K) et de l'interaction avec les ions D. En particulier, en utilisant un modèle de migration d'HI dans W, nous avons pu étudier la rétention sous-surface de D en fonction de la température, et la comparer à la variation de réflectivité mesurée par ellipsométrie.

- Le chapitre 5 contient une étude parallèle à celle décrite au chapitre 4, également réalisée au cours de la deuxième année. Elle consistait en la croissance thermique de couches d'oxydes W sur des substrats W et leurs mesures ellipsométriques *in-situ* lors de l'exposition au plasma D. L'intérêt d'étudier les oxydes W exposés au plasma dans le contexte de la fusion nucléaire est élevé et sera discuté en profondeur au chapitre 5. Le point principal ici est à nouveau de prouver l'efficacité des diagnostics optiques *in-situ* pour surveiller l'évolution de surface causée par l'interaction plasma. En particulier, nous avons constaté que l'ellipsométrie était capable de détecter la réduction de la couche d'oxyde induite par les ions D et de sonder la présence d'une couche enrichie en W à la surface à laquelle les techniques de microscopie *ex-situ* n'étaient pas sensibles.

- La dernière étude, décrite au chapitre 6 et réalisée au cours de la dernière année de la thèse, a consisté à effectuer des mesures ellipsométriques *in-situ* dans des conditions réalistes d'exposition au plasma d'He, où la morphologie de surface du W est fortement modifiée par l'interaction avec les ions He (création de bulles d'He surpressurisées, augmentation de la rugosité). En particulier, à partir de la diminution de la réflectivité observée lors de l'exposition au plasma, nous avons pu reconstruire la cinétique de formation des bulles d'He et l'évolution temporelle de la rugosité de surface en modélisant les données *in-situ* avec une couche poreuse adéquate. Nous validons nos résultats avec l'utilisation de la microscopie *ex-situ* réalisée sur les échantillons exposés, afin de mesurer la taille et la densité des bulles d'He éclatées à la surface.

Nous reviendrons brièvement sur les acquis de cette étude et esquisserons enfin quelques perspectives pour les travaux futurs.

Dans le chapitre 3, nous avons mené une étude paramétrique de la réflectivité du W en fonction de la rugosité et de la température. Comme il s'agissait d'un travail préliminaire avant une exposition au plasma, nous avons décidé de contrôler la variation de rugosité par gravure chimique, afin de simuler l'effet d'augmentation de la rugosité de l'irradiation He sur le W. Ensuite, nous avons mesuré la variation de réflectivité en fonction de la température dans la gamme 300-1000 K au cours de plusieurs cycles de recuit, pour différents échantillons avec une rugosité croissante dans la gamme 20-100 nm. De plus, des techniques de microscopie ex-situ (microscopie confocal, microscopie à force atomique) ont été utilisées pour mesurer la rugosité avant et après les cycles de recuit. Nous avons examiné la réflectivité avant et après les cycles de recuit et avons constaté une augmentation de 5-10%. Nous avons ajusté les données expérimentales avec le modèle Bennet-Porteus, qui prédit le comportement de la réflectivité en fonction de la longueur d'onde et de la rugosité, y compris la contribution des

composantes spéculaires et diffuses, dans la limite où $\sigma << \lambda$ (rugosité beaucoup plus faible que la longueur d'onde). Par conséquent, nous avons trouvé une plus grande divergence dans le comportement spectral de la réflectivité pour les échantillons les plus rugueux, où la rugosité commence à devenir du même ordre que la longueur d'onde utilisée et des modèles plus complexes sont nécessaires. Étant donné que les techniques de microscopie n'ont mis en évidence aucune variation de rugosité avant et après le recuit, nous avons utilisé la technique XPS (Spectroscopie Photoélectronique X) pour détecter tout changement dans la composition de la surface. En effet, le XPS des échantillons après recuit a montré une diminution considérable des contaminants (potassium et azote, provenant de la solution de gravure) et une réduction constante de l'oxyde natif, visible par la prédominance des pics métalliques W 4f. Par conséquent, nous expliquons l'augmentation de la réflectivité comme une conséquence du nettoyage de surface causé par le recuit, et concluons que la variation de rugosité a peu d'effet sur le changement de réflectivité dans cette gamme de température.

Au chapitre 4, nous effectuons les premières mesures d'ellipsométrie *in-situ* sur W exposé à un plasma D, afin de mieux nous entraîner à la technique et de nous préparer à des expositions plus sévères (plasma He), car les ions D ne sont pas censés induire un changement important de la morphologie du W. Ici, nous avons constaté une augmentation de la réflectivité du W pendant le plasma D d'environ 3,5% à 850 nm. Comme la température de surface du W, surveillée en même temps avec un pyromètre, a augmenté jusqu'à 600 K à cause du plasma, suivant la même tendance du signal optique, nous avons effectué quelques étalonnages afin de quantifier les contributions de la température et de l'exposition aux ions D à la variation de la réflectivité totale pendant le plasma. Nous avons ensuite utilisé l'ellipsométrie pour mesurer la variation de réflectivité pendant le recuit, soit avec un four et avec un laser de forte puissance, et avons soustrait cette contribution de la température à la variation de réflectivité observée pendant le plasma, en supposant que le résultat de cette soustraction est l'effet des ions D dans le changement de réflectivité (donc en supposant que les deux effets s'additionnent). En regardant la variation de réflectivité due à l'exposition aux ions D en fonction de la longueur d'onde, nous avons observé qu'elle est maximale à 850 nm tout comme la contribution de la température, suggérant que les deux effets ont la même nature, en particulier ils modifient les interactions phonon-électron contribuant à modifier la fonction diélectrique du W. Nous avons également examiné la variation de réflectivité pendant l'exposition au plasma. Ici, nous observons une croissance rapide dans la première minute de l'exposition, où elle atteint un maximum à 410 K. Ensuite, l'effet des ions de D diminue et est contrebalancé par l'augmentation de la température. Afin d'obtenir plus d'informations sur l'absorption et la désorption des atomes de D à la surface, nous avons utilisé le code MHIMS pour modéliser la rétention de D (concentration d'atomes de D retenus dans le matériau) pendant l'exposition au plasma. Pour pouvoir comparer ces résultats avec les données ellipsométriques, qui dépendent des propriétés d'absorption de la lumière du matériau considéré, ici le W, nous avons modélisé la rétention de D proche de la surface, c'est-à-dire la concentration d'atomes de D retenus dans les 25 premiers nm de la surface (profondeur de pénétration au premier ordre de la lumière à 850 nm dans le W). Ici, nous avons observé une assez bonne concordance entre le modèle et les données ellipsométriques, car l'inventaire de surface de D est maximal dans

la première minute de l'exposition au plasma (à 410 K) après quoi il diminue par un effet combiné de désorption induite thermiquement et de diffusion en volume des atomes de D.

Dans le chapitre 5, nous consacrons un peu de temps à la synthèse et à la caractérisation de couches épaisses (> 50 nm) d'oxyde de W développées thermiquement sur des substrats de W. La présence de couches d'oxyde soulevant des questions sur la durée de vie des PFC à l'intérieur du tokamak et sur une éventuelle contamination du plasma, nous utilisons l'ellipsométrie in situ pendant l'exposition au plasma de D couplée à des caractérisations ex situ pour évaluer tout changement dans l'état de surface de l'oxyde causé par l'irradiation au plasma de D. Les mesures optiques ont mis en évidence un changement substantiel des constantes optiques n et k de l'oxyde, qui après exposition prennent des valeurs typiques d'une surface métallique. Cela suggère une réduction générale des oxydes de W par les ions de D, ce qui a également été confirmé par des techniques ex situ (FIB-SEM) et que nous attribuons à un processus de pulvérisation chimique, puisque nous effectuons l'exposition à des énergies ioniques d'environ 15 eV (bien en dessous du seuil de pulvérisation). De plus, la réduction des oxydes est un processus thermiquement favorisé, clairement visible à partir des mesures FIB-SEM uniquement dans le cas des oxydes irradiés à haute température (650 K). Pour les oxydes irradiés avec du plasma D à basse température (373 K), le FIB-SEM n'a détecté aucun changement dans la morphologie des oxydes, alors que l'ellipsométrie et le XPS ont montré les caractéristiques typiques d'un processus de réduction des oxydes, respectivement une augmentation du coefficient d'extinction k et une prédominance des pics métalliques W 4f sur ceux des oxydes, suggérant que de tels changements se produisent dans la couche proche de la surface ($\simeq$5 nm) qui est proche de la résolution du FIB-SEM. Nous avons alors conclu que la température a également un effet sur l'extension en profondeur de la réduction des oxydes, et que l'ellipsométrie in situ peut être un outil utile pour la détecter même lorsqu'elle est inférieure à la résolution des techniques de microscopie ex situ telles que le FIB-SEM.

Dans le chapitre 6, nous effectuons enfin des mesures d'ellipsométrie in situ de W pendant l'exposition au plasma d'He, dans des conditions similaires à l'environnement hostile du divertor du tokamak, dans lesquelles nous nous attendons à un changement cohérent de la morphologie de surface de W en raison des dommages induits par He (en particulier, à des températures <1000K, où nous nous attendons à la formation de bulles d'He). L'objectif est d'utiliser l'ellipsométrie pour étudier la cinétique de formation des bulles d'He et l'évolution de la rugosité de surface. Dans ce cas également, la microscopie ex situ des échantillons exposés est systématiquement couplée aux mesures in situ. Nous effectuons des expositions au plasma d'He en modifiant différents paramètres, à savoir la température, le flux ionique et l'état de surface précédent du W. L'ellipsométrie in situ couplée aux mesures SEM des surfaces irradiées montre une diminution de la réflectivité du W pendant l'exposition au plasma d'He. En particulier, cette diminution est plus élevée avec l'augmentation de la température, passant de 2% à 673 K à 14% à 973 K, et la taille des bulles d'He suit également cette tendance (passant de 1-5 nm à 673 K à 20-25 nm à 973 K). De plus, augmenter le flux ionique d'un facteur 2 ne change pas beaucoup la variation de réflectivité ainsi

que la taille des bulles. Enfin, effectuer l'exposition sur une surface W préalablement recristallisée entraîne une diminution plus faible de la réflectivité ainsi que des bulles d'He plus petites. Nous modélisons les données *in-situ* avec une couche poreuse (EMA) représentant la couche proche de la surface des échantillons exposés contenant des bulles d'He, en considérant également la rugosité de la surface. Nous supposons que l'évolution de la porosité (fraction volumique des bulles d'He sur la couche poreuse) et de la rugosité de surface dépend d'une loi d'Arrhenius, elle est donc activée thermiquement et l'énergie d'activation du processus correspond à l'énergie de liaison des clusters d'He à une lacune (formation de bulles). Le modèle présente un bon accord qualitatif avec les données expérimentales, en utilisant une énergie de liaison de 1,2 eV pour tous les échantillons (sauf celui recristallisé, pour lequel nous avons utilisé une énergie de liaison de 1,3 eV) et en supposant une erreur de $\pm$30 K sur les valeurs de température. Nous avons ensuite comparé les résultats de l'ajustement avec les valeurs expérimentales de porosité et de rugosité, récupérées respectivement à partir de l'analyse des images SEM et des mesures AFM. Alors que les valeurs de porosité semblent avoir un bon accord avec les valeurs expérimentales, considérées comme des limites supérieures pour la porosité car elles se réfèrent à la couverture de surface des bulles, nous constatons que nous surestimons la rugosité. Nous concluons alors avec deux explications possibles : soit nous sous-estimons la fraction volumique des bulles sur la couche poreuse, soit notre modèle n'est pas complet, donc nous négligeons un autre effet, qui n'est pas la rugosité, qui serait responsable de la variation constante de réflectivité que nous observons lors de l'exposition.

Enfin, nous souhaitons esquisser quelques perspectives qui pourraient être mises en œuvre pour poursuivre et améliorer les études actuelles. En particulier:

1. Mesures de réflectivité du W en fonction de la température et de la rugosité :

    - Utiliser un dispositif adéquat capable de mesurer également la composante diffuse de la réflectivité d'échantillons très rugueux, ainsi qu'un modèle plus précis capable de prédire la variation de réflectivité également à $\sigma >> \lambda$, comme les modèles utilisant la fonction BRDF.

2. Mesures ellipsométriques *in-situ* sur W lors d'une exposition au plasma D :

    - Réussir à réaliser des expositions au plasma sans élévation de température en utilisant un système de refroidissement, afin de mesurer directement les effets du plasma D sur la réponse optique W.
    - Inclure l'inventaire de surface D dans un modèle de Lorentz-Drude dépendant de la température de la fonction diélectrique W, déjà développé par Minissale et al. (2017), afin d'étudier la nature physique de l'interaction entre les atomes D implantés et les électrons W.

3. Mesures ellipsométriques *in-situ* sur les oxydes de W pendant l'exposition au plasma D :

    - Effectuer des mesures TEM sur l'échantillon d'oxyde exposé à basse température, pour observer la couche enrichie en W et extraire directement son épaisseur.

- Une fois que nous sommes sûrs de l'épaisseur réelle de la couche enrichie en W, utiliser l'ellipsométrie pour modéliser ses constantes optiques.

4. Mesures ellipsométriques *in-situ* sur W pendant l'exposition au plasma He :

   - Construire un modèle plus complet capable d'expliquer les mesures spectroscopiques. Une collaboration avec le LSPM à Paris, qui utilise le code FENICS pour modéliser la cinétique de croissance des bulles d'He, va bientôt démarrer à cet effet.
   - Approfondir l'étude de la dépendance de la densité des bulles d'He en fonction de l'orientation cristalline W.
   - Effectuer des mesures TEM des échantillons exposés à l'He, afin de mesurer la profondeur réelle de la couche poreuse et la distribution des bulles sur toute la couche.
   - Effectuer des mesures d'ellipsométrie après avoir chauffé les échantillons irradiés à l'He jusqu'à 1000 K, afin d'étudier une éventuelle récupération de surface entraînant moins de défauts et/ou une coalescence des bulles d'He (déjà observée dans des travaux précédents), et étudier comment de tels changements pourraient affecter la réflectivité et la rugosité de surface.

Acknowledgements

I would like to thank all the people that gave me their help and support during these three years.

First of all, a special mention to my supervisors, Marco Minissale and Régis Bisson, for their continuous help in dealing with the experimental problems (and there were quite a few), the extreme cure in revising my work (papers and oral presentations), their encouragement to never give up and always come up with new and interesting ideas, and for involving me in stimulating initiatives. I was rather an immature and unripe scientist at the beginning of the PhD, and they really taught me a method on how to conduct scientific research with a critical thinking. I will always be grateful to them for that.

I am truly thankful to all the permanent members of Plasma Surface team: Thierry Angot, for his persistent questions that served as an input for critical thinking; Gilles Cartry, for his endless patience in explaining plasma physics topics and the functioning of the load-lock chamber in CAMITER; Eric Salomon, for his help with XPS measurements; Jean-Bernard Faure and the rest of the mechanical workshop, for their prompt help in fixing any problem related to the experimental set-up.

A special thanks also to a few people from other teams, with whom I have worked quite closely: Céline Martin, for her help in the oxides synthesis and for all the microscopy measurements present in this work, for her patience in the explanations and all the constructive discussions about it; Andrea Campos and Martiane Cabié, for their help with electron microscopy characterizations; Greg Giacometti, for his help in AFM measurements and analysis; Cédric Pardanaud for his help with Raman measurements; Guillaume Serin, for his help with laser installation.

I would also like to thank a few people from institutions external to AMU that contributed to make my work progress: ISFIN, that made my two months mobility in Slovenia possible; Sabina Markelij (JSI), for her help in ion beam analysis measurements, her willingness to discuss and her warm welcome in Slovenia; Etienne Hodille (CEA), for his help in the interpretation of MHIMS data.

I would also like to thank all the administrative staff of PIIM for helping me in organizing my stay during the first months and later to always give their assistance for any problem.

I also wish to thank all the post-doc and PhD students that made these years in the lab so pleasant: Matthieu (for his help in realizing MHIMS simulations), Aleksandr (for his help in anything related to coding), Francisco (for his help with XPS and all the transfer operations), Surabhi (for sharing anxiety and giving valuable professional and personal advice), Mattia, Martino and Matheus (for the endless talks and laughters in the lunch room at the 6th floor).

Finally, a special thank goes to my family (my mother Lucia and my sister Giuliana) that supported me since the beginning and was always helpful even from a distance, for their effort in coming here for my defense despite all the difficulties of the travel. Thanks to my lifetime friends (Marta, Annalisa, Ciccio, Alessio and Alberto), to Andrea and to Marta, even though they couldn't be here. Finally, thanks to Nathan, for listening and supporting me, for bearing me in the most difficult moments and always cheering me up, and for making this last year joyful and amazing.

Contents

1 Introduction **2**

1.1 Context: nuclear fusion . . . 2
1.2 The tokamak fusion reactor: ITER . . . 3
1.3 Plasma-wall interaction . . . 6
1.3.1 The choice of W . . . 6
1.3.2 W/D interaction . . . 7
1.3.3 W/He interaction . . . 7
1.4 Optical diagnostics and thermography . . . 8
1.5 Motivation for this work . . . 10

2 Methods **12**

2.1 Experimental methods . . . 12
2.1.1 Samples preparation procedure . . . 12
2.1.2 Thermal oxidation procedure . . . 14
2.1.3 Optical methods . . . 16
2.1.4 RF plasma generation . . . 20
2.1.5 Imaging techniques . . . 26
2.1.6 X-rays Photoelectron Spectroscopy (XPS) . . . 33
2.2 Models . . . 34
2.2.1 Bulk W samples . . . 35
2.2.2 Optical interference model for multi-layer system . . . 36
2.2.3 Bennet-Porteus model for surface roughness . . . 37
2.2.4 Effective medium approximation (EMA) model . . . 37

3 Reflectivity measurements on W as a function of roughness and temperature **39**

3.1 Experimental procedure and effect of annealing on roughness . . . 40
3.2 Reflectivity variation with roughness and temperature: results and model discussion . . . 41
3.3 Chemical analysis: influence of surface composition on reflectivity . . . 45
3.4 Conclusions and perspectives . . . 46

4 Study on temperature and retention effect in W reflectivity variation during D plasma **48**

4.1 In-situ modification of W optical response during D plasma . . . 49
4.2 Evaluation of the effect of the plasma on ellipsometric measurements . . . 52
4.3 Effect of temperature and ion interaction in W reflectivity variation . . . 53
4.4 Estimation of D surface inventory with the code MHIMS . . . 57

4.5 Comparison of ellipsometry results and MHIMS modeling 61
4.6 Conclusions and perspectives: the effect of temperature 62

5 In-situ monitoring of W oxides reduction by D plasma 65
5.1 Sample preparation and plasma exposure 66
5.2 Oxide reduction by D ions: increase of extinction coefficient k 68
5.3 Oxide reduction by D ions: indirect measurement of W enriched layer . 70
5.4 Conclusions and perspectives 75

6 Microscopic and macroscopic investigation of He bubbles formation in W 77
6.1 Experimental methods and conditions 78
6.2 *Ex-situ* microscopy study on He bubbles size and density 80
6.2.1 SEM images treatment for He bubbles characterization 80
6.2.2 Impact of temperature 82
6.2.3 Impact of ion flux 84
6.2.4 Impact of surface state 86
6.2.5 Impact of grain orientation 86
6.3 Optical measurements 88
6.3.1 Reflectivity variation of the He exposed samples 88
6.3.2 Temporal evolution of porosity and surface roughness 89
6.4 Conclusions and perspectives 92

7 Conclusions 94
7.1 Summary 94
7.2 Perspectives 97

Chapter 1

Introduction

1.1 Context: nuclear fusion

The need to provide alternatives to fossil fuels is nowadays becoming more and more urgent. Although a huge progress has been done in the fields of renewable sources such as solar, wind and hydrothermal energy, they still are not able to provide high energy density in a steady fashion. Nuclear fission has been used extensively as a source of electricity since its advent in the 1950s, especially in countries such as France where 80% of electricity is generated by nuclear power plants. However, concerns over long-lived radioactive waste and public safety are resulting in increasing costs and political moves away from nuclear power. Nuclear fusion, which is gaining a constantly growing interest during the last decades, could be a promising and efficient solution, due to its high energy output, sustainability and safety [1].

Nuclear fusion consists in the combination of light nuclei to form heavier ones and release energy. It was proven to be the source of energy that powers the stars [2], in which the high core temperature ($\simeq 10^6$ K) inside the Sun makes the gas become a plasma. In addition, the nuclear fusion reaction can only take place if the reacting elements have sufficiently high kinetic energy to overcome Coulomb barrier. Inside the Sun, the high gravitational force confines the ion, making them overcome the Coulomb barrier. To make fusion on Earth, one of the ideas is to develop plasma confinement devices in which magnetic forces bring plasma particle together to achieve fusion. The fusion reaction which combines a high cross section with a low input energy is the deuterium-tritium (D-T) reaction [3], occurring between the two heavy hydrogen isotopes, which produces 3.5 MeV α particles ($^4He^{2+}$) and 14 MeV neutrons:

$$D^+ + T^+ \rightarrow^4 He^{2+} + n \tag{1.1}$$

The fuels necessary for the reaction are available on Earth and theoretically inexhaustible. Deuterium can be extracted by water through distillation, while tritium is a rare isotope of hydrogen (with a natural proportion of 10^{-18}) and is radioactive. However, among the goals of nuclear fusion through D-T reaction, there is also the breeding of tritium based on the interaction between fusion neutrons and lithium, largely available from seawater, which will be present on the walls of the machine. The D-T reaction does not generate any greenhouse gas nor long-term radioactive waste. Its safety comes from the fact that, even in the case of an accident, the plasma cools down and the reaction stops.

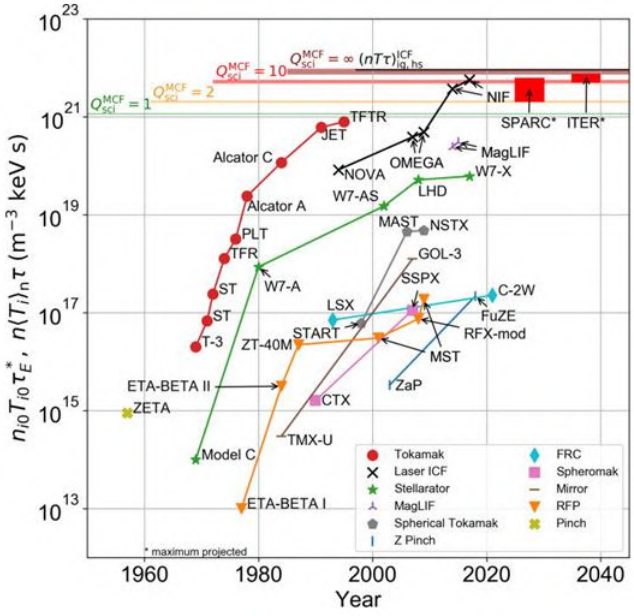


Figure 1.1: Triple products $n_{i0}T_{i0}\tau_E^*$ and $n < T_i >_n \tau$ (for inertial confinement devices and magnetic confinement devices, respectively) reached by different reactors vs year achieved, from Wurzel et al. [4].

In the fusion reaction described above, the neutrons, which carry 80% of the energy, leave the plasma without interacting with it and convert the energy into heat in the breeding blanket system. The α particles can transfer their energy to plasma through collisions. The fusion reaction become self-sustained when all energy losses are compensated by α particles heating and external heating is not required (so called "burning plasma"). The condition for self-sustained plasma (or "ignition") is described by the Lawson's criterion [5], resumed by the following triple product:

$$n_i \cdot T_i \cdot \tau > 5 \cdot 10^{21} keV \cdot s \cdot m^{-3} \tag{1.2}$$

where n_i is the ion density (in m^{-3}), T_i is the plasma temperature (in keV) and τ is the energy confinement time (in s). To realize this condition, several combinations of the three quantities are theoretically possible. One is met in the core of the stars and consists in very high n_i and τ, which allow the reaction to take place at relatively low T_i. In inertial confinement devices, a fuel target is heated and compressed by high-energy ultra-short laser pulses, to obtain high n_i and T_i with short τ. Finally, in magnetic confinement devices that we have described so far, magnetic fields are used to maintain a plasma with relatively low n_i, high T_i and τ (in ITER, for example, n_i=10^{20} m^{-3}, T_i= 8 keV in the core, and τ is a few s [6]). Figure 1.1 shows the triple product values reached by different fusion machines as a function of the year achieved, with the aim to illustrate the progress toward energy gain of different concepts over time.

1.2 The tokamak fusion reactor: ITER

Among the different configurations of magnetically confined fusion devices, the most common is the tokamak (figure 1.2(a)), which stands for toroidal chamber with mag-

netic coils. The toroidal coils create a torus-shaped magnetic field which confines the plasma particles inside the vacuum vessel. In such configuration, ions and electrons tend to diverge and the plasma is pushed outwards. This is why a poloidal field is added by running a current through the plasma, generated by the central solenoid, which makes the magnetic field lines helical. This configuration results in a pulsed mode of operation since it relies on the current generation by the central solenoid, which generally can sustain discharges up to several hundreds of s. Finally, the outer poloidal coils are used to set the plasma position and shape. The loss of magnetic confinements (which can occur for multiple reasons, for example heat loss cause by the presence of impurities in the plasma) is called disruption. The main challenge and complexity of the tokamak configuration is to optimize plasma performances while minimizing the losses of magnetic confinement.

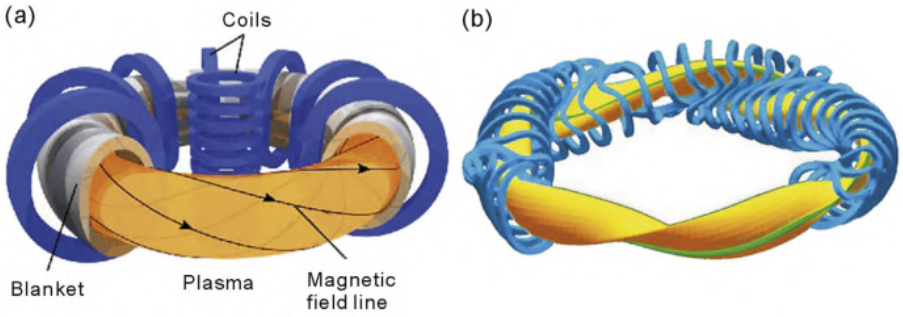


Figure 1.2: Schematics of two magnetic confinement configuration [7]: tokamak (a) and stellerator (b).

Another magnetic configuration in which it is possible to realize the Lawson's criterion is the stellerator (figure 1.2(b)), in which twisted coils allow direct plasma control and there is no need for plasma current. They work in steady-state regime and ensure a nearly disruption free operation as compared to tokamaks, however their construction is more complex.

ITER is a tokamak type reactor that is being built in the south of France, after an agreement signed in 1986 by the European Union, Japan, the Soviet Union and the USA, and that now includes 35 nations with the common goal to demonstrate the scientific and technical feasibility of controlled nuclear fusion. The final aim of ITER is to produce plasma with a power amplification $Q>10$ (where Q is the ratio between the output and the input power). So far, only the condition $Q\leq 1$ has been reached by some reactors such as JET (Joint European Torus) and TFTR (Tokamak Fusion Test Reactor).

The main components of ITER tokamak are depicted in figure 1.3. The vacuum vessel is a toroidal metallic chamber in stainless steel, containing a divertor and a blanket. The divertor is located at the bottom of the vessel and extracts heat and particles produced by the fusion reaction (α particles transported by the plasma), fuel particles that have not undergone fusion reaction and impurities from the plasma core. The divertor is composed by 54 cassettes made by tungsten (W) monoblocks (figure 1.4). Each monoblock contains a CuCrZr tube covered with a Cu layer for active cooling by a coolant, which will transfer the radiative and neutron heat to the ITER cooling towers. The vacuum vessel is covered by a blanket which was originally supposed to be made of beryllium (Be), thanks to its properties of low

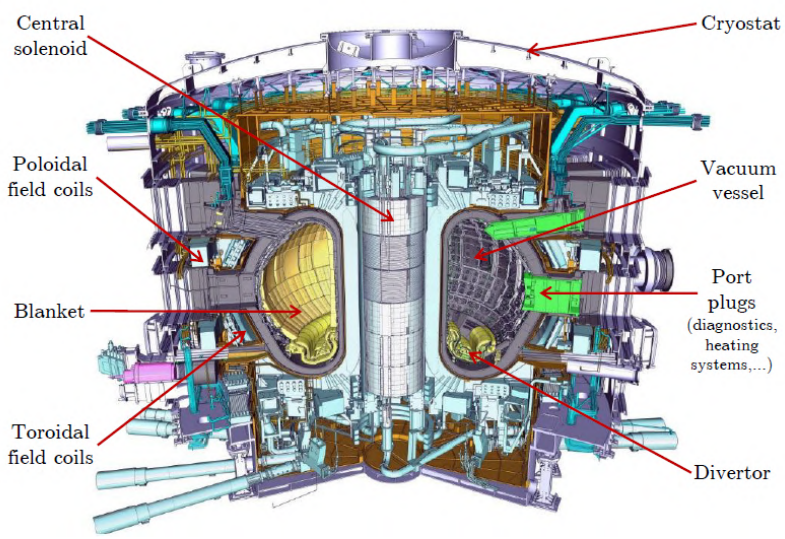


Figure 1.3: Schematics of ITER tokamak components [8].

plasma contamination, fuel retention and neutron activation. Because of safety and toxicity reasons, however, Be is being replaced by W. It will be cooled for the heat transfer (80% of the total fusion energy output carried by neutrons) to the ITER cooling towers.

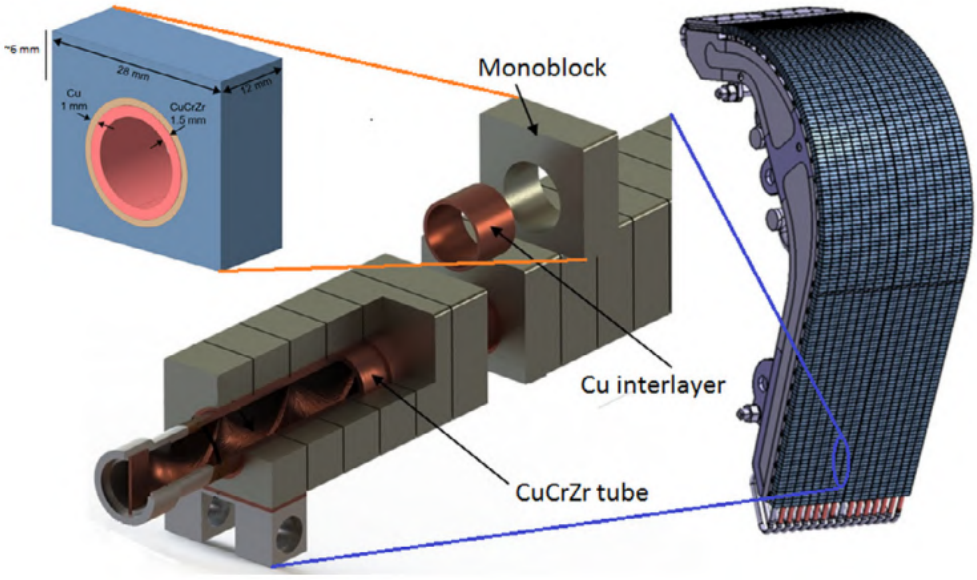


Figure 1.4: Schematic picture of a W monoblock, its characteristic dimensions and its location in the divertor structure [9].

The other components of ITER are then the superconducting magnetic coils, the cryostat, the fuel supply lines, the cooling system, the plasma heating systems and several plasma diagnostics. In the following, we will focus mainly on the plasma-facing components (PFCs) of the vacuum vessel and the optical diagnostics used in ITER, as the subject of the present work is the evolution of optical properties of W materials subjected to ion-surface interaction.

1.3 Plasma-wall interaction

1.3.1 The choice of W

The choice of plasma-facing materials (PFM) is of crucial importance to maximize the plasma performance and ensure the correct functioning of the machine. Originally, this choice for the divertor components was oriented towards low atomic number (Z) materials, mainly carbon, for their favourable properties of low plasma contamination. Carbon, in particular, was chosen for its high sublimation point (>3900 K), allowing high heat loads, together with a good plasma tolerance of carbon impurities. However, the main issue of carbon is the chemical erosion by hydrogen isotopes (HI) [10], which is high even at low energy of the incident particles. In addition, in the co-deposited layers of HI with carbon, fuel retention is very high [11], raising nuclear safety issues about T trapping.

Atomic number	74
Atomic mass	183.85
Crystallographic structure	body centered cubic (bcc)
Lattice constant	3.15 A
Atomic concentration	$6.3 \times 10^{28} m^{-3}$
Density	19.3 g/cm^3
Melting point	3687 K
Boiling point	5828 K
Recrystallization temperature	1573-1773 K
Ductile-to-brittle transition temperature	373-623 K

Table 1.1: Main physical properties of W [12].

For all these reasons, the choice of carbon for divertor PFMs has been put aside and the efforts of the community have been focused rather on high Z materials, in particular on the category of refractory metals, proposed for the first time in 1992 [13]. The choice of W as a PFC comes from its low chemical sputtering and physical erosion, as well as low fuel retention as compared to low Z materials such as carbon and Be. It also has the highest melting temperature ($\simeq$3687 K) among the refractory metals, and has high thermal conductivity and mechanical resistance. However, W is brittle at room temperature [14], with the possible risk of creating micro-cracks during the fabrication process or during plasma operation. Furthermore, it has an high chemical affinity with oxygen, posing issues about the W PFCs oxidation (especially at high temperatures) [15]. In addition, the interaction with helium (He) ions can significantly modify W surface morphology, with possible consequences on HI retention [16].

In the ITER divertor region, the expected ion and neutral fluxes will be of the order of $\simeq 10^{24}$ particles $m^{-2}s^{-1}$. Considering a discharge of 400 s, the particles fluence for each discharge will be $\geq 10^{26}$ particles m^{-2}. The kinetic energy of the incident ion is expected to be in the range 10-100 eV, while the surface temperature will be in the range 800-1300 K [15]. The main impurities are expected to be oxygen (dominant impurity), water (heavy water, tritiated water), carbon (<1.5%).

1.3.2 W/D interaction

Since the sputtering threshold energy of D ions on W is around 244 eV [17] and the energy of HI in the divertor region should not exceed 100 eV, no erosion of W PFCs is expected. However, even in this range of energy, ion flux and temperature, D ions induce indeed a change in W surface morphology. The most common feature observed in D irradiated W are the so called "surface blisters", 3D voids on the surface where D is trapped in a gaseous form. They are probably created from oversaturation of D atoms in W defects close to the surface, such as vacancies, grain boundaries and dislocation loops, which would cause high stress fields [18]. Their formation depends mostly on the ion fluence, in the range $10^{23} - 10^{25}$ ions m^{-2} [19]. With increasing ion fluence and ion energy, their size increases (up to a few µm in diameter) and their density decreases by 2-3 order of magnitudes [20]. Furthermore, there seems to be also a dependence on temperature, as they are not observed at temperatures >873 K. W blistering could lead to instability of the plasma if blisters burst and eject large amounts of gas and/or material [21].

Another common feature observed multiple times at ion energies lower than the displacement threshold is the so called "deuterium super saturated layer" (DSSL), a surface region with high concentration of D atoms (up to 10 at%) whose thickness depends on the ion energy (going from 5-6 nm at 45 eV to 11-12 nm at 175 eV [22]). It was observed in [23] that the DSSL formation during irradiation can cause high lattice distortion in W, as a synergistic effect of D ions, which can produce defects such as W interstitials, and D solute atoms, which prevent the recombination of vacancies with such defects.

1.3.3 W/He interaction

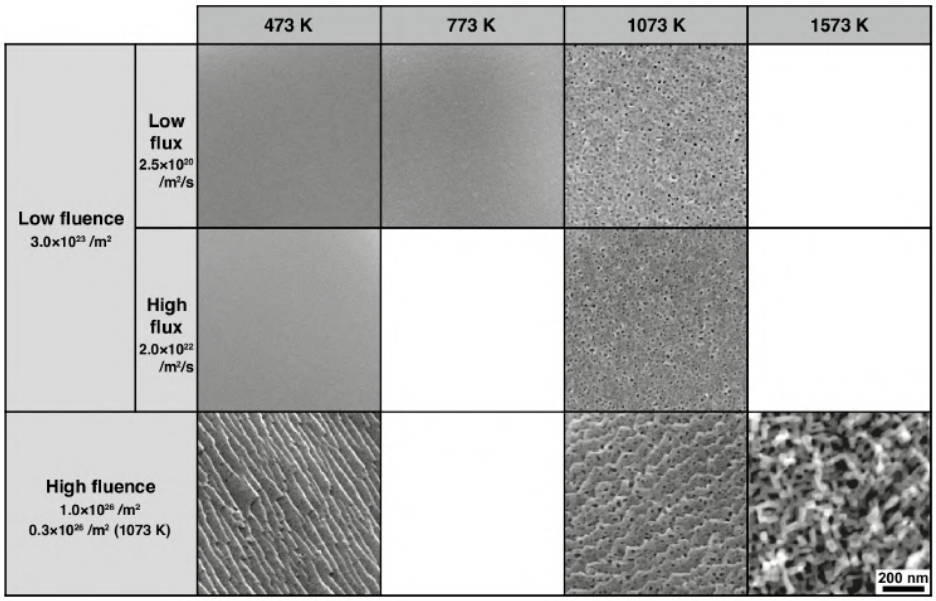


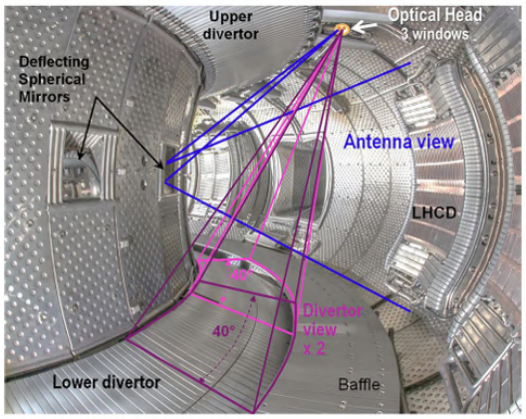
Figure 1.5: SEM images of He irradiated tungsten samples with different fluences and temperatures, from [24].

As compared to D, He ions create much bigger damage in W, due to their low solubility in metals ($<10^{-11}$ at.fr./Pa in many liquid metals, from [25]) and low chemical affinity with W [26]. Intensive He ion fluxes can cause erosion of the surface of W PFCs as well as lattice damage in their bulk. The nature and extent of the damage depends on both the kinetic energy of the incident He ions as well as the W PFCs surface temperature [27]. For the energies values expected in the divertor (<100 eV), the implantation depth of He ions in W is estimated to be around <5 nm (from SRIM [28] simulations). Once implanted in W, He atoms can easily diffuse due to their very low migration energy ($\simeq$0.13 eV) [29]. They are then trapped in pre-existing and/or radiation-induced defects in W lattice. The main process generating lattice damage and consequent He accumulation in W is the so called He self-trapping mechanism, when a cluster of He atoms in the W lattice emits a W vacancy and a W interstitial, resulting in Frenkel pair production [30, 31]. The reason why He can accumulate so easily in W (creating He atoms clusters) even if there's only few pre-existing lattice defects is the high binding energy of 2 He atoms of around 1 eV [29], resulting in high tendency for He atoms to cluster. This can explain why, even at temperatures where migration of He atoms is larger than for D atoms (around 500 K), He will form bubbles right below the surface, i.e. as soon as it encounters another He atom, at depth of around 10 nm. On the other hand, the interaction between D atoms in W lattice is largely repulsive at short D-D distances, preventing D atoms to self-trap in W but only to be trapped by defects [30]. At ion energies lower than the physical sputtering threshold for He on W ($\simeq$105 eV [17]), two main surface morphologies can appear due to He irradiation, depending on the substrate surface temperature and the He ions fluence (figure 1.5). At temperatures lower than $\simeq$1073 K and fluences lower than $\simeq 10^{26} He/m^2$, W surface morphology can appear as undulating and overall more rough as compared to an unexposed surface. It is typical to observe the presence of holes as well as facetted structures, which are linked with the creation in the near-surface layer ($\simeq$30 nm) of over-pressurized bubbles which then burst on the surface, and whose shape can depend on the grain orientation [32, 33]. Such surface modification of He irradiated W will be discussed later in this thesis, in chapter 6.1. At high temperatures ($\simeq$1073 K) and high fluences ($\simeq 10^{26} He/m^2$), W surface morphology can appear as undulating and overall more rough as compared to an unexposed surface. At temperatures higher than $\simeq$1073 K and fluences higher than $\simeq 10^{26} He/m^2$, W surface atoms are displaced giving rise to highly porous and elongated nanostructures, commonly called W "fuzz". It has been shown by recent studies that their size increases with increasing temperature [27] and that the thickness of the nanostructures layer increases with the exposure time (thus, with the ion fluence) [34]. The presence of W fuzz poses serious problems for fusion reactors such as ITER, as it might reduce the lifetime of PFCs and also enhance the contamination of the core plasma. The W fuzz formation mechanism is still unclear, but seems to be related to the formation of He bubbles below the surface, their growth and coalescence and, at the end, the bursting of the over-pressurized ones located close to the surface.

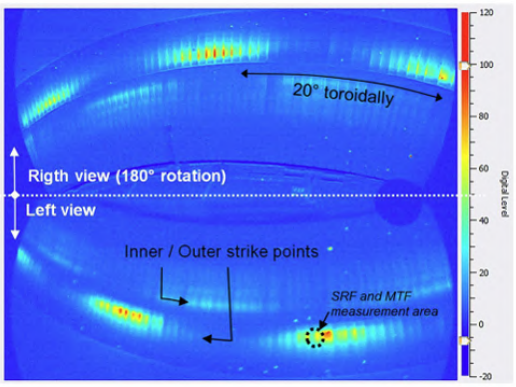
1.4 Optical diagnostics and thermography

In-situ and real-time diagnostics play an essential role in monitoring plasma-wall interaction processes, such as erosion and redeposition, which raise serious issues as they

can lower the lifetime of PFCs and increase fuel retention and plasma contamination. In addition, as the plasma continuously modifies the surface, new defects are created in the material which can change the HI retention [35]. For machines that rely on a mixture of D and T, the permeation of T through materials poses serious nuclear safety issues [36]. *In-situ* diagnostics implementation is challenging in tokamak conditions as most of the techniques are not compatible with the harsh environment typical of magnetic confinement devices, making it necessary to extract the exposed material from the machine and conduct a post mortem analysis using *ex-situ* methods. For the moment, the most reliable *in-situ* diagnostics are mostly optical and laser-based techniques. Examples include laser-induced breakdown spectroscopy (LIBS) [37] and laser-induced desorption spectroscopy (LIDS) [38], which allow to analyze the surface composition and HI retention locally, as typical laser-surface interaction area is on the order of a millimeter or less.



(a)



(b)

Figure 1.6: Upper port endoscope fields of view in the tokamak WEST (a) and IR image of the divertor area during a plasma pulse [39].

A crucial point to ensure the lifetime of PFCs as well as their correct functioning during operation is their surface temperature measurement, realized through non-contact optical diagnostics (figure 1.6 depicts some of the optical diagnostic of the tokamak WEST, located in the south of France). Such instruments (pyrometers, IR cameras) are able to reconstruct in real time the heat loads distribution on entire W monoblocks during discharge and to accurately monitor the temperature of the PFCs from the emitted radiation. For this reason, it is of fundamental interest to increase the knowledge of PFCs surface emissivity, which depends on several factors such as the wavelength and the temperature as well as the surface conditions (roughness, crack, presence of contaminants) [40]. Also, for the same wavelength and temperature there is a large spread of tungsten emissivity depending on the manufacturing process (mainly from 0.05 to 0.5) [41]. As a consequence, with the introduction of all-metal walls in fusion devices, surface emissivity becomes a very important and challenging issue for accurate surface temperature measurement. As was shown in a significant number of studies, W exhibits pronounced surface morphology changes under He plasma exposure, which can affect its thermal and mechanical properties [42].

In addition, ion beam analysis offers a way to probe the depth distribution of implanted species *in situ* [43], while transmission electron microscopy (TEM) allows for direct imaging of nm-sized bubbles nucleation and growth [44].

In situ spectroscopic ellipsometry presents an alternative method to measure the surface morphology evolution under plasma irradiation. The technique is non-destructive and non-contact, is not dependent on the absolute reflectivity of the surface, and provides sensitivity to nm-scale changes in roughness. To determine this information, ellipsometry measures how the polarization of light is changed when reflected from a sample surface. In this way, it is more robust against instabilities like variations in the beam intensity, and provides greater sensitivity to thin surface layers. One limitation of this approach is that ellipsometry gives direct information only on the optical properties of the surface, rather than on its physical structure. However, it is possible to overcome this problem by comparing the ellipsometric results with complementary techniques and by an adequate modeling of the ellipsometric data. By doing so, it could be possible to gain a basic knowledge of the plasma-surface interaction in an indirect way, passing through the measurement of the optical properties.

1.5 Motivation for this work

In the context of nuclear fusion, scientific advances are required in several areas including radiation-resistant materials capable of operating at high temperatures and development of compatible and reliable *in-situ* diagnostics. The monitoring of PFCs during plasma operations must take into consideration their surface modifications due to intensive fluxes of light elements, such as HI and He, as well as neutrons, impurities and possible oxidation. In particular, since ITER and many other fusion devices are moving towards first-wall metallic components, to conduct such studies on materials like W in a wider range of temperatures and energies is becoming more and more urgent and essential.

In this thesis, we use laboratory experiments that include plasma exposures and optical techniques, in order to investigate the fundamental interaction between W surface and the ions (D and He) coming from the plasma. The aim of the thesis is to prove the feasibility and advantage of using optical techniques (both *ex-situ* and *in-situ* during plasma) in gaining insight on the plasma-wall interaction indirectly from the optical properties.

To begin, chapter 2 gives an overview on the experimental methods and the theoretical models used during the three years of the PhD to perform our studies. Afterwards, the work can be seen as composed by three logically subsequent studies, each one realized every year of the PhD:

- A first preliminary study has been realized before proper plasma exposure, by performing direct reflectivity measurement of W in controlled conditions, without exposing it to plasma, but simulating the effect of He plasma irradiation (roughness increase) by tailoring *ad-hoc* the surface roughness through chemical etching. In this way, it was possible to conduct a parametric study on the evolution of W reflectivity with temperature (during multiple annealing cycles, in the range 300-1073 K), as a function of the controlled roughness (in the range 20-100 nm). The results of this study will be discussed in chapter 3 of this thesis.

- The following study, discussed in chapter 4, was realized using an *in-situ* optical technique (spectroscopic ellipsometry) in order to monitor W surface evolution during plasma exposure. We perform some first experiments using D plasma,

as, in our working ranges of ion energy, flux and temperature, it is not supposed to induce considerable changes in the surface morphology. In this way, we could focus on the modification of W electronic and optical response because of the combined effect of temperature increase (up to 600 K) and interaction with D ions. In particular, using a model of HI migration in W, we were able to investigate on the D surface retention as a function of temperature, and to compare it with the reflectivity variation measured by ellipsometry.

- Chapter 5 contains a parallel study to the one described in chapter 4, also performed during the second year. It consisted in the thermal growth of W oxides layer on W substrates and their *in-situ* ellipsometric measurements during D plasma exposure. The interest of studying W oxides exposed to plasma in nuclear fusion context is high and will be deeply discussed later in chapter 5. The main point here is again to prove the effectiveness of *in-situ* optical diagnostics to monitor the surface evolution caused by the plasma interaction. In particular, we found that ellipsometry was able to detect the reduction of the oxide layer induced by D ions and to probe the presence of a sub-surface W enriched layer to which the *ex-situ* microscopy techniques were not sensitive.

- The last study, described in chapter 6 and realized during the last year of the thesis, consisted in performing *in-situ* ellipsometric measurements in more realistic conditions of He plasma exposures, where W surface morphology is strongly modified by the interaction with He ions (creation of over-pressurized He bubbles, increased roughness). In particular, from the decrease of reflectivity observed during plasma exposure, we made a first attempt to reconstruct the kinetics of He bubbles formation and the temporal evolution of surface roughness by modeling the *in-situ* data with an adequate porous layer. We validate our results with the use of *ex-situ* microscopy performed on the exposed samples, in order to measure the size and density of the He bubbles burst on the surface.

Finally, in the conclusions we will summarize the main results obtained during this work and outline some future perspectives for a possible continuation of these studies.

Chapter 2

Methods

This chapter gives an overview of the methods used during this thesis, which can be distinguished into experimental techniques and theoretical models.

As the title of this thesis suggests, the main effort of this work is to characterize the optical properties of W (and W oxides) exposed to plasma. To achieve this goal, samples had to be prepared and characterized using different experimental techniques. Among these techniques, we first briefly discuss the samples preparation methods (mechanical and electro-chemical polishing, thermal oxidation of W samples), prior to optical measurements and plasma exposures. We then focus on the description of the two optical techniques used in this thesis: one, laser reflectometry, allows to perform direct spectral measurements of W reflectivity; the other one, spectroscopic ellipsometry, which is used for *in-situ* measurements during plasma exposure of the optical constants of the material, as well as other properties (overlayer thickness, roughness, porosity). We then describe RF plasma generation and characterization of plasma parameters with a Langmuir probe. Eventually, as the plasma exposure can induce a morphological and chemical modification of the surface (appearance of cracks, holes and other lattice defects), we describe the *ex-situ* techniques used to visualize the morphology of the exposed samples and to extract their roughness parameters (Confocal Microscopy, Atomic Force Microscopy, Scanning Electron Microscopy), and the one used to evaluate their chemical composition and evolution (X-rays Photoelectron Spectroscopy).

In addition, the theoretical methods used to model optical properties are described: starting from the direct determination of bulk W dielectric function, continuing with the reflectivity from a multi-layer stack, the Bennet-Porteus model for the reflectivity of a rough surface and the effective-medium approximation (EMA) model for a porous or composite layer.

2.1 Experimental methods

2.1.1 Samples preparation procedure

The polycrystalline W samples analyzed during this thesis are provided by GoodFellow (U.K.). They are either square samples with dimensions 10x10x0.5 mm^3 or round samples with 22 mm diameter and 0.5 mm thickness. Those are made from laminated W with a 99.95% purity, and all the treatments (mechanical and/or electrochemical

polishing, annealing, etching, etc.) are realized in PIIM laboratory (Aix-Marseille University), after delivery from the company. Those samples are used both for W oxides thermal growth, for optical measurements and for direct exposure to D and/or He plasmas, also realized in PIIM laboratory.

Mechanical polishing

Step	Foil	Lubricant	Force (N)	Rotation speed (rpm)	Rotation verse	Time (min.)
1	Diamond paper 54 µm grains	Water	25	300	Concordant	1.5 (square) >4 (round)
2	Diamond paper 18 µm grains	Water	25	300	Concordant	1.5 (square) 2 (round)
3	Paper 9 µm grains	Aerosol LPS4	25	300	Concordant	1.5 (square) 2 (round)
4	Paper 3 µm grains	Aerosol LPS4	20	300	Concordant	1.5 (square) 2 (round)
5	Paper 1 µm grains	Aerosol LPS4	15	300	Concordant	1.5 (square) 2 (round)

Table 2.1: Table resuming the five steps of mechanical polishing of W samples.

This procedure was realized on as-received GoodFellow samples, in order to smooth the surface by uniformly scratching it and making it mirror-like. It was performed using an ESCIL Saphir 520 machine [45]. Such machine is able to polish simultaneously five samples which are previously incorporated in a resin, obtained by mixing a powder and its correspondent solvent (2:1 proportion), both provided by Presi [46]. The sample is pressed onto a template with a bolt and the liquid resin is poured in the template and let solidify for one day, after which it is removed and ready for polishing procedure. The mechanical polishing procedure is made of different steps, during which it is possible to vary the force applied to the samples, the velocity and direction of rotation (of the polishing foil with respect to the samples, whose velocity is fixed), the use of water or aerosol as lubricant and the duration of each step. The five steps are resumed in table 2.1. The purpose of the first two steps is to scratch uniformly the surface in every direction, using abrasive diamond foils with decreasing grains dimension. The purpose of the remaining three steps is to make the surface of the samples reflecting and mirror-like, using lubricants with different particle dimensions, that are sprayed on paper with correspondent grains dimensions. The time of each step depends both on the amount of exposed surface of the sample and on the success of the previous steps. It is common, in those last steps, to insist longer in order to have a reflecting surface as big as possible.

To remove samples from the resin, they are washed in an acetone ultra-sound bath for more than one hour. Once they are removed from the resin, an additional ultra-sound bath in acetone and then ethanol is performed, in order to completely remove the residual layer of resin on the surface.

Electro-chemical polishing

Electro-chemical polishing is performed on already mechanically polished samples, in order to better visualize crystalline grains by removing a small amount of material

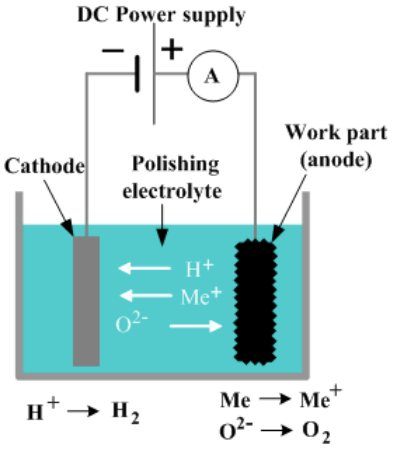


Figure 2.1: Schematic diagram of the electro-chemical polishing process [47].

without inducing mechanically deformation of the surface. It is an anodic dissolution process in which a metallic sample is immersed into an electrolyte solution and works as an anode. A potential difference between the sample and a metal cathode induces a current from the anode to the cathode, causing metal ions removal from the surface of the sample and dissolving into the electrolyte solution (as represented in figure 2.1). The amount of removed material depends on the type of electrolyte, on the applied voltage and on the duration of the process, other than the geometry of the sample and its distance from the cathode.

In this work, we use similar conditions than the ones experimental determined by Addab [48]. Distilled water containing 1.5% of NaOH is used as the electrolyte solution. The distance between the anode (W sample) and the molybdenum (Mo) cathode is 12 cm, and the applied voltage is 7 V for a duration of 15 s. The electrolysis of W in NaOH can be described by the following simplified chemical reaction:

$$W + 8OH^- \rightarrow WO_4^{2-} + 6e^- + 4H_2O \tag{2.1}$$

After electro-chemical polishing, samples are washed in an ultra-sound bath of acetone (for 20 minutes), ethanol (for 20 minutes) and distilled water (for 20 minutes), and finally rinsed with optical paper. They are then annealed in vacuum (base pressure: $4{\times}10^{-8}$ mbar) at 1073 K for 30 minutes using an high power laser, in order to desorb carbon and oxygen impurities and reduce at minimum the contamination.

2.1.2 Thermal oxidation procedure

The thermal oxidation of W samples is realized in the CAsPEr experimental set-up, already described in [48] and [49], under the supervision of Céline Martin. The main goal of this step is to perform a controlled thermal oxidation process, maintaining high vacuum environment and controlling the temperature of the substrate as well as the gas injection and its pressure decay during the process.

The set-up consists in a series of stainless steel tubes that connect a quartz cell, where the sample is placed and with an oven under it, to the vacuum pumps and pressure sensors. A primary pump followed by a turbo-molecular one allows to reach a base pressure of about 10^{-7} mbar. A set of manual and pneumatic valves allows to

separate the different parts of the system and to control the gas pressure in each part, with three capacitive membrane sensors measuring gas pressure in different ranges: 0-1.33 mbar, 0-13.3 mbar and 0-1330 mbar. Oxygen is introduced in the system from a bottle connected to one side of the set-up (image 2.2). The sample is placed into a cell (which has a volume of 0.12 l) made of quartz in the lower half (which can be heated up to 1200 K) and of pyrex in the upper half (which can be heated up to 800 K). A small oven with an adjustable height is placed around the quartz cell and can be programmed to reach the desired oxidation temperature with a specific ramp.

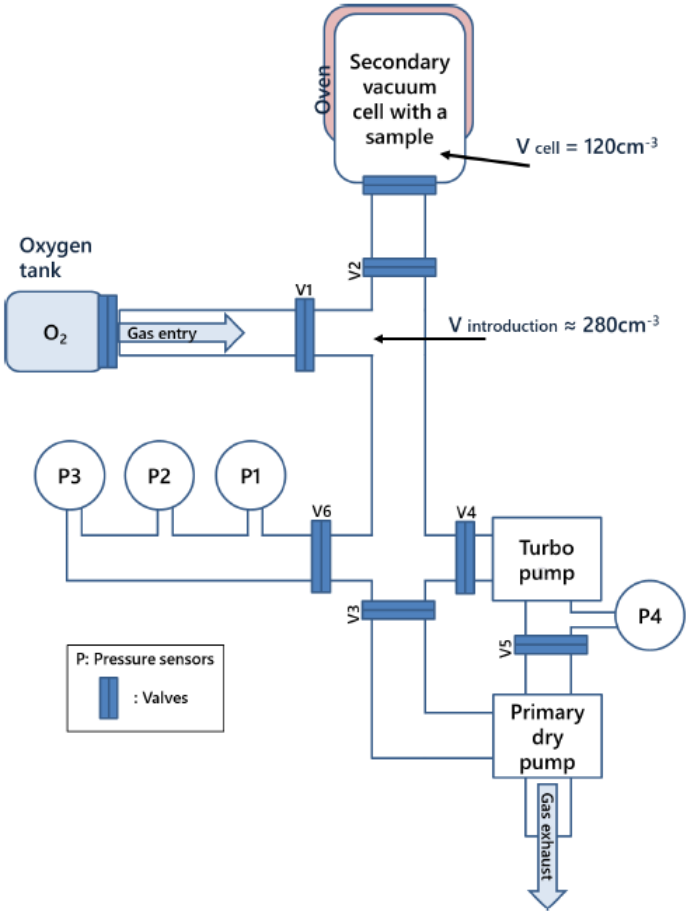


Figure 2.2: A schematic representation of the experimental set-up CAsPEr used for thermal oxidation [49].

For the thermal oxidation performed in this study, the samples in the vacuum cell are heated to the desired oxidation temperature (1073 K) through a 4 hours ramp, and pumped for about 5 minutes at this temperature until a stable vacuum is achieved. The vacuum cell is then separated from the rest of the set-up, and oxygen gas is introduced in the volume between the bottle and the set-up (0.28 l). When the desired oxygen pressure is set, thermal oxidation process is started by opening the valve connecting the vacuum cell to the rest. The oxygen pressure, recorded during the process, drops exponentially to 10-15% of the initial value. The thermal oxidation is then stopped by pumping the system and switching off the oven.

The thermal oxidation is performed at 1073 K in order to be relevant for plasma-facing components (PFCs) surface temperature conditions in fusion environments and

also to ensure thermal stability of the oxide layer during plasma exposure. Different protocols with different oxidation times and oxygen pressures have been tested, based on the previous works of [48] and [49], in order to obtain W oxide layers with different thicknesses, as will be discussed in chapter 5.1.

2.1.3 Optical methods

Reflectometry set-up

Direct reflectivity measurements of W samples (whose results will be described in chapter 3) are realized via the experimental set-up shown in figure 2.3, described in [50]. One sample at a time is fixed on a Macor sample-holder and placed into a vacuum chamber (base pressure: 10^{-8} mbar), to limit surface contamination (e.g., oxidation). Spectroscopic reflectivity measurements in the 500-1100 nm range were performed using a supercontinuum white-light laser source (YSL Photonics, model SC-5, SCL in figure 2.3) emitting in the 450-2400 nm range with a maximum power of 1.5 W and with a fiber-collimated beam of diameter 1.5 mm. The SCL beam passes through a linear polarizer (ThorLabs, model LPVIS100-MP2, operating in the 550-1150 nm range) and reaches a 70/30 beam splitter (ThorLabs, model BSS10, BS in figure 2.3), which reflects 30% of the incoming polarized beam into an integrating sphere made in Spectralon (LabSphere, IS1 in figure 2.3), connected to a fiber spectrometer (Avantes, model AvaSpec-ULS2048L, 200-1100 nm, FS1 in figure 2.3) through a 1000 µm core fiber. The aim of the first integrating sphere was to quantify the intensity fluctuations of the SCL arising from the non-linear mechanisms that allow the creation of a supercontinuum (mainly dependent on the pumping noise). The SCL resulted to have intensity fluctuations of around 2%. At the same time, 70% of the incoming polarized beam is transmitted by the BS to either a removable reference silver mirror (ThorLabs, model PF05-03-P01, M2 in figure 2.3) or the W sample. In the latter case, the SCL beam crosses the silica window twice (before and after hitting the W sample) and is sent to a second integrating sphere (IS2) by means of another silver mirror (M1 in figure 2.3), identical to the first one.

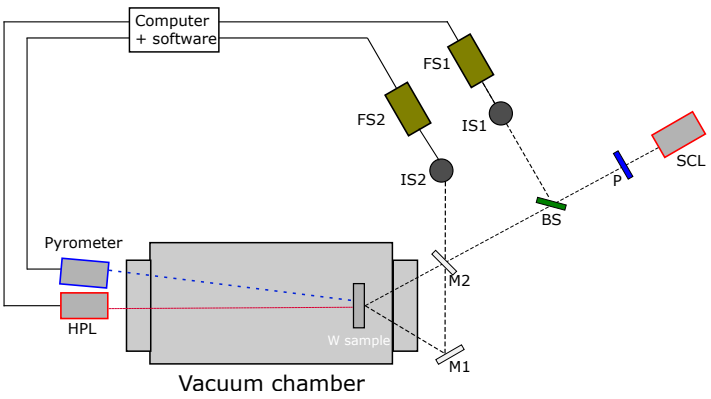


Figure 2.3: Schematic of the experimental setup: HPL, high power laser; SCL, supercontinuum laser; P, polarizer; BS, beam splitter; M1 and M2, fixed and removable silver mirrors, respectively; IS1 and IS2, integrating spheres of reference and sample side, respectively; FS1 and FS2, fiber-optic spectrometers connected to IS1 and IS2, respectively.

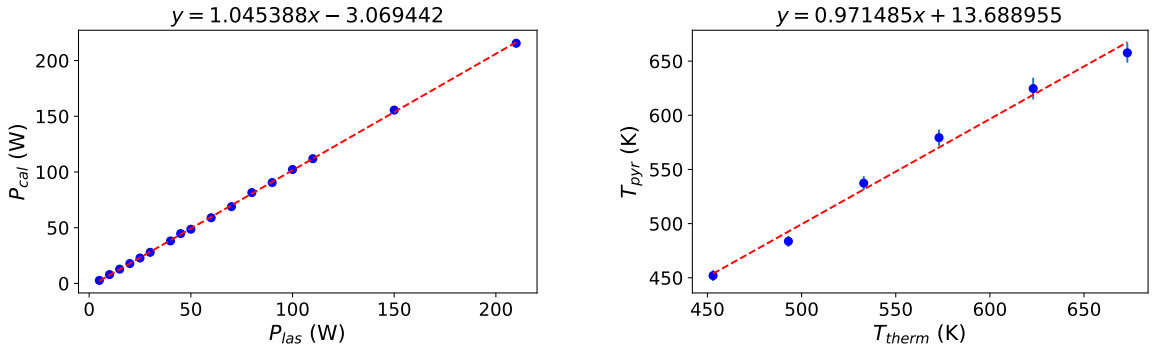
The reflectivity recorded by FS2 was obtained using the following equation:

$$R_{W,FS2}(\lambda) = \frac{S_{meas}(\lambda) - S_{dark}(\lambda)}{S_{ref}(\lambda) - S_{dark}(\lambda)} \frac{1}{T_{wi}^2(\lambda)} \tag{2.2}$$

where S_{meas} and S_{ref} are the spectra obtained by sending the SCL beam to the W sample or to the reference mirror M2, respectively; S_{dark} is the dark spectrum obtained with the SCL source switched off; T_{wi} represents the transmission through the fused silica window. All reflectivity signals were then divided by the intensity signal S_{FS1} recorded by the fiber spectrometer FS1, placed on the reference side and collecting the light reflected from the BS. The signal from FS2 ("sample-side" setup), in fact, carried information not only on the interaction between SCL beam and samples, but also on the intrinsic intensity fluctuations of the SCL. The purpose of the "reference" side is to measure only such intrinsic fluctuations in real time, i.e., synchronized with the sample side. The corrected W reflectivity signal is then given by:

$$R_W(\lambda) = R_{W,FS2}(\lambda) \cdot \frac{S_{FS1(\lambda,t=0)}}{S_{FS1(\lambda,t)}} \tag{2.3}$$

where $S_{FS1(t)}$ is the signal recorded by FS1 at the generic time t when the SCL beam is sent on the sample, and $S_{FS1(t=0)}$ is the same signal recorded at the initial time when the SCL beam is sent on the reference mirror.



(a) (b)

Figure 2.4: Calibration curves of HPL power with respect to a calorimeter (a) and of the pyrometer temperature with respect to a thermocouple (b).

Reflectivity measurements were realized varying the temperature of the sample from 300 to 1073 K. The samples are heated with a continuous wave high-power laser (AMTRON, HPL in figure 2.3), based on a fiber-coupled GaAs diode emitting at 805 nm placed outside the vacuum chamber, impinging on the backside of the sample. The laser is equipped with a distilled water and air cooling system. It can convey a maximum power of 200 W and was previously calibrated with the use of a calorimeter (figure 2.4 (a)). The temperature of the sample is monitored via a pyrometer (SensorTherm, model METIS M323), working in the 2-2.6 µm spectral range and allowing measurements of temperatures in the range 323-1073 K. The pyrometer was previously calibrated on the values measured by a thermocouple (K-type) while heating W sample via a backside oven in the experimental set-up CAMITER (described in section

2.1.4), as it is possible to see in figure 2.4 (b). The error bars on pyrometer temperatures are calculated as standard deviation of the values obtained using different emissivity parameters (ϵ=0.3, corresponding to the cleanest surface, ϵ=0.35 and ϵ=0.4, corresponding to the most oxidized surface). For all the following measurements on W present in this work, the emissivity parameter set in the pyrometer is ϵ=0.3.

In-situ spectroscopic ellipsometry

Spectroscopic ellipsometry is an optical technique that measures the change in light polarization upon reflection on a sample [51]. The name "ellipsometry" comes from the fact that the linearly polarized light which is sent on the sample often becomes "elliptical" once reflected. Ellipsometry measures two quantities, Ψ and Δ, which represent, respectively, the amplitude ratio and the phase difference between s and p-polarized light waves. In spectroscopic ellipsometry, Ψ and Δ spectra are measured by changing the wavelength of light, generally in the UV/visible/NIR range. This technique is widely used for thin films characterization, for example growth monitoring in real-time and processes diagnosis including etching and thermal oxidation. Some remarkable features of spectroscopic ellipsometry are: high precision of the measurement and thickness sensitivity ($\sim$ 0.1 Å), non-destructive and fast measurements, possibility of *in-situ* real-time monitoring of the surface evolution (as it is the case for this study). On the other hand, there are two general restrictions of ellipsometry: (i) surface roughness of samples has to be rather small compared to the light wavelength, as light scattering by an high surface roughness would severely reduce the reflected intensity; (ii) the measurement has to be performed at oblique incidence (usually in the range 60-80°, depending on the material), to better distinguish s and p-polarizations. In addition, there is one inherent drawback of ellipsometry which is the indirect nature of its characterization method: in general, the interpretation of measurements results is rather difficult, if one only looks at the absolute values of Ψ and Δ. Thus, the construction of an optical model is required to extract physical properties, such as the optical constants and film thicknesses of the sample [52].

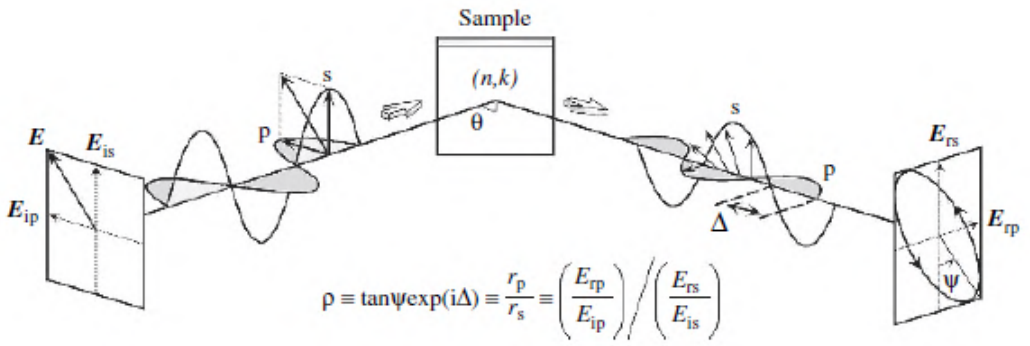


Figure 2.5: Schematic representation of the measurement principle of ellipsometry [51].

Figure 2.5 illustrates the measurement principle of ellipsometry. When light is reflected by a sample at oblique incidence, it is classified into p- and s-polarized light waves, depending on the oscillatory direction of its electric field. In p-polarization, the electric fields of incident and reflected waves oscillate within the same plane (called plane of incidence), while in s-polarization they oscillate perpendicularly to it. If we

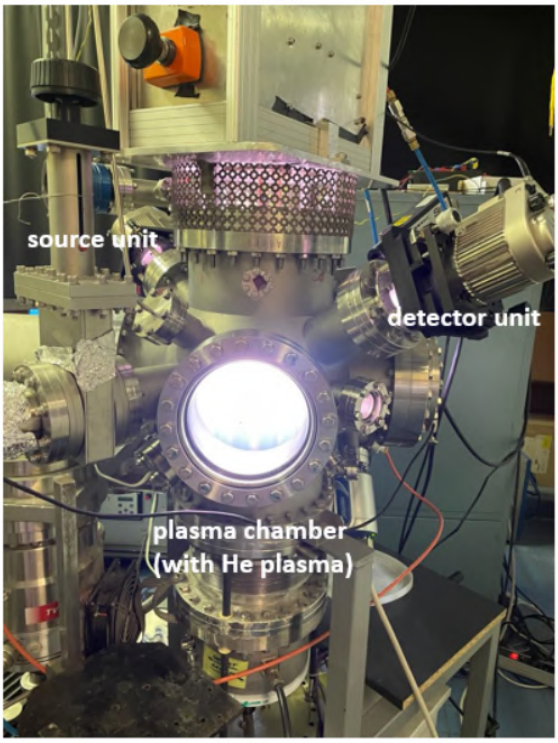


Figure 2.6: Ellipsometer source and detector units installed on the plasma chamber.

call n_i the refractive index of the medium where light impinges on the surface and n_t the one where light is transmitted, and θ_i and θ_t the incidence angle and the transmission angle (with respect to the normal to the surface), respectively, the amplitude reflection coefficients for s and p-polarized light can be expressed by the following:

$$r_s = \frac{E_{rs}}{E_{is}} = \frac{n_i \cos\theta_i - n_t \cos\theta_t}{n_i \cos\theta_i + n_t \cos\theta_t} \tag{2.4}$$

$$r_p = \frac{E_{rp}}{E_{ip}} = \frac{n_t \cos\theta_i - n_i \cos\theta_t}{n_t \cos\theta_i + n_i \cos\theta_t} \tag{2.5}$$

known as Fresnel equations. These equations still hold if the refractive index n is replaced with the complex refractive index N=n+ik, and in this case the amplitude coefficients become complex numbers.

In polar coordinate representation, amplitude coefficients are expressed by:

$$r_s = |r_s| exp(i\delta_{r_s}) \tag{2.6}$$

$$r_p = |r_p| exp(i\delta_{r_p}) \tag{2.7}$$

Upon light reflection on a sample, p- and s-polarizations show different changes in amplitude and phase. The Ψ and Δ measured from ellipsometry are defined from the ratio of the amplitude coefficients for p- and s-polarizations:

$$\rho = \tan\Psi exp(i\Delta) = \frac{r_p}{r_s} = \left(\frac{E_{r_p}}{E_{i_p}}\right) \Big/ \left(\frac{E_{r_s}}{E_{i_s}}\right) \tag{2.8}$$

If we use polar coordinates to represent the amplitude coefficients, it follows that:

$$\tan \Psi = |r_p|/|r_s| \tag{2.9}$$

$$\Delta = \delta_{r_p} - \delta_{r_s} \tag{2.10}$$

which are the quantities measured by ellipsometry.

The ellipsometric measurements present in this thesis were acquired with the *in-situ* Spectroscopic Ellipsometer (iSE, J.A. Woollam), visible in figure 2.6. The polychromatic light source is a quartz tungsten halogen lamp emitting in the 400-1000 nm range, contained, together with a rotating compensator, in the source unit. The light reflected from the surface of the sample is collected by the detecting unit, where it goes through a rotating analyser and is then dispersed by a CCD detector connected to an optical fiber, which can measure simultaneously 190 wavelengths with a temporal resolution of the order of 1 s and a spectral resolution of 3.2 nm. The area of the spot is about 3 mm^2 and the angle of incidence of light is fixed at 61°. A calibration of the system with a 25 nm SiO_2 wafer is realized before measurements.

2.1.4 RF plasma generation

One of the goals of this work is to investigate plasma-surface interactions, for which we expose W and W oxides samples to radio-frequency (RF) generated plasma. The basic principle of creating RF plasma is to apply RF current to a planar coil, that creates an oscillating magnetic field both above and below it. This generates a RF electric field that causes breakdown of the gas, creating the plasma. Under such coupling, there is a transition from capacitively-coupled plasma (CCP) to inductively-coupled plasma (ICP), characterized by an increase in the gas density and emission brightness [53].

The majority of plasma exposures of this work are realized in CAMITER (in French: Carbone et Autres Matériaux pour ITER) experimental set-up (visible in figure 2.7), located at PIIM laboratory.

The experimental set-up consists of a spherical plasma chamber (300 mm in diameter) made of stainless steel, with glass viewports and a quartz window on top (166 mm in diameter and 12 mm thick). The sample holder is a cylinder made of stainless steel that can be moved along the z-axis. On top of it, we put a wafer where the sample is placed. At the beginning of this work, we used a wafer made of W deposited on Si (100) around 0.5 mm thick, on which we put the sample without fixing it (figure 2.8(a)). Later, since it accidentally broke during a transfer operation, we switched to a stainless steel disk around 1 mm thick, and, in order to make optical beam alignment operations easier, we cut an aperture on it, where it was possible to fix the sample to the wafer with W wires (figure 2.8(b)). The sample holder cylinder has a temperature control system, including a backside thermocouple (K-type), resistive heater and circulation of cooling fluid (air or glycol-based liquid), that allows to reach the maximum temperature of around 1073 K. In addition, the wafer can be biased down -1 kV with an external power supply. The wafer is loaded horizontally through a load-lock system (base pressure 1x10^{-6} mbar) without breaking the vacuum of the plasma chamber and fixed by a clamping ring made of Al_2O_3. The vacuum system includes two pressure gauges and two vacuum pumps. One pressure gauge is used to measure residual vacuum, which is usually of around 5x10^{-8} mbar. It is achieved through a primary pump (Alcatel oil rotary pump) followed by a Varian TURBO-V551 turbo-molecular pump.

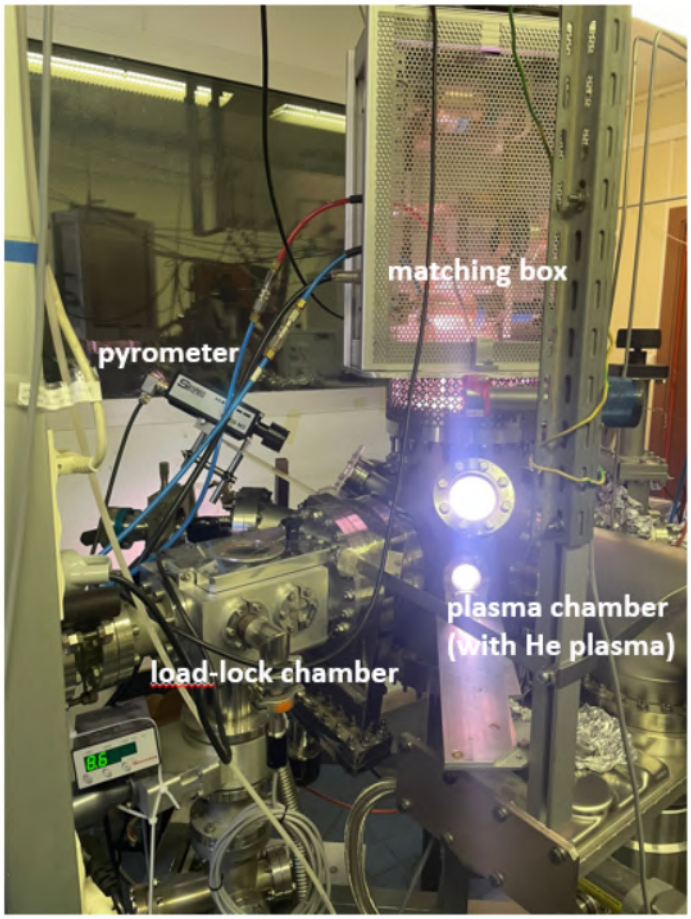


Figure 2.7: CAMITER experimental set-up: plasma chamber, load-lock chamber for samples insertion, capacitance matching box and pyrometer.

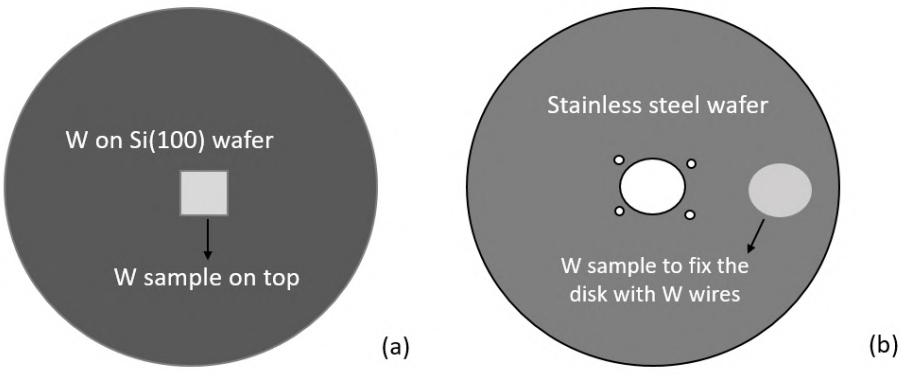


Figure 2.8: Schematic representation of: the W on Si(100) wafer with the W sample placed on top (a) and the stainless steel wafer with the holes to fix the sample (b).

Another gauge (MKS 121A Baratron) is used to monitor pressure in the typical range of plasma operation (0.01-0.1 mbar, which corresponds to an extremely low level of impurities). Various gases with ultra-high purity (99.99 %) can be introduced into the plasma chamber through BROOKS mass flow controllers. The plasma operation pressure is regulated by changing a gate valve placed between the turbo-molecular

pump and the plasma chamber. The mass flow controller voltage is fixed at 5 V, corresponding to a flow rate of 20 sccm.

The RF system used for plasma generation is composed by:

- **RF generator:** a CESAR 1310 Radio Frequency generator (13.56 Hz) whose forward power can be adjusted between 200 and 1000 W.
- **Planar coil antenna**, a three-turn copper coil positioned on top of the quartz window and cooled by a water-circulating system.
- **Impedance matching network:** placed between the antenna and the generator, it has the purpose to maximize power delivery to the plasma and minimize power loss to the antenna. It converts the plasma load impedance to 50 Ω, matching the load impedance of RF generator's output. It is made of two variable copper capacitors C_1 (25-500 pF) and C_2 (10-300 pF), which are adjusted manually in order to minimize the reflected power to 0 W under plasma operation.

The last experiments of this work, which are ellipsometry measurements on W exposed to He plasma (chapter 6.1), are realized in PHISIS, another experimental set-up in PS team of PIIM laboratory, because of technical problems with the heating system of CAMITER. The plasma is still generated in the same way (antenna and RF generator), with the difference that the matching of capacitances is done automatically instead of manually, and other small differences in the experimental set-up (i.e., different distance between the antenna and the sample, presence of a mesh between the antenna and the sample). The ion flux values and other plasma parameters are retrieved from previous plasma characterizations realized in this set-up, described in [54].

RF plasma characterization

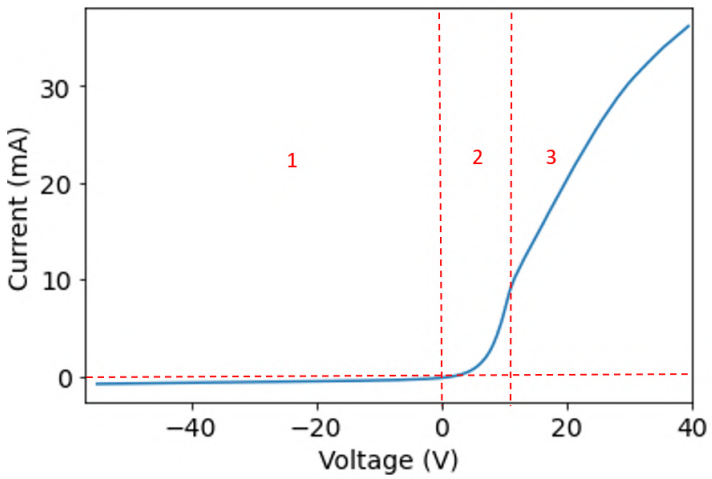


Figure 2.9: Typical I-V curve obtained with a Langmuir probe (in this case, for D plasma).

Langmuir probe measurements are performed on D and He plasma in order to have a basic knowledge of the plasma parameters, such as electron density, electron temperature and plasma potential, in a gas pressure range of 2-10 Pa and in a RF power range of 300-1000 W. The Langmuir probe that we use consists of a tungsten tip 6.5 mm long and with a radius of 0.1 nm, inserted horizontally as closer as possible to the sample surface and electrically biased to the ground. A voltage scan between -55 V and 40 V is realized for different combinations of pressure and RF power. Every I-V scan gives an I-V curve as in figure 2.9. In the region 1, in which the voltage probe is negative, the plasma sheat is mainly constituted of ions, as electrons are repelled by the negative voltage. The current saturates to a minimum value called ionic saturation current. In region 2, the curve slope rises, as ions start to be outnumbered by electrons and, as those are faster than ions, some of them start reaching the probe. This can be seen as a region of exponential growth, and computing the first derivative maximum of this curve allows to access the values of plasma potential V_p. The floating potential V_f is then the potential when the current value is 0. Finally, in the region 3 the voltage is strongly positive, repelling the ions, and the sheath is mainly made of electrons. To calculate electron temperature T_e, we make the approximation that the electron distribution function is a Maxwellian, thus we can define the electronic current as:

$$I_e = I_{e,sat} \exp \frac{-e(V_{LP} - V_p)}{k_B T_e} \tag{2.11}$$

where V_{LP} is the Langmuir probe voltage, and the electronic saturation current $I_{e,sat}$ corresponds to the region where the electronic sheath is established, i.e. $V_{LP} = V_p$. The previous equation can be written as:

$$\ln \frac{I_e}{I_{e,sat}} = \frac{-e(V_{LP} - V_p)}{k_B T_e} \tag{2.12}$$

The logarithm plot of this equation as a function of the voltage gives a linear curve. From the slope of such curve, we can derive the electron temperature T_e (as e and k_B are known constants). Once computed T_e, it is possible to calculate the electron density n_e, as the electron saturation current can be written like:

$$I_{e,sat} = \frac{n_e}{4} e v_e A = \frac{n_e}{4} e A \sqrt{\frac{8 k_B T_e}{m_e}} \tag{2.13}$$

Once we have access to the values of electron temperature and density of the plasma, since the plasma is globally neutral (i.e., $n_i = n_e$), the ion fluxes values are computed using the following relation:

$$\Phi_i = 0.6 \cdot n_e \cdot \sqrt{\frac{T_e}{m_i}} \tag{2.14}$$

where n_e and T_e are electron density and temperature in m^{-3} and J respectively, m_i is the ion mass ($2 \cdot m_H$ for D ions and $4 \cdot m_H$ for He ions), and 0.6 is just a factor deriving from the multiplication of physical constants. It is important to specify that only electron temperature T_e appears in the previous expression, as in the present case we are dealing with cold plasmas ($T_i \simeq 300K = 25\text{meV}$), therefore the contribute of ion temperature is negligible.

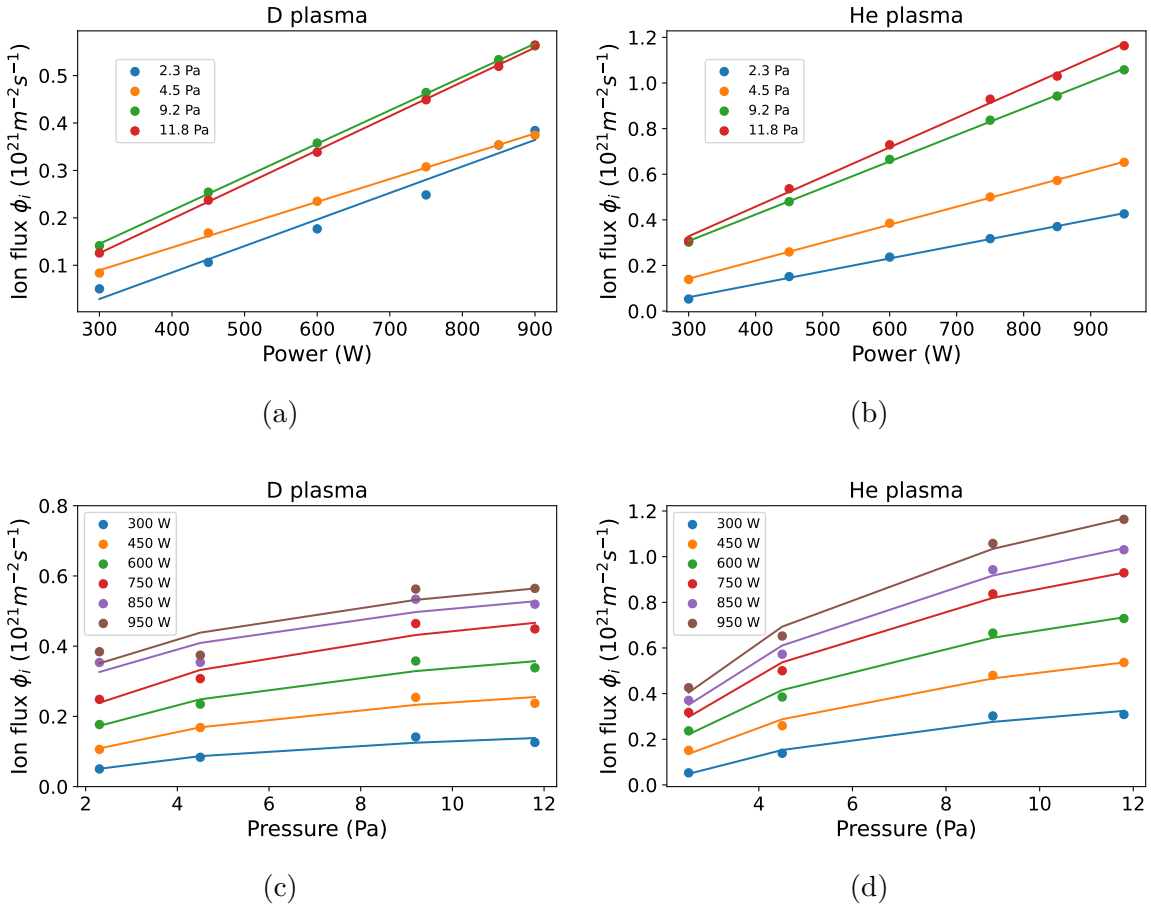


Figure 2.10: Ion flux plots as a function of power and pressure for D (a,c) and He (b,d) plasma. The points refer to the experimental data while the solid lines refer to a linear fit (in the case of the power plots) and a logarithmic fit (in the case of the pressure plots).

Assuming the model described in [55], the expected trends of the measured quantities are the following: T_e is expected to be constant with power and inversely proportional to pressure, while n_e is linearly proportional to power and depends on pressure as in a logarithmic way (the fit in figure 2.10 is realized assuming $\propto ln(p^{3/2})$). The reason of this behaviour is that RF power influences mainly the electron density n_e, keeping the average electron energy $k_B T_e$ constant, while increasing the gas pressure (thus, increasing the density of neutral species) will decrease the electron mean free path, therefore increasing collisions and resulting in a lower average electron energy $k_B T_e$.

Figure 2.10 represents the plot of ion fluxes obtained from Langmuir probes measurements for both D and He plasma, as a function of pressure and power. As we can see, as the flux is linearly proportional to the electron density, it keeps the same dependencies from power and pressure (e.g., linear increase with power and logarithmic trend with pressure). As before mentioned, from Langmuir probe measurements we can also extract the plasma potential V_p and the floating potential V_f, from which we can derive the energy of the ions. In the case the sample is floating (not biased, as it is the case for most plasmas of this work), the ion energy is E_{ion}=e$(V_p - V_f)$.

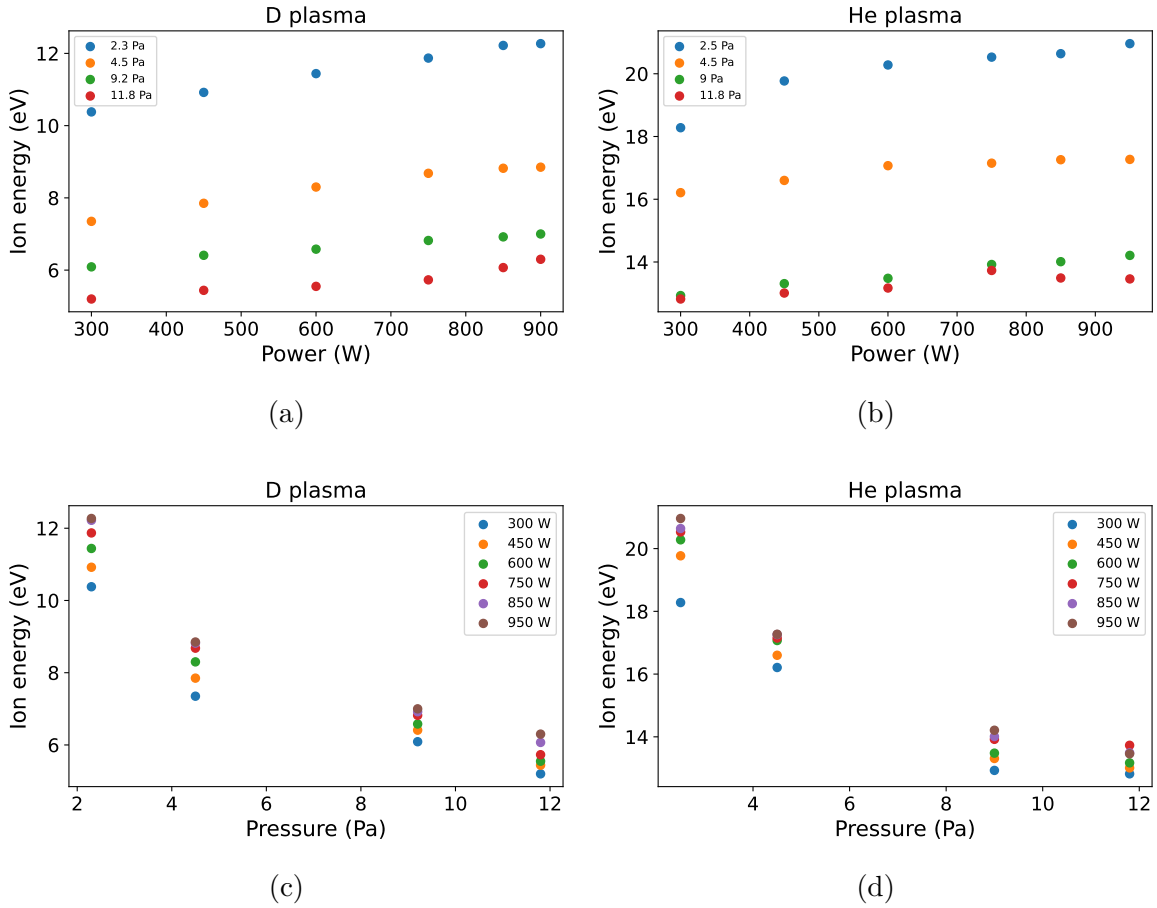
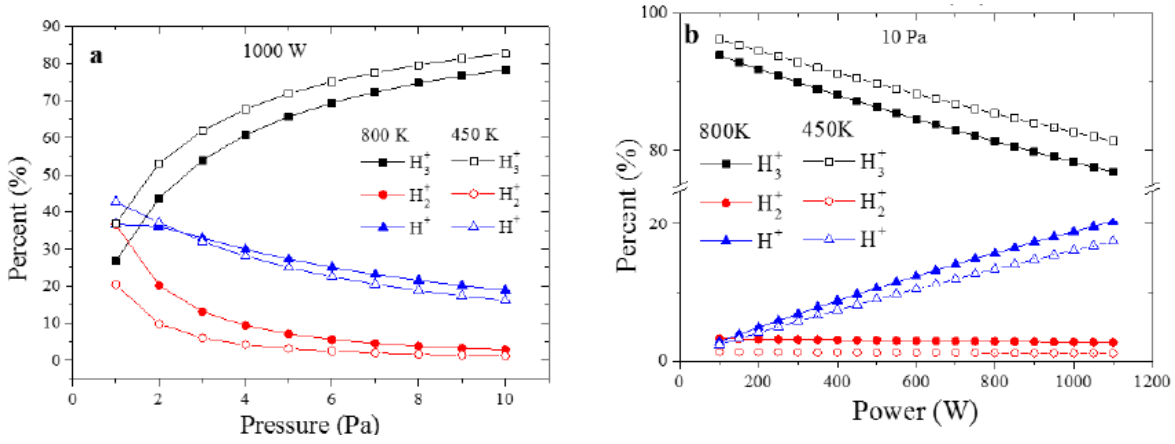


Figure 2.11: Ion energy plots as a function of power and pressure for D (a,c) and He (b,d) plasma.

If a bias V_{bias} is applied, the ion energy will be E_{ion}=e($V_p - V_{bias}$). It is also important to keep in mind that the ion energy is not a constant value, but the average of a Maxwell-Boltzmann distribution function, which is the solution of the Boltzmann equation for a plasma in an equilibrium state [56]. Usually, the ion energy distribution has a peak width of about 1 eV and an asymmetric tail at lower energies that becomes more important with increasing gas pressure (because of increasing number of collisions, causing a bigger presence of lower energy ions). The ion energies values (obtained from the plasma potential values measured with Langmuir probe) are in the range of 5-12 eV for D plasma and of 12-22 eV for He plasma. As expected, the ion energy is approximately constant with RF power and decreases with increasing gas pressure (figure 2.11). At higher pressures, in fact, the number of collisions increases, resulting in energy loss.

It is also important to know which is the dominant ion species in the plasma. For D plasma, we rely on previous plasma characterization studies realized in the same set-up by [53], which determined the percentage of H^+, H_2^+ and H_3^+ in the total ion density (results are equivalent for D plasma). We can see from figure 2.12 that D_3^+ is the dominant ion species for pressures higher than 2 Pa and fixed RF power, follwed by D^+ and D_2^+. D_2^+ has an opposite trend of D_3^+ with power and pressure, which can be explained by the fast conversion of D_2^+ in D_3^+ when colliding with D_2, reaction which

is favoured at higher pressures. After impact on the surface, then, the $D_3{}^+$ molecules dissociate into 3 D^+ ions, each carrying 1/3 of the molecule energy. For He plasma, the dominant ion species is He^+, as the second ionization energy for He atoms is quite high (54.4 eV), making it highly unlikely to have He^{2+} ion species.



(a) (b)

Figure 2.12: Contribution of H^+, H_2^+ and H_3^+ to the total ion population, as a function of pressure (a) and power (b), for two gas temperatures [53].

In addition, during plasma exposures, the emission spectra in the visible-NIR range are recorded with a light collimator (connected to a spectro-photometer by an optical fiber). The atomic emission lines of the chemical elements present in the plasma are identified using the NIST database [57]. In this way, it is possible to identify the emission lines of the plasma gas and also to detect the possible presence of impurity, which could suggest the presence of a leak or other experimental problems.

2.1.5 Imaging techniques

The first two techniques here described, Confocal Microscopy and AFM, are used to characterize the morphology of a specific area of the sample surface and to extract roughness values relative to that area. As one technique (Confocal Microscopy) uses light to probe the surface, while the other (AFM) exploits the interatomic force between a tip and the sample, the roughness parameters extracted from the two should be adequately distinguished.

In both cases, roughness is calculated as root mean square (RMS) of the heights distribution of the scanned area, through the formula:

$$\rho = \frac{1}{N}\sum_{n=1}^{N}(z_n - \bar{z})^2 \tag{2.15}$$

where $\bar{z}$ is the height mean value and N is the number of line scans along the x axis (especially in AFM, data are usually collected as line scans along x axis). It is straightforward from the equation above that the RMS roughness values extracted from the images strongly depend on the size of the scanned area.

Confocal Microscopy allows to scan areas of the order of a few mm (with different magnifications depending on the objective used), which are closer to the diameter size

of the optical beams used in this work (both the supercontinuum laser for reflectometry and the ellipsometric light source). Hence, they will be more representative of the whole sample surface, but will also result in bigger roughness (due to the intrinsically statistic nature of roughness determination) and have a lateral resolution of a few hundreds nm. On the other hand, it is important to take into account also the wavelength range of the used optical methods (400-1000 nm). For this reason, AFM is used to accompany Confocal results, as it allows to scan smaller areas (40x40 μm^2 maximum), and thus to measure roughness variations at scale compared to the light wavelength. Therefore it allows to take into account smaller surface structures, as the lateral resolution is higher than in Confocal Microscopy (same order of the tip radius, in this study around 10 nm).

Confocal Microscopy



Figure 2.13: Schematic image of S-neox SENSOFAR Confocal microscopy instrumental set-up [58].

Confocal Microscopy is an optical imaging technique which allows to obtain 2D images of a surface as well as its 3D topography. As visible in figure 2.13, it uses the light coming either from a laser or from a LED, which is collimated and directed to a micro-display by a beam splitter. Each pixel of the microdisplay projects the light through a field lens and an objective, and illuminates a single point of the sample surface. The light reflected from each point is then directed by another beam splitter to a high resolution CCD detector (1360x1024 pixels). The surface is scanned in lateral direction by pointing the light beam on the sample through a pair of galvanometric mirrors, which allow sample stage moving. The image of the topography

(height measurement) is obtained by collecting a series of 2D images at different focal planes, while moving the objective along z-axis. The collected images are then combined together and called z-stack, and they can be processed to deduce the height of each point by the maximum intensity. The instrument can reconstruct an image of a certain area by stitching several fields of view obtained during the sample stage movement. Such technique allows to have higher resolution compared to traditional optical microscope (≃0.1 µm), as the out-of-focus light is removed through a confocal pinhole, thus recording a signal for each focal plane and creating a background-free image.

For this thesis, a S-neox SENSOFAR confocal microscope was used. It is equipped with four different LEDs (blue, green, red and white), but the green one (530 nm) was mainly used, since the instrument performance is optimized for it. There are also four objectives (5x, 20x, 50x, 100x) which allow to obtain images with different fields of view and optical resolution. After the acquisition, the images are corrected using the software SENSOSCAN 6.7 and Mountain [59]. The analysis procedure of a raw 3D image is the following:

- Subtraction of a mean plane, in order to correct possible inclinations of the sample or the sample stage with respect to the focus plane.
- Filtering the image in order to correct possible large-scale variations of the surface profile. In this work, a Gaussian filter is used, which allows to distinguish between local roughness and waviness profiles of the surface. The threshold size value is chosen depending on the image size and on the dimensions of the structures we are interested in observing at a smaller scale (roughness profile, as the one depicted in figure 2.14(b)).
- Finally, the topography parameters of the selected area are obtained (table in figure 2.14(b)): S_a and S_q, respectively the average and the root mean square roughness. Mainly S_q is used as parameter to evaluate the surface roughness.

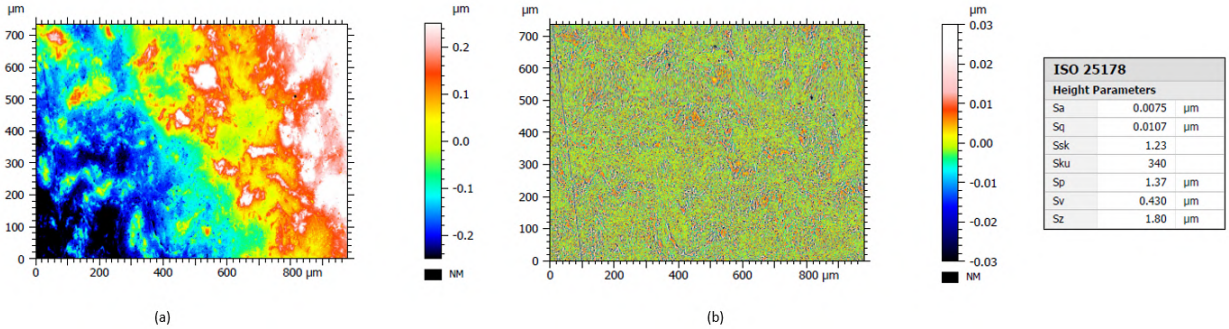


Figure 2.14: An example of CM images of a W sample: raw image (a) and corrected image with roughness parameters table (b).

Atomic Force Microscopy (AFM)

Atomic Force Microscopy (AFM) can be encountered among the scanning probe microscopy techniques, in which the information is gathered by sensing the surface with

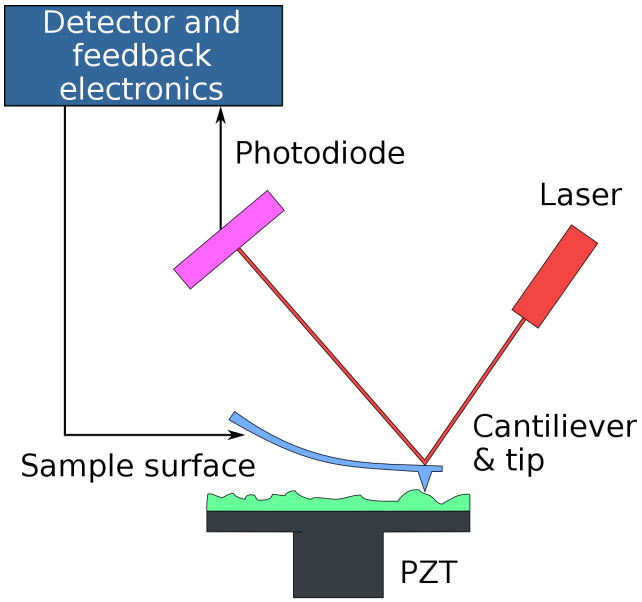


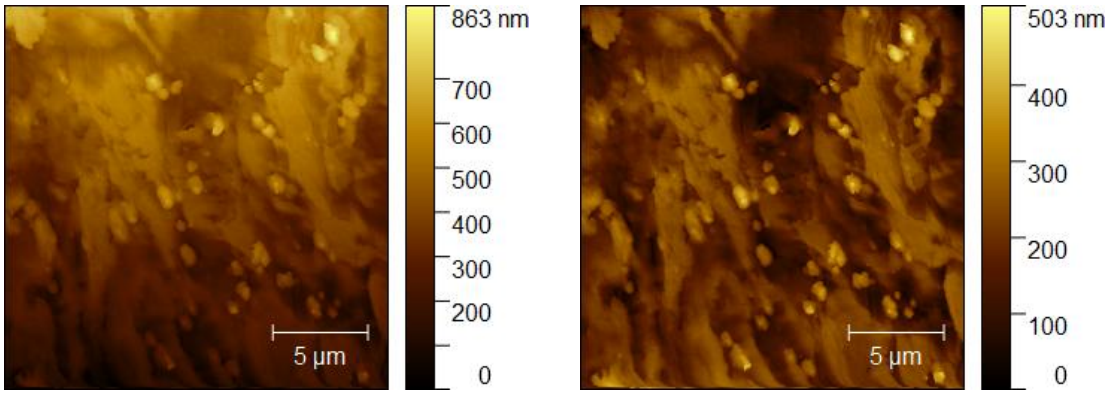
Figure 2.15: A simplified scheme of AFM instrumental set-up [60].

a mechanical probe (tip). In particular, AFM uses the interatomic force between the tip and the sample to form a 3D topography image of the surface, resulting in a much higher resolution than optical microscopy techniques. The AFM experimental set-up (figure 2.15) consists of a sharp tip attached at the end of a cantilever, used to scan the surface. The AFM measurements of this work were realised on a AFM NT-MDT, using a silicon tip with a curvature radio of about 10 nm, which corresponds to the lateral resolution of the technique. The vertical resolution is estimated to be around 0.1 nm. When the tip is brought in proximity of the surface (0.1-100 nm), the interatomic forces between the tip and the sample lead to a deflection of the cantilever, which is evaluated from the deflection of a laser beam impinging on the back of the cantilever and reflected on a photodiodes matrix (the two signals are proportional). The AFM can be operated in different modes, generally distinguished between static (or contact) modes and dynamic (non-contact or "tapping") modes, where the cantilever vibrates at a given frequency. In this work, the "tapping" mode is used: the cantilever is driven to oscillate near its resonance frequency via a small piezoelectric element in the cantilever holder. The amplitude of cantilever oscillations is constant as long as there's no interaction with the surface and starts to vary once the tip is approaching the surface. The change in cantilever's oscillations amplitude is used as a parameter in the electronic feedback loop that controls the height of the cantilever above the sample. The loop adjusts the height of the sample in order to maintain a fixed amplitude of cantilever oscillations as this one is scanned over the surface. The AFM image obtained at the end consists in a height map, in which each height corresponds to a constant force between the tip and the surface during the intermittent contacts [61]. In this work, the AFM images are measured at approximately the center of the studied sample, scanning different area sizes (from 2x2 to 40x40 μm^2). Each image is then corrected using the software Gwyddion via the following procedure:

- Plane levelling: the plane is computed from all the image points and is subtracted from the data. If more complicated structures are present, three point levelling

is preferred, as the plane is computed from three selected points in the image that should be at the same level.

- Polynomial background subtraction, in which it is possible to select the polynom degree (usually fixed at second order). This step is preferred to the first one when the surface presents 2D irregularities (e.g., bowed structures), for which a plane levelling is not accurate enough.
- Align rows: usually the median algorithm is used, based on finding the median of each scan line and subtracting it, thus moving the lines to the same height. This is done in order to correct the possible shift or slightly different slope of the profile taken in the fast scanning axes.
- Remove scars: the parts of the image corrupted by local faults of the closed loop (usually parallel to the fast scanning axis) are removed, using neighbouring lines to "fill-in" the gaps.
- Fix zero: adds a constant to all the data to move the minimum value to zero.



(a) (b)

Figure 2.16: An example of AFM images of a W sample: raw (a) and corrected (b) image.

Figure 2.16 shows the comparison between two AFM images, before and after corrections.

Scanning Electron Microscopy (SEM)

Scanning Electron Microscopy (SEM) allows to image the surface of a material with a nanometric resolution, since it uses as a probe a focused beam of high energy electrons instead of light. From the De Broglie relation, in fact:

$$\lambda = \frac{1.2398}{E} \tag{2.16}$$

where E is the particle energy in eV and λ is the particle wavelength in µm. Thus, for 1 keV electrons the corresponding wavelength is of about 1.2 nm, allowing then a resolution at a nanometric scale.

The electron microscopy analysis (both SEM and FIB) was performed at CP2M laboratory in Aix-Marseille University, under the supervision of Céline Martin, Andrea Campos, Martiane Cabié and Thomas Neisius. The Zeiss Gemini SEM 500 experimental set-up consists in an electron column, which contains an electron gun that generates and accelerates electrons in vacuum (base pressure: 10^{-6} mbar) with an energy in the range 0.1-30 keV, optical lenses to focus and scan the electron beam on the surface of the sample, and the detectors for signal collection. The interaction the electrons beam with the material gives rise to signals of different nature [62], each one providing a different kind of information (morphology, topography, chemical composition, crystallinity):

- **secondary electrons (SE):** these are valence electrons of the atoms of the material that are ejected from inelastic scattering with the incident electron beam. They have energy of 0-10 eV and they come from a depth of around 1-10 nm from the surface. They provide information about the topography of the surface: as their emission yield strongly depends on the tilt of the surface, different inclinations of surface structures will give rise to a color contrast. In particular, peaks and protruding objects will appear brighter, while hollow structures and pits will appear darker.

- **back-scattered electrons (BSE):** these are electrons from the incident beam which are elastically retro-diffused by the atoms of the sample, thus they have the same energy of electron beams (1-30 keV). They are detected close to the incident beam direction by a ring solid-state detector placed above the sample. They probe a depth of few hundreds of nm and their emission yield is a function of the atomic number Z of the sample material. A BSE image will appear as a Z contrast image, where brighter areas correspond to higher Z areas of the surface, while darker areas to lower Z (as it is possible to see in figure 2.17). They can also provide information about the crystallinity of the material as, for example, different crystalline grains of the same material have different BSE intensities due to their different crystal orientation.

- **characteristic X-rays**, generated from the ionisation of the atoms of the material by the incident electron beam, which occurs within about 1 µm below the surface. Their emission energy is characteristic of the material, thus allowing the chemical characterization of the surface.

- **diffraction of back-scattered electrons (EBSD):** this phenomenon is used to study the crystal phase and orientation of a sample. It can be obtained by tilting the sample as much as possible (in our case, by 70°) in order to maximize the probability of diffraction of the electrons. Electrons that are scattered by atoms close to the surface and electrons that penetrate deeper in the crystal (channeling effect) before being scattered are re-emitted from the surface, creatinga flat cone distribution. Each atomic plane creates two cones of intensity, one related to the electrons diffracting from the front, the other one from the back. The two cones intercept the imaging plane of the EBSD detector (phosphor screen and CCD camera) and appear as two straight lines separated by a double Bragg angle. The EBSD pattern is composed of the lines from all the atomic planes, which will have different intensities because of different angles between the incident and

scattering beams. The intersection points on the EBSD pattern are called zone axis and represent specific crystallographic directions, which will be evidenced by a color map. In figure 2.18 (b), for example, red color denotes grains with orientation close to (100), blue to (111) and green to (101).

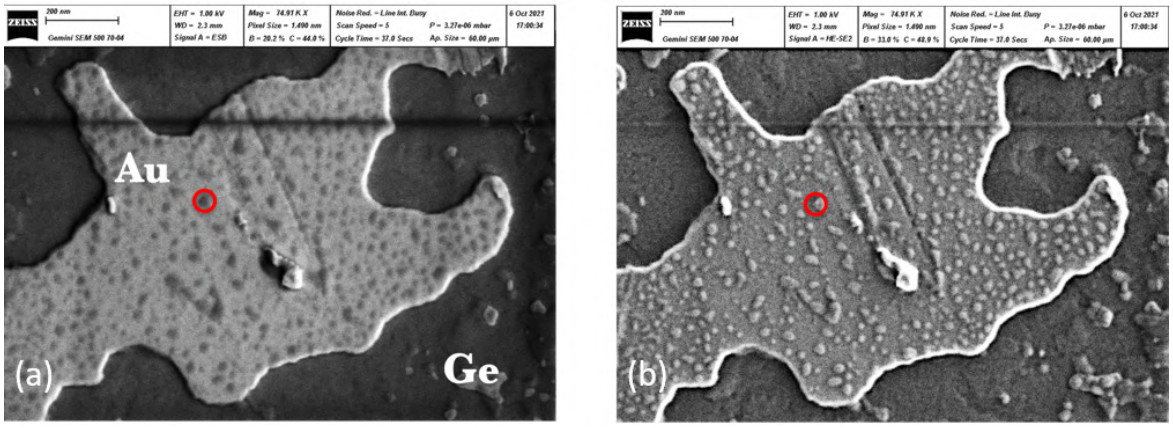


Figure 2.17: SEM image in BSE mode (a) and SE mode (b) of a thin Au film on Ge(111) surface upon annealing [63].

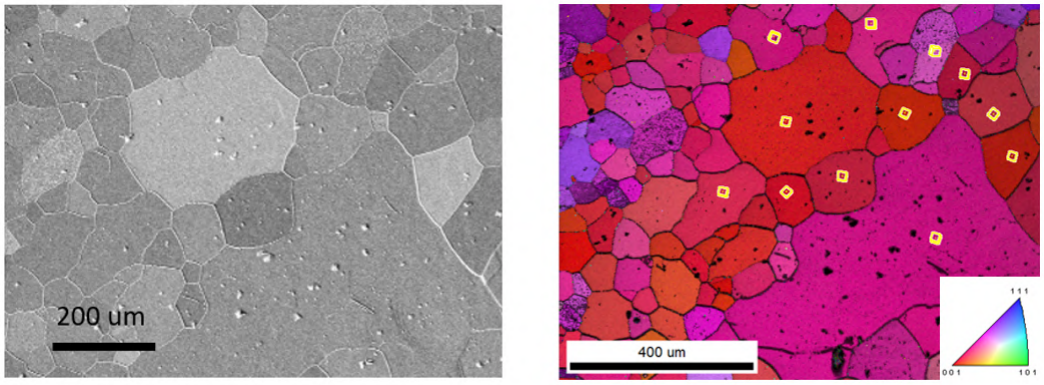


Figure 2.18: SEM images of a He exposed W surface acquired by different detectors: SE image (a) and EBSD pattern (b).

Focused Ion Beam (FIB) technique for thickness measurements

FIB and cross-section SEM measurements are performed on W samples after thermal oxidation, in order to measure the oxide layer thickness. A FEI Helios 600 nanolab Dual Beam instrument is used, equipped with an electron and ion guns (separated by 52°) and coupled with a SEM, which allows to chose the area where to perform the cut and, after tilting the sample, to evaluate the thickness of any present surface layer. In our case, we chose an area correspondent to the center of the sample. A protection layer is realized first by an electron-induced deposition of Pt (3 kV, 1.4 nA) for 200 nm, and secondly by an ion-induced deposition of Pt (5 kV, 0.17 nA)

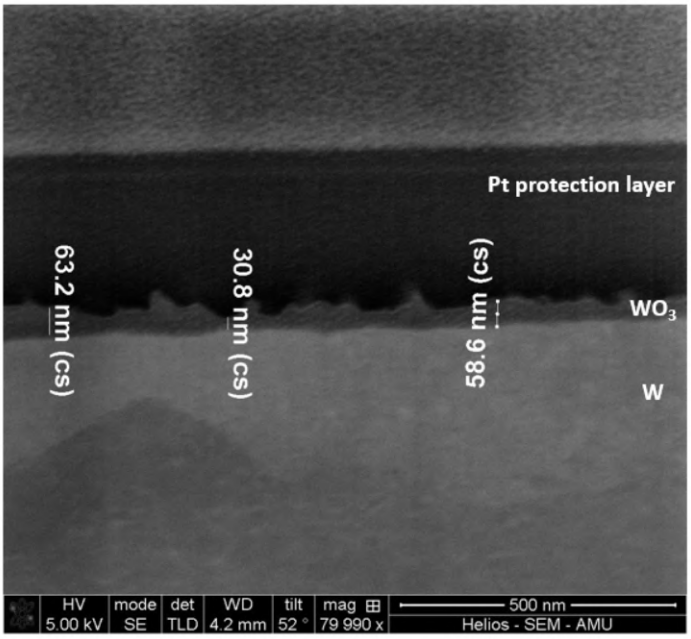


Figure 2.19: Cross-section SEM view of WO_3 layer on W substrate (with the Pt protection layer on top).

for 500 nm, forming around 700 nm of Pt protection layer. This is fundamental to prevent additional damage during the cut. Then, a volume of 15x2x6.78 μm^3 is cut by a focused beam of Ga ions with an energy of 30 keV. The sample is then tilted to separate the lower and upper side part of the lamella from the sample, and it is possible to have a SEM cross-section view of the sample (in our case, W substrate with the oxide layer and the Pt deposit on top, as visible in figure 2.19), due to the contrast difference between the components.

An estimation of oxide layer thickness is realized through the software ImageJ, where it is possible to correct the tilt (52°) and to evaluate the final thickness values from a statistical average on many images (and, in each image, on many areas of the layer). Their associated error is the statistical one. As it is possible to see in figure 2.19, oxide growth was quite inhomogeneous (with thickness sensibly varying depending on the W grain where the oxide grows), giving rise to a wide distribution of values.

2.1.6 X-rays Photoelectron Spectroscopy (XPS)

X-rays Photoelectron Spectroscopy (XPS) is a surface-sensitive technique based on the photoelectric effect, used for compositional characterization of a sample. Not only it allows to identify the elements present within a material, but also their chemical state as well as the overall electronic structure and density of electronic states [64]. It consists in irradiating a sample with monochromatic X-rays source (usually Mg Kα at 1.253 keV or Al Kα at 1.486 keV) and analyzing the kinetic energy of the photoemitted electrons, which is given by:

$$E_k = h\nu - (E_b + \phi) \tag{2.17}$$

where hν is the energy of the X-ray photon, E_b is the binding energy of the atomic orbital from which the electron is expelled, and ϕ is the spectrometer work function. Since each element has a unique set of binding energy, XPS can be used to identify elements in the surface and to quantify their concentration. Also, variations in the binding energy, arising from difference in the chemical environment, can be used to identify the chemical state of the analyzed material (e.g., metallic or oxidized). The X-rays photons have a penetration depth of about 1-10 µm below the surface of a solid, causing the ionization of the atoms of the material (emission of core electrons). However, only the core electrons which are emitted within the first few nm can leave the surface without any energy loss. These are the electrons detected by the technique and producing sharp peaks in a typical XPS spectrum, while the electrons that undergo inelastic scattering constitute the background, consequently making XPS a surface analysis technique.

The XPS measurements present in this work are realized with an high intensity Mg anode X-rays source (PREVAC) emitting at 1.2536 keV, described in [65]. The analyzed samples are fixed onto a sample-holder by a Mo mask and placed inside a mu-metal ultra-high vacuum chamber (base pressure: 1×10^{-10} mbar). Photoelectrons are detected via a high resolution electron energy analyzer (Scienta Omicron R3000), composed of an high transmission electron lens with an acceptance angle of 30° and a 40 mm MCP detector monitored by a FireWire CCD camera. The resolution of the XPS spectrometer, determined from the full width at half maximum of the Ag 3d core levels of a clean Ag single crystal, is of 0.9 eV.

A typical XPS spectrum is a plot of the intensity of detected photelectrons versus their kinetic energy (which can easily be converted to their binding energy). The characteristic XPS peaks (photoelectrons lines) correspond to the configuration of the electrons within the atoms (e.g., 1s, 2s, 2p, including also the spin-orbit splitting for orbitals different from s). The intensity of each peak is directly related to the amount of the element within XPS sampling volume, with a detection limit of about 0.1-1%. In the peak-fitting process of XPS spectra, as represented in the example figure 2.20, the following features were taken into account:

- full width at half maximum (FWHM) of photoelectrons lines (about 0.5 eV wider for insulators compared to conductors).
- asymmetry of photoelectrons lines (typical of pure metals, due to the coupling with conduction electrons).
- identification of "shake-up" lines, which are just satellite peaks a few eV lower in kinetic energy (higher in binding energy) with respect to the main peak, due to a possible excited state of the ion (a few eV above the ground state) following the photoelectric process. The displacement and relative intensity of shake-up lines can be useful to identify the chemical state of an element.

2.2 Models

The following paragraphs describe the optical models use to determine the optical constants n,k (namely, the refractive index n and the extintion coefficient k) of the

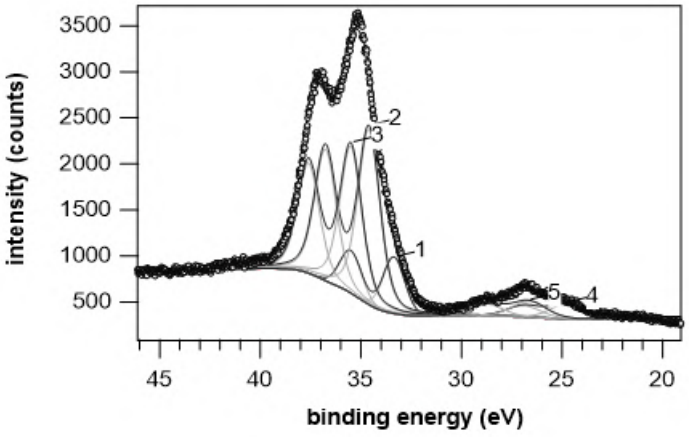


Figure 2.20: Example of a fit of the XPS spectrum of the W 4f peaks of a WO_3 sample.

different analyzed materials, as well as the layer thickness in the case of multi-layer systems, and other properties such as roughness and inclusions volume fraction in the case of, respectively, rough surfaces and He implanted materials.

2.2.1 Bulk W samples

For bulk W samples, the optical constants n,k are obtained directly from the measured values (Ψ, Δ). Those are called "pseudo"-optical constants, as they are calculated from an optical model that assumes a perfectly flat substrate with infinite thickness and no surface layer on top (hence, assuming the absence of multiple reflections). If the external medium is air (ϵ_{air}=1), the complex pseudo-refractive index N of the material is given by:

$$\epsilon = \epsilon_1 + i\epsilon_2 = (n+ik)^2 = sin^2(\theta) + \left[1 + \tan^2(\theta)\left(\frac{1-\rho}{1+\rho}\right)^2\right] \tag{2.18}$$

where θ is the incident angle of light (with respect to the normal to the surface) and ρ is defined in 2.8.

The pseudo-optical constants are equal to the the true ones if surface roughness and the thickness of any surface layer are negligible: in this case, it is possible to consider the material as an opaque layer where only one reflection occurs. For the bulk W samples analyzed in this work, the native oxide thickness is estimated to be <5 nm (from XPS measurements) and the surface roughness is estimated to be <10 nm (from Confocal microscopy measurements over an area of a few hundreds µm), hence it is reasonable to assume pseudo-optical constants to be the real ones. Furthermore, in order to validate this assumption, we have compared the reflectivity calculated from the n,k obtained from [66] and the reflectivity obtained from the pseudo-optical n,k directly extracted from the measured Ψ and Δ, and found that the behaviour of the "pseudo-optical" reflectivity was closer to the reflectivity spectra previously measured on similar samples with direct reflectometry techniques. Hence, those are then used to model the optical constants of W as a substrate, for following experiments in which other coatings (such as W oxide layers) are present on it.

2.2.2 Optical interference model for multi-layer system

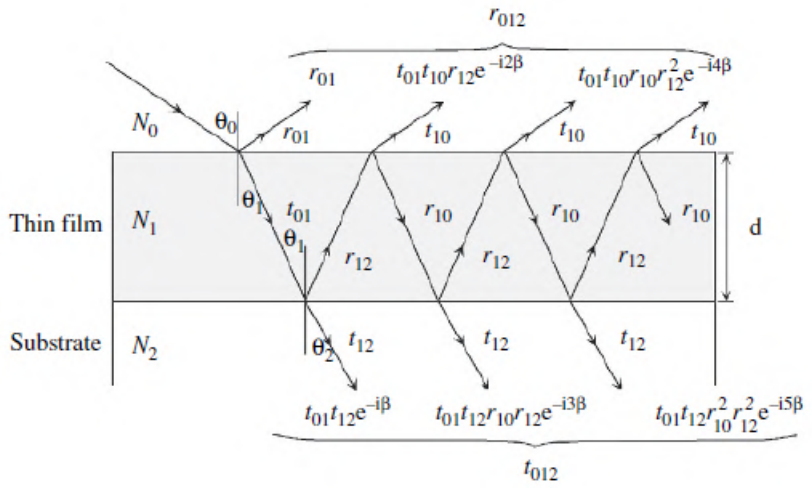


Figure 2.21: Optical model for an air/thin film/substrate structure [51].

This model is used to calculate the overall reflectivity of a system where one or more layers are present on a substrate (e.g., He-implanted porous layer on W substrate). In this case, if light absorption within the films stack is weak, the incident wave is reflected (and transmitted) at every interface, and optical interference occurs (as visible in figure 2.21). The amplitude of reflection and transmission coefficients at each interface are:

$$r_{jk,s} = \frac{N_j \cos\theta_j - N_k \cos\theta_k}{N_j \cos\theta_j + N_k \cos\theta_k} \qquad r_{jk,p} = \frac{N_k \cos\theta_j - N_j \cos\theta_k}{N_k \cos\theta_j + N_j \cos\theta_k} \tag{2.19}$$

$$t_{jk,s} = \frac{2N_j \cos\theta_j}{N_j \cos\theta_j + N_k \cos\theta_k} \qquad t_{jk,p} = \frac{2N_k \cos\theta_j}{N_k \cos\theta_j + N_j \cos\theta_k} \tag{2.20}$$

The incidence and transmission angles at each interface can be obtained by applying Snell's law:

$$N_j \sin\theta_j = N_k \sin\theta_k \tag{2.21}$$

The phase variation β between each layer and the interface is expressed by:

$$\beta = \frac{2\pi d_j}{\lambda} N_j \cos\theta_j \tag{2.22}$$

By multiplying the phase variation and amplitude coefficients at each interface, we obtain the reflected wave at each interface $t_{jk}t_{kj}r_{kj}exp(-i2\beta)$. The amplitude reflection coefficient for the whole structure of air/thin films/substrate is expressed by the sum of all the reflected waves.

In the case of only one layer on a substrate, it is possible to calculate analytically the reflectivity of the system. This will be equal to:

$$r_{012} = \frac{r_{01} + r_{12}exp(-i2\beta)}{1 + r_{01}r_{12}exp(-i2\beta)} \tag{2.23}$$

From this, we obtain the reflectivity of s and p polarized waves as follows:

$$R_s = |r_{012,s}|^2 \qquad R_p = |r_{012,p}|^2 \tag{2.24}$$

In the case of more than one layer on a substrate, the problem must be solved in a numerical way, performing the calculation upward from the substrate.

2.2.3 Bennet-Porteus model for surface roughness

The reflectivity from a rough surface can be derived, among all, by the Bennet-Porteus model, extensively described in the paper [67]. It describes the relation between reflectivity (considered as a sum of specular and diffused components) and the root mean square roughness σ, defined as the root mean square deviation of the surface heights distribution. The model, however, is valid under specific assumptions:

- σ is small compared to the light wavelength λ.
- The surface is perfectly conductive and hence would have a specular reflectivity equal to 1 if it was perfectly smooth.
- The heights distribution of surface irregularities is Gaussian, with a standard deviation σ.
- The autocovariance function of surface irregularities is also Gaussian, with a standard deviation a.

The complete expression for the measured reflectivity R of a rough surface is then:

$$R(\lambda, \delta, \sigma) = R_{eff}(\lambda, \delta) exp[-(4\pi\sigma/\lambda)^2] + R_{eff}(\lambda, \delta) \frac{2^5\pi^4}{m^2} (\sigma/\lambda)^4 (\Delta\theta)^2 \tag{2.25}$$

where R_0 is the specular reflectivity of a perfectly smooth surface of the same material, $\Delta\theta$ is the instrumental acceptance angle and the autocovariance length a is defined as $a = \sqrt{2}\sigma/m$, where m is the root mean square of the surface profile.

It is straightforward from equation 2.25 that the diffused reflectivity component R_{diff} can be neglected when $\sigma << \lambda$, hence when surface roughness values are much smaller than the working wavelength range.

2.2.4 Effective medium approximation (EMA) model

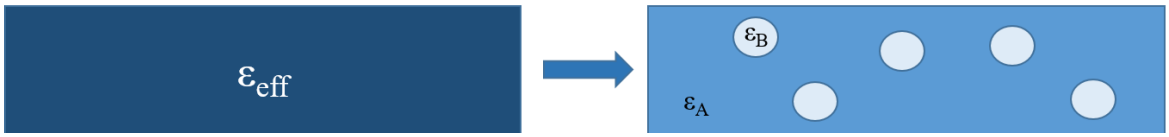


Figure 2.22: Schematic depiction of the EMA layer.

To model a layer in which two different material phases coexist, we have used the so called effective medium approximation (EMA) layer, which has a dielectric function that depends on the single dielectric functions of the constituents materials and on

their volume fraction [68]. From a general point of view, if the two material phases are called A and B and their dielectric functions ϵ_A and ϵ_B, respectively, the EMA layer will have the following dielectric function:

$$\epsilon_{eff} = \epsilon_A \frac{2\delta(\epsilon_B - \epsilon_A) + \epsilon_B + 2\epsilon_A}{\epsilon_B + 2\epsilon_A - \delta(\epsilon_B - \epsilon_A)} \tag{2.26}$$

where δ is the volume fraction of B in A. In the present study, we have used EMA model in the approximation of Maxwell-Garnett, which assumes that the material phase of ϵ_B is surrounded by the phase of ϵ_A, and their volume ratio determines δ. In addition, the inclusions of the material phase B are assumed to be perfectly spherical.

The validity of effective medium theories is limited to specific conditions, namely:

- the size of inclusions in the composite material is sufficiently great than atomic size, but smaller than $\lambda/10$ of the wavelength
- the dielectric functions of the material phases are independent of size and shape

Furthermore, in general terms, the Maxwell Garnett EMA is expected to be valid at low volume fractions δ, since it is assumed that the domains are spatially separated, and electrostatic interaction between the chosen inclusions and all other neighbouring inclusions is neglected.

Chapter 3

Reflectivity measurements on W as a function of roughness and temperature

This chapter investigates the change in W reflectivity in the visible and near-infrared domain (500-1100 nm), as a function of temperature (in the range 300-1073 K) and of surface roughness (in the range 20-100 nm). The interest for W optical properties is recently growing, especially in research fields such as fusion [69] and aerospace applications [70, 71]. In particular, in fusion reactor environments such as ITER, where W will be used as a material for both divertor and first wall components, the interaction with high ion fluxes and heat loads could induce temporary or permanent changes in its optical response. Previous studies have proved that the interaction of charged particles with W can induce material modifications, from microscopic lattice defects to mesoscopic damages, such as surface blisters [72] and near-surface bubbles [73, 74]. Those defects often evolve upon thermal annealing and can be responsible for a modified fuel inventory in the reactor walls [75]. Therefore, the plasma-wall interaction can modify the roughness of W components, either decreasing it due to W erosion or increasing it due to deposition. In particular, the deposition can create layers where different elements (W, C, O) are mixed [76], and it has been recently demonstrated that W optical properties such as emissivity strongly varies depending on the deposition area, so based on the physical-chemical properties of the deposit [77]. The presence of similar surface modifications is indeed known to affect W optical properties, due both to a local change of the electronic properties of the implanted area, and to an increase of the surface roughness. Many studies have been conducted on the separate dependence of W optical properties from temperature [78, 79, 80], as wells as from surface roughness [81, 82, 83, 84]. It is therefore of fundamental importance to evidence possible changes in W reflectivity due to both effects, and to understand their physical nature upon interaction with charged particles, in the expected working temperatures of ITER (<1273 K) [85]. During such interaction, the optical response can be simultaneously affected by the two effects (evolution of morphological or electronic properties), and only experimental parametric constraints can allow to study separately the two processes. For this reason, we study the effect of the evolution of morphology on W reflectivity by modifying the surface roughness of W samples. Optical reflectivity measurements are performed on such W samples

with controlled roughness. Furthermore, we study the combined effect of roughness and temperature on W reflectivity using a "pump-probe" laser system, which locally probes the optical response while the sample is heated by a high-power laser.

The results of this work are resumed in [50] and, as already explained in the Introduction, can be seen as a preliminary study for the experiments realized in the following chapters of this thesis.

3.1 Experimental procedure and effect of annealing on roughness

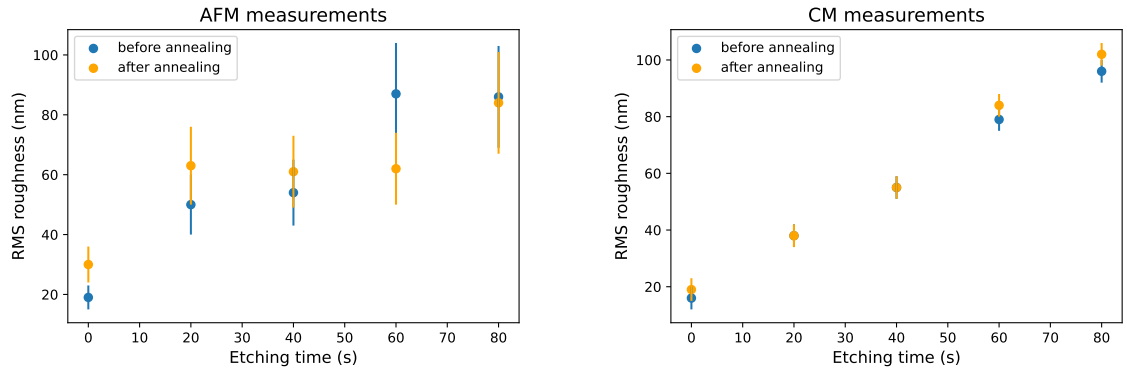
Five W samples provided by GoodFellow (99.95wt% purity, 10x10x0.5 mm^3) are mechanically polished in order to have a mirror-like surface. The roughness of each sample is controlled by chemical etching using Murakami's solution (a mixture of 10wt.% KOH in H_2O and 10wt.% $K_3Fe(CN)_6$ in H_2O), a method which, as proven by previous studies ([86]), allows to induce a given roughness in the material without causing any mechanical damage. One of the five samples is left unetched and used as a reference (W1); the remaining four are etched during different times: 20, 40, 60 and 80 s (respectively, W2, W3, W4 and W5). After chemical etching, each sample is cleaned in an ultra-sonic bath with acetone and then ethanol.

The experimental set-up used to perform reflectivity measurements is the one described in 2.1.3. We make reflectivity measurements in s and p polarization while heating the backside of the samples with the HPL from room temperature to 1073 K. We measure the surface temperature of the front face with a pyrometer. Each sample is heated using the following procedure: during a first temperature cycle, we hold the sample for 5 minutes at 6 different temperatures (300, 473, 623, 723, 823, 923 K) and we measure reflectivity at each temperature, for both light polarizations. The sample is then annealed at 1073 K for 30 minutes. Reflectivity is measured both at 1073 K and at room temperature after the annealing, waiting a sufficient amount of time for the sample to cool down. Two more identical annealing cycles are then performed on the sample, to study the evolution and stability of its optical response. The purpose of the three annealing cycles is to follow the change of reflectivity due to the temperature increase and the surface roughness/composition evolution. It is known from previous studies [87], in fact, that thermal annealing of metals can be responsible for an evolution of their surface roughness, as it induces stress liberation and structural improvement.

Before and after reflectivity measurements and annealing, we measure the root mean square roughness σ of each sample with two techniques described in 2.1.5, AFM and Confocal Microscopy (CM). The plots in figure 3.1 represent the RMS roughness σ values of the five samples as a function of etching time, before and after the annealing, extracted with AFM (a) and CM (b). The size of AFM images was of 40x40 μm^2 while the size of CM images was 0.98x0.76 mm^2. We can notice that, as an expected effect of chemical etching, σ increases with etching time as:

$$\sigma = 20.8 + 0.93 \cdot t_{etching} \tag{3.1}$$

Equation 3.1 is obtained from a linear fit of experimental data, averaging the RMS roughness values obtained by the two techniques. The error on the roughness values



(a) (b)

Figure 3.1: RMS roughness AFM (a) and CM (b) measurements as a function of samples etching time, before and after the annealing.

obtained by CM correspond to the experimental resolution of the technique at the specific magnification of the microscope (4 nm for the 50x objective). The error on the roughness values obtained by AFM is taken as the 20% of the values, based on the size of our AFM tip for the standard ISO 19606:207 and due to the local nature of the technique, as it is unlikely to return in the same area in the same sample [88].

If we look at RMS roughness after the annealing procedure, we notice that the values measured by AFM do not follow a precise trend, apparently tending to homogenize, increasing for samples with low-medium initial roughness (W1, W2, W3) and decreasing for samples with higher initial roughness (W4, W5). CM results, on the other hand, do not show relevant variations after the heating. This is likely due to the discrepancy between the two techniques, AFM measurement being very local and thus representative only of the specific scanned area. In our analysis, we realized AFM going always at the center of each sample before and after the annealing, but, as specified above, due to the very small scale of the technique, it is quite difficult to go back at the same area. Figure 3.2 shows the AFM images of three samples (W1, W3 and W5) before (left column) and after (right column) the annealing. After the annealing, we do not notice any change in the surface morphology for all the samples, in contrast with some studies mentioned before such as [87], possibly due to the different examined material and other discrepancies (annealing and vacuum conditions, explored temperature range, surface preparation). The bright protuberances present in figures 3.2 (d) and (f) are probably connected to the quality and cut of the material (laminated W), rather than a direct effect of the annealing, as similar structures have been observed in W samples provided by the same company and with a similar surface preparation.

3.2 Reflectivity variation with roughness and temperature: results and model discussion

In figure 3.3, we present the reflectivity of the five sample before (green solid curves) and after (blue solid curves) the first laser annealing, in both cases recorded at room temperature. As expected, reflectivity decreases as roughness increases, going from

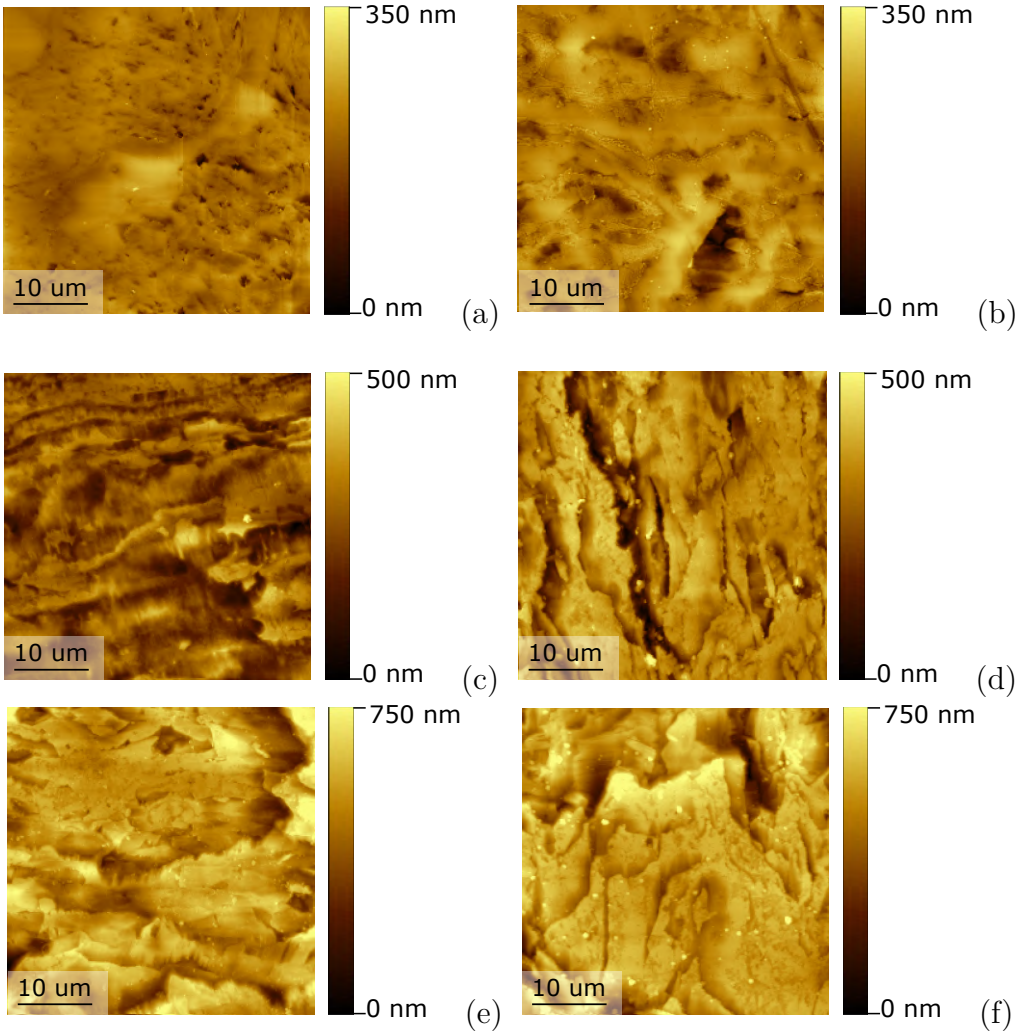


Figure 3.2: AFM images of samples W1 (a, b), W3 (c, d) and W5 (e, f), before (left) and after (right) annealing.

35% at 840 nm for the first reference sample (W1, with σ=19±4 nm) to 5% for the last, most rough sample (W5, with σ=102±4 nm). The experimental reflectivity spectra are then compared with the theoretical values of reflectivity (dashed green and blue lines in figure 3.3), obtained using the equation 2.25 derived from Bennet-Porteus model described in section 2.2.3. In the model, we use as σ the experimental RMS roughness values extracted from CM images, before and after laser annealing. We choose to consider CM roughness values as they are more representative of the area to which we are optically sensitive (closer to the 2 mm diameter of the laser beam). As $R_0(\lambda)$ we use the reflectivity spectrum of the reference sample W1. All the reflectivity curves are related to unpolarized light (obtained by making an average of s and p spectra).

The theoretical curves are in quite good quantitative agreement with experimental results. It can be observed that the theoretical curves of W3–W5 samples present spectral behavior slightly different from the experimental ones. A possible reason could be that the used model is valid only in the case that surface irregularities are much smaller

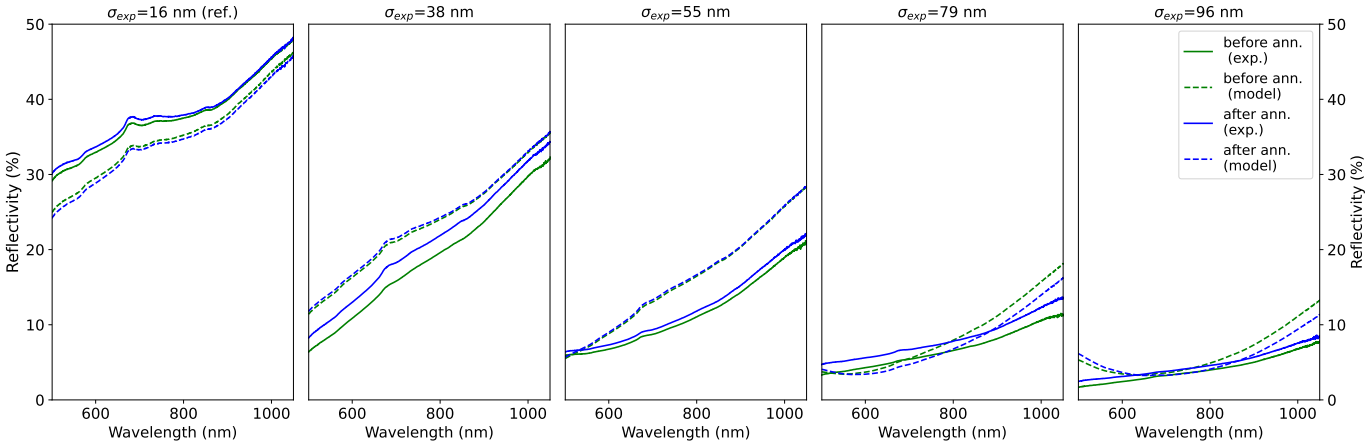


Figure 3.3: Experimental reflectivity spectra measured at room temperature (solid lines) for unpolarized light before (green) and after laser annealing (blue), and theoretical curves (dashed lines) obtained with equation 2.25.

compared to the used wavelength $\sigma << \lambda$ [67]. If this is not the case, in fact, already when σ is of the same order of λ, diffraction effects become important and the reflectivity will depend also on the size and inclination of surface irregularities. As visible in figure 3.4, when the roughness of the samples increases (going from W1 to W5), the weight of the diffused reflectivity (second term in equation 2.25) similarly increases, contributing for 100% of the total reflectivity for sample W5 at shorter wavelengths. In this case, a more accurate experimental set-up, able to measure also the diffused component of reflectivity, as well as more accurate scattering models, considering the bidirectional reflection distribution function (BRDF) and, thus, overcoming the previous limitation, could provide a more accurate agreement between theoretical and experimental results [89], as shown in the study [90] in the case of beryllium samples.

Going back at figure 3.3, one can note that an irreversible change of reflectivity is observed after the first annealing for all samples, in the whole spectral range. Quantitatively, the irreversible relative increase of reflectivity at λ=840 nm measured at room temperature goes from 5% for the reference sample W1 to 10% for the second rough sample W2, which experienced the largest reflectivity change after the first annealing. However, we do not observe an irreversible evolution of reflectivity at room temperature after the second and third annealing. In other words, the reflectivity at room temperature stabilizes and does not evolve anymore after the second and third annealing.

Figure 3.5 shows the relative reflectivity variation (with respect to room temperature) at λ=840 nm, as a function of the sample temperature. Each point is averaged over the five samples, since they all show a similar behaviour. The black squares represent the reflectivity relative variations during the first annealing, which range from 6% at 473 K to 15% at the highest annealing temperature (1073 K). During the second and third annealing, we observe an identical relative variation, smaller compared to the first one (the largest variation being around 6% at 1073 K). The other wavelengths show a similar trend but smaller in absolute value, as visible in figure 3.6 (with a maximum relative variation of 12% at 600 nm and 10% at 1000 nm). Thus, the important reflectivity variation variation observed during the first

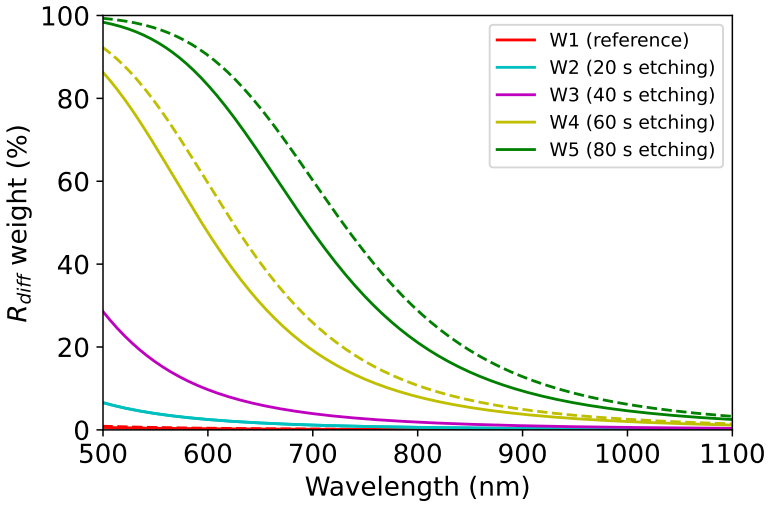


Figure 3.4: Percent weight of the diffused component on the total reflectivity (obtained from Bennet-Porteus model) as a function of wavelength, for the 5 samples, before (solid curves) and after (dashed curves) the annealing. For W2 and W3, solid and dashed curves overlap, as their roughness is unchanged after the annealing.

annealing results from two different physical processes: the first one is related to W electronic properties and is reversible (such as in the second and third annealing); the second one, which is irreversible and is more related to the surface morphology and composition.

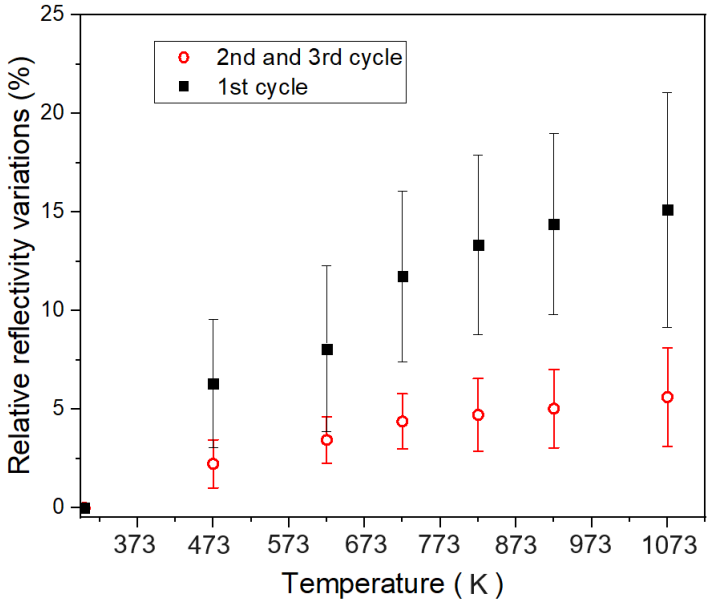
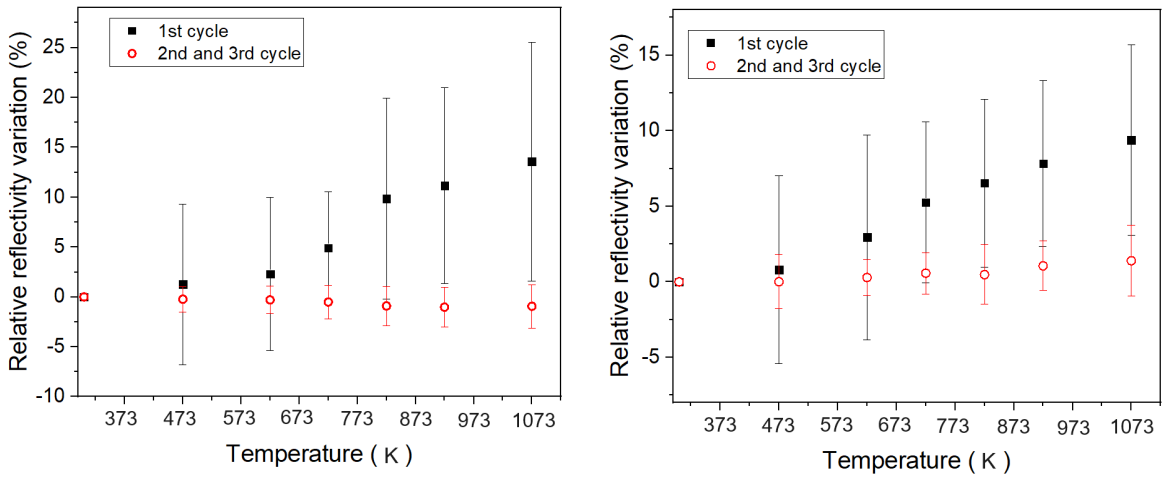


Figure 3.5: Relative reflectivity variation (with respect to the RT curve) at 840 nm as a function of temperature, during the first annealing (black squares) and the second and third ones (averaged, open red circles). Each point was obtained by averaging over the five samples, the error bar being the standard deviation.



(a) (b)

Figure 3.6: Relative reflectivity variation (with respect to room temperature measurement) at 600 nm (a) and 1000 nm (b) as a function of the samples temperature, during first annealing (black squares) and during second and third annealing (averaged, open red circles).

Two main hypotheses are then considered to explain the variation during the first laser annealing: an evolution of the roughness or of the surface composition. If one considers only roughness effects on reflectivity, an increase in roughness for a specific sample should correspond to a lower reflectivity spectrum, and vice versa. But as surface roughness does not evolve significantly in the studied temperature range (as evidenced by the morphology analysis), it cannot explain the irreversible reflectivity after the first annealing.

3.3 Chemical analysis: influence of surface composition on reflectivity

To test the second hypothesis (evolution of surface composition during first annealing), we analyze the elemental composition of W samples with XPS, before and after the laser annealing. The different chemical elements are assigned using the NIST-XPS database and references therein [91]. The XPS measurements were qualitatively the same for all the samples, hence we here show only the ones realized on W5.

The core levels of the observed elements are shown in figure 3.7 as a function of their binding energy, for the sample W5: (a) W 4f, (b) C 1s and K 2p, (c) N 1s, (d) O 1s. As visible in figure (a,d), the amount of native tungsten oxide (WO_3), visible from the "oxidized W" peaks at 37.7 and 35.5 eV, is drastically reduced after laser annealing, while the "metallic" W peaks, at 33.3 and 31.1, increase. WO_3 is a semiconductor with a band-gap of 2.9 eV [92] absorbing for λ>400 nm [93]. This would suggest that the increase of reflectivity in the visible and near-infrared domain is more likely related to the reduction of the native oxide film, in agreement with Addab et al. [48], who studied the role of oxide layer thickness in decreasing the surface reflectivity in the wavelength range 2.5-5.5 µm. Moreover, as presented in figure (b,c),

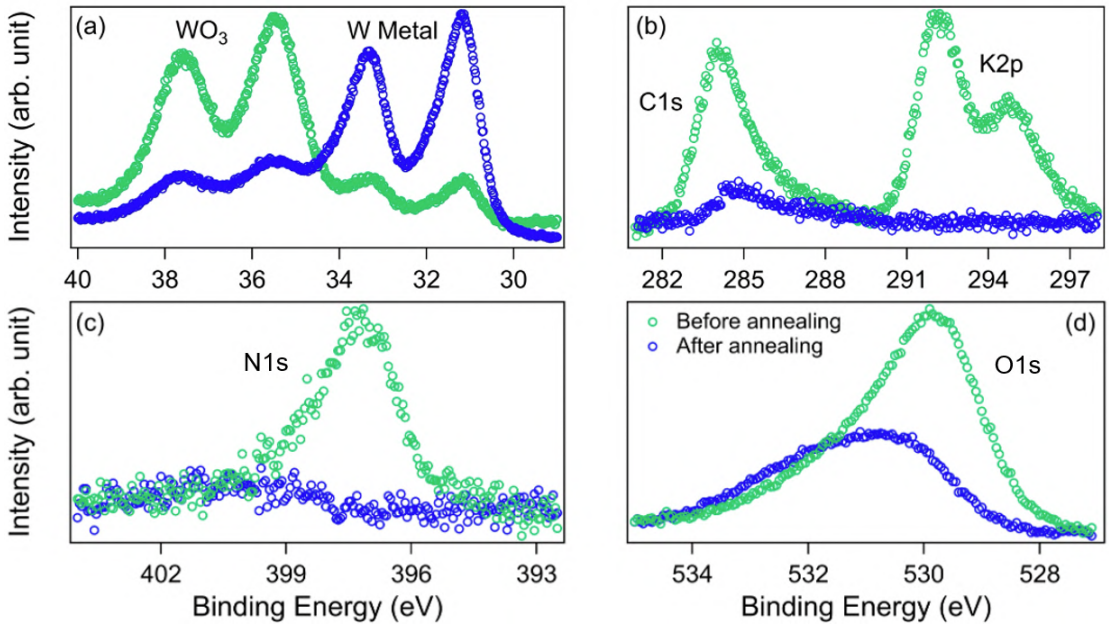


Figure 3.7: XPS spectra of sample W5 as a function of binding energy, showing the core levels of W 4f (a), C 1s and K 2p (b), N 1s (c), and O 1s (d) before (green open circles) and after annealing (blue squares).

carbon, nitrogen and potassium (residuals of the chemical etching solution) are still present after ultrasound bath cleaning for the four etched samples before the annealing (green curves), and could produce additional absorption. The laser annealing would then allow the desorption of such species. Thus, the reflectivity variation observed for all samples after the first annealing is likely due to two different contributions: the evolution of the native oxide and the desorption of the chemical etching solution residuals. Since in the reference sample W1 we do not detect any presence of potassium or nitrogen, but only an evolution of the native oxide (as observed by Pardanaud et al. [94]), the irreversible increase of reflectivity after the annealing could be attributed mainly to the evolution of the surface oxide. We stress that oxygen and carbon are systematically detected on all W samples, while the presence of potassium and nitrogen is clearly related to the used etching procedure.

3.4 Conclusions and perspectives

In this study, we aim to gain insight on the evolution of optical properties of W in harsh environments where high photon and particle fluxes, heat loads, and impurities can change both the morphology and surface composition of W. These findings can be of particular interest, among all, to fusion technologies and tokamak reactors. We use chemical etching to control the surface roughness of W samples in the 20–100 nm range in order to simulate the damage induced by the interaction with He ions, with the aim to study the role of morphology and composition on the optical response of W. As expected, the measured reflectivity decreases as the surface roughness increases. A simple scattering model allows to quantitatively predict the experimental findings and the evolution of reflectivity as a function of the surface roughness. The discrepancy

of the model with experimental data as the roughness of the samples becomes bigger can be explained with the predominance of the diffused component of reflectivity on the specular one, which would be overcome by using different models which take into account also the angular distribution and shape of surface irregularities. Moreover, we follow the evolution of both the optical response and the surface morphology during laser annealing in the 300-1073 K temperature range. We observe that, during and after the annealing, reflectivity tends to increase for all samples. Using AFM and CM techniques, we highlight that evolution of RMS roughness is unlikely to be the origin of the measured reflectivity variation, since roughness values did not sensibly vary in the investigated temperature range. We demonstrate that the increase in reflectivity is rather due to a change in the chemical composition of the samples, performing a composition analysis (XPS) before and after the annealing. We observe that the heating causes the desorption of nitrogen and potassium impurities (residuals of the etching solution) and reduces the amount of the native oxide, and we conclude that this last effect is more likely to cause an increase in the specular reflection. By highlighting the role played by morphology, surface impurities and native oxide, we attempt to quantitatively estimate the variation of reflectivity both as a function of roughness and as a function of surface composition, as a first, preliminary study before introducing the effect of actual interaction of ions (D and He). In such more realistic contexts, in fact, the optical response of W will be modified by the simultaneous and combined effects of ion interaction, temperature increase and change in morphology and/or chemical composition (caused by both the heat loads and the ion fluxes). We will analyze these scenarios in the following chapters, focusing first on the interaction with D ions (where roughness variation can be neglected) in chapter 4, and then on the interaction with He ions, where the roughness variation influences considerably the optical response of W, in chapter 6.

Chapter 4

Study on temperature and D retention effect in W reflectivity variation during D plasma

This chapter describes the results of *in-situ* spectroscopic ellipsometry measurements performed on W exposed to low energy D plasma. The aim of such experiments is to acquire a deeper knowledge on the behaviour of W optical properties under conditions that resemble the ones of the divertor in a tokamak environment. In such context, W plasma-facing components (PFCs) will handle high heat fluxes, up to 10 MW/m^2 in steady state and 20 MW/m^2 in slow transient [95], and high fluxes of particles ($\simeq 10^{24} m^{-2} s^{-1}$) with an energy <100 eV. Most of the existing operating tokamaks are currently validating the PFCs protection strategy with the use of visible and IR thermography [96]. Therefore, it is necessary to have the most accurate temperature measurements of W PFCs, for both machine safety reasons and research studies. In this work, we measure W optical properties in the wavelength range 400-1000 nm, in particular the refractive index $n(\lambda)$ and the extintion coefficient $k(\lambda)$, from which it is possible to calculate the reflectivity $R(\lambda)$, which is then directly linked to emissivity $\epsilon(\lambda)$ by the relation $\epsilon(\lambda) = 1 - R(\lambda)$. It is important to specify that this wavelength range does not correspond exactly to the one used in optical diagnostics in tokamaks. The choice of this domain is rather dictated by the available commercial instruments and it could be considered as a proof of concept. Surface emissivity strongly depends on wavelength, temperature and surface state (roughness, cracks, oxidation), as well as the manufacturing process (which, for the same wavelength and temperature, can cause a variation up to one order of magnitude) [41]. We use *in-situ* spectroscopic ellipsometry as a tool to measure the modification of W optical response in real time during plasma exposure. Such technique, in fact, is a non-contact optical diagnostics and is therefore suitable to measure with high accuracy the optical properties of materials even under extreme conditions (high vacuum environment, high temperatures and high ion fluxes), in a fast and non-destructive way. It has already been extensively used to measure the optical constants of various metals [97, 98, 99], among which W, as well as semiconductors and dielectric materials [100, 101, 102], in a different variety of conditions [103]. Thanks to its high sensitivity, it is a suitable technique to monitor surface processes such as thin film growth, microscopic surface roughness [104], multi-layer and graded-composition systems [105], and etching for example by a

plasma [106, 98]. Moreover, some investigations have been conducted during the last years in order to possibly integrate an *in-situ*, real-time ellipsometer in the first wall of a tokamak [107].

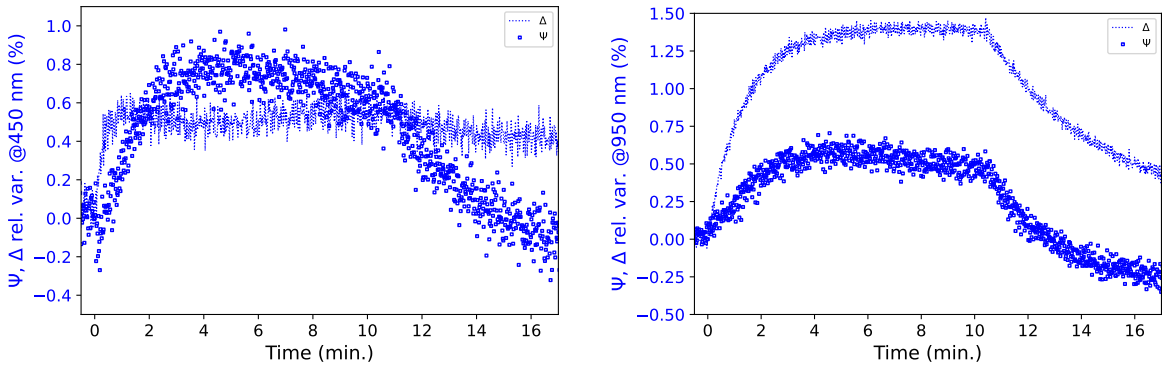
In the present chapter, we perform measurements during D plasma exposure and try to separate and estimate quantitatively the effects of temperature and ion interaction in the variation of W reflectivity, using calibrations realized to measure only the effect of temperature. We try to validate the contribution of D ions interaction using the code MHIMS (Migration of Hydrogen Isotopes in MaterialS), which can model the diffusion and trapping of hydrogen isotopes in W, and allows to estimate their depth profile and overall retention [108]. Finally, we find that the values of concentration of D atoms in the first 25 nm (depth to which the ellipsometry light penetrates "at the first order", i.e. reducing its intensity by 1/e of the initial value) during the plasma exposure time matches quite well and could explain the behaviour of D ions contribution to reflectivity variation.

4.1 In-situ modification of W optical response during D plasma

Ellipsometric measurements are realized on a W sample provided by GoodFellow (99.95% purity, 10x10x0.5 mm^3) and mechanically polished in PIIM, introduced in CAMITER vacuum chamber via the load-lock system. Before the sample is introduced in the chamber, a first "conditioning" D plasma is realized for about an hour in order to make impurities desorb from the walls. Once the sample is installed on the sample holder, it is moved along the z-axis to the lowest reachable point and the walls of the chamber are again conditioned with a D plasma for about an half an hour, in order to prepare the set-up and to put the chamber walls in a steady-state condition for the experiment. After walls conditioning, we align the ellipsometer light beam at approximately the center of the sample and try to maximize the yield of the intensity signal recorded by the detector. The spot of the pyrometer is also positioned at the center of the sample. The sample is then exposed to D plasma with an ion flux of 1.7×10^{20} $m^{-2}s^{-1}$, obtained using a gas pressure of 2 Pa and RF power of 600 W. The exposure time is 10 minutes, corresponding to an ion fluence of 1×10^{23} m^{-2}. The ion energy is around 12 eV, since the sample-holder is not biased ("floating").

Here, we represent the percentage relative variation of Ψ and Δ with respect to their value at t=0, when the plasma starts. Most of the wavelengths show the same qualitative behaviour during plasma exposure, namely an increase of the signal as soon as the plasma is on, with a following stabilization and then decreasing once the plasma is off, at t=10 min, with a slower trend with respect to the initial phase when plasma is on. We show in figure 4.1 Ψ and Δ as a function of time during a D plasma exposure of 10 minutes, for the wavelengths λ=450 nm (a) and λ=950 nm (b), and in figure 4.2 for λ=850 nm. We choose to focus on the latter one as it shows the biggest variation of Ψ and Δ in absolute value.

Looking more in detail at the left scale in figure 4.2, we observe a sudden rise in the ellipsometric signal (both Ψ and Δ) as soon as the plasma is on. After about 4 minutes, the signal stabilizes into a plateau region (with a slight decrease of Ψ signal around about 8 minutes). When the plasma is switched off (at t=10 min.), the signal



(a) (b)

Figure 4.1: Ψ and Δ relative variation at 450 nm (a) and 950 nm (b) as a function of time. The plasma starts at t=0 min. and stops at t=10 min.

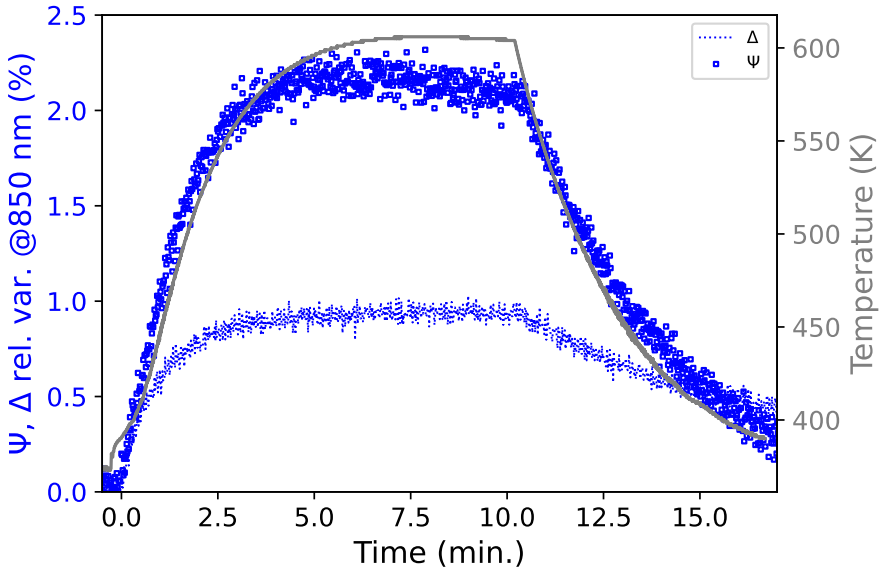


Figure 4.2: Ψ and Δ relative variation at 850 nm (blue curves, left scale) and simultaneous W surface temperature (black curve, right scale) as a function of time.

decays exponentially, and Ψ and Δ return to their initial value, even if with different time constants. For most of the other wavelengths, both Ψ and Δ curves do not go back to their initial value, at least in the measured time range (figure 4.1). It is difficult to speculate on the physical meaning of Ψ and Δ signals without making any model, however a possible reason could be a different response of each wavelength to the combined effect of plasma exposure and temperature rise, without necessarily going back to the initial value. However, it is important to notice that, for most of the wavelengths, Ψ and Δ percentage variations are even smaller than the ones at 850 nm, possibly resulting in negligible variations of the extracted reflectivity. On the right scale, we show in figure 4.2 the behaviour of the temperature signal, simultaneously recorded by the pyrometer (grey curve). It is clear that the temperature signal follows the same trend of the optical one, meaning that the surface temperature of the W

sample rapidly rises because of the plasma, reaching a plateau region at around 600 K, and exponentially drops back to room temperature as soon as the plasma is off. We stress that all our experiments are realized at room temperature, meaning that the temperature increases because of plasma and we do not heat or cool down the system before making the plasma.

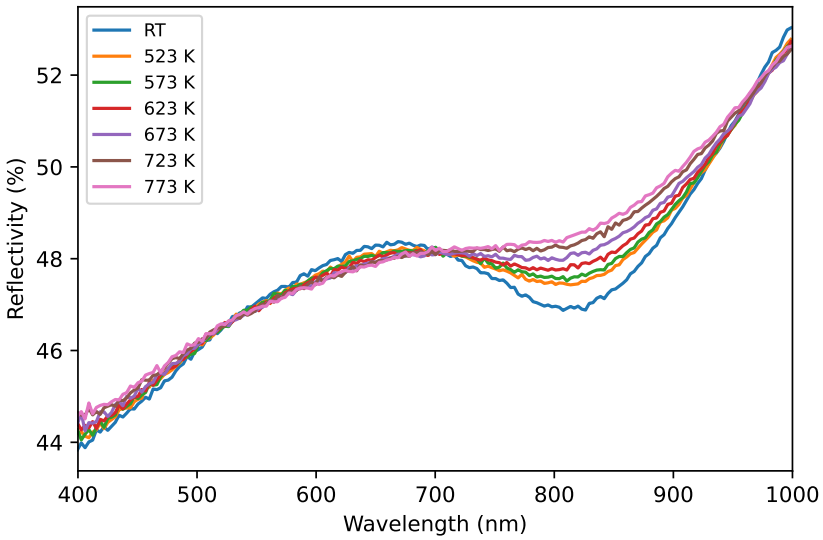


Figure 4.3: W reflectivity spectra calculated from ellipsometric measurements during oven annealing, for 9 temperatures in the range 300 K (RT)-773 K.

Moreover, as it was already shown by previous studies [80] and confirmed in chapter 3 of this thesis, in correspondence of the wavelength λ=850 nm, W optical properties such as reflectivity are most affected by the temperature variation in the range 300-1000 K. In particular, reflectivity increases with temperature, becoming more flattened with temperature, with the disappearance of the well at 820 nm typical of the room temperature spectrum. This can be explained using a Lorentz-Drude model for W dielectric function, if one includes the temperature dependence not only of the Drude terms (free electrons, taking into account the intraband transitions) but also of the Lorentz ones (bound electrons, taking into accountthe interband transitions) [80]. We will go deeper on this subject later in this chapter, as it will be used to explain our results.

We calculate W reflectivity in the sample temperature range 300-800 K from our ellipsometric experimental set-up, using the oven of CAMITER plasma chamber (section 2.1.4) to anneal the sample. The trend of the spectra (figure 4.3) is found to be in qualitative agreement with the results of [80], which measured solely the effect of temperature onto W reflectivity, with a relative variation of reflectivity (with respect to room temperature value) of 4% at 850 nm for the highest temperature (773 K). The goal at this point is to evaluate how much the ellipsometric signal is affected by the temperature rise and how much by the interaction with D ions coming from the plasma. First of all, we perform a series of calibrations of our system in order to exclude the presence of artefacts or systematic errors in the experiments, compromising the reliability of the ellipsometric measurements.

4.2 Evaluation of the effect of the plasma on ellipsometric measurements

We make a first test in order to verify if the signal recorded by the pyrometer is due to an actual variation of the sample surface temperature, or to a possible absorption or emission of radiation emitted by the plasma in the working wavelength range of the pyrometer (2-2.6 µm). For this reason, we put an oven (black body) in front of one of the chamber viewports, and we align it to the pyrometer. We set the oven to reach a fixed temperature and wait for it to stabilize, until the pyrometer can read the same value, and switch on the plasma. The temperature value detected by the pyrometer stays the same, meaning that it is not influenced by any absorption or emission process of the plasma radiation. The same test is realized for three different temperatures (523, 623 and 773 K) and also in the reversed way (switching on the plasma before, then changing the temperature and waiting for it to stabilize), always obtaining the same result. This result confirms that the plasma does not influence the temperature measurement by pyrometer.

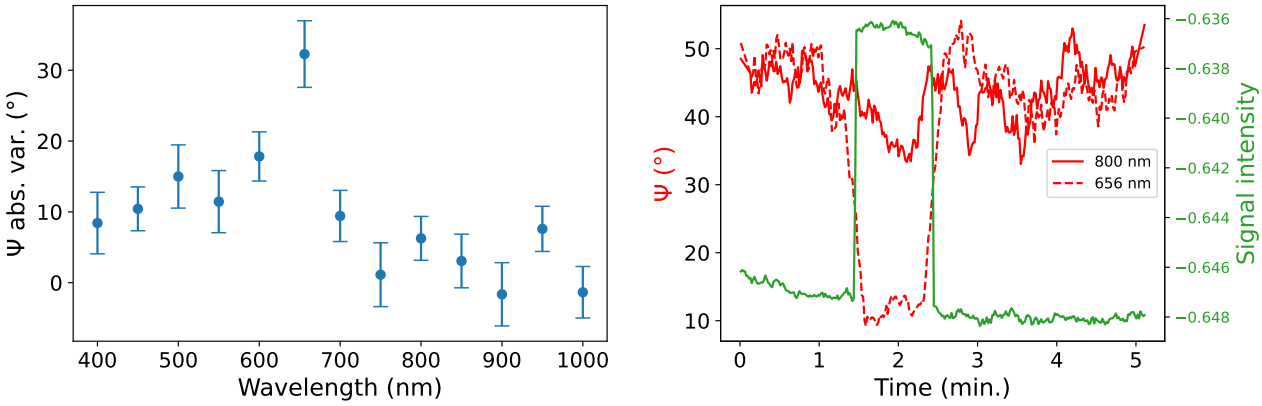


Figure 4.4: Absolute variation of Ψ caused by D plasma during "dark" measurement, as a function of wavelength (a) and as a function of time for two wavelengths (b), together with the temporal evolution of the signal intensity (integrated over the whole wavelength range). The plasma takes place between t=1.5 min. and t=2.5 min.

Another test is realized in order to verify a possible contribution of the light emitted by the plasma in the variation of Ψ and Δ. For this purpose, we reproduce what in optical experiments is known as a measurement of the dark: we cover the ellipsometric light source and switch on the plasma, in order to detect a variation of the signal that is due to the plasma only. We observe that, in correspondence of plasma, the intensity of the light collected by the detector (averaged over the whole wavelength range) increases by 1.85% (figure 4.4(b)). If we look at the variation of Ψ caused by the presence of the plasma (figure 4.4(a)), we can see that for most of the wavelengths it is comparable to the error bar (noise level), except for the wavelength λ=656.2±3 nm, for which this variation is more consistent. We can conclude then that Ψ is affected by the presence of the plasma only at this wavelength (figure 4.4(b)), which is the one of D Balmer-α emission. For the same wavelength, Δ is not affected by the plasma emission, possibly because the D emission line does not induce a phase variation.

4.3 Effect of temperature and ion interaction in W reflectivity variation

After the control experiments in section 4.2, the next step of our study is to estimate how much of W surface modification evidenced by the variation of the ellipsometric signal in figure 4.2 is actually due to the physical-chemical interaction between D ions and W. Since this effect is combined to the temperature rise occurring during the plasma, it is necessary to separate the two.

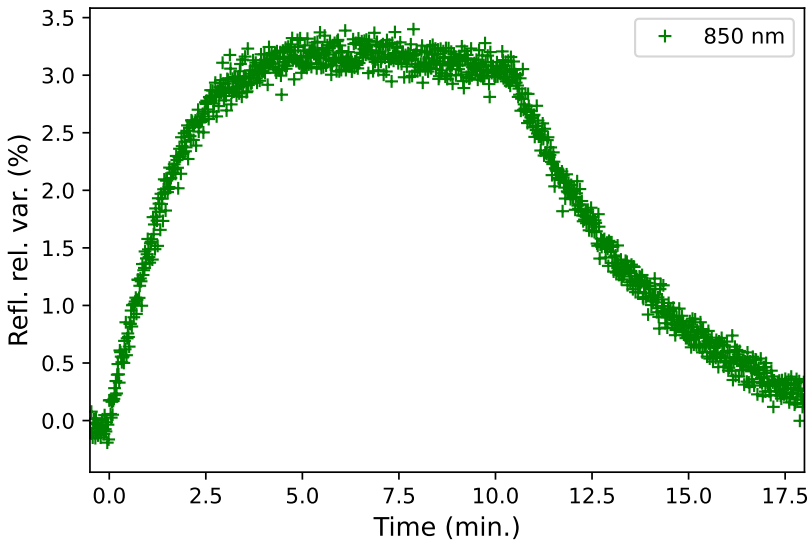


Figure 4.5: W reflectivity relative variation at 850 nm (with respect to the initial value, before plasma) as a function of time.

We can obtain the optical constants n and k of W directly from the measured Ψ and Δ. These are often called pseudo-optical constants and they are valid for bulk materials, where no surface roughness or overlayers are taken into considerations (more details are present in section 2.2.1 of chapter 2). From those, we can calculate the reflectivity and represent it as a function of time. Figure 4.5 represents the reflectivity relative variation at 850 nm (with respect to the initial value, before plasma) experienced by the surface during plasma exposure. It is possible to see that the maximum variation at this wavelength is of about 3.3% (corresponding to the temperature plateau T_{max}=600 K, reached around t=7.5 min.).

In order to calibrate the temperature-only dependence of the optical signal increase, we perform *in-situ* ellipsometry while heating the sample up to 600 K, without exposing the sample to D plasma. This will be referred to as the "annealing" measurement. The first annealing measurement was realized using the oven installed underneath the sample holder in the plasma chamber (more details in section 2.1.4). The temperature regulation of this oven is controlled by a PID system. The temperature ramp is slow (about 10 times longer than the actual temperature increase observed during plasma exposure) and quite hard to control with the PID. As visible in figure 4.6(b), the ramp is not linear and creates artefacts in the representation of the optical signal (reflectivity variation) as a function of temperature, where a jump appears (4.6(a)), which is not

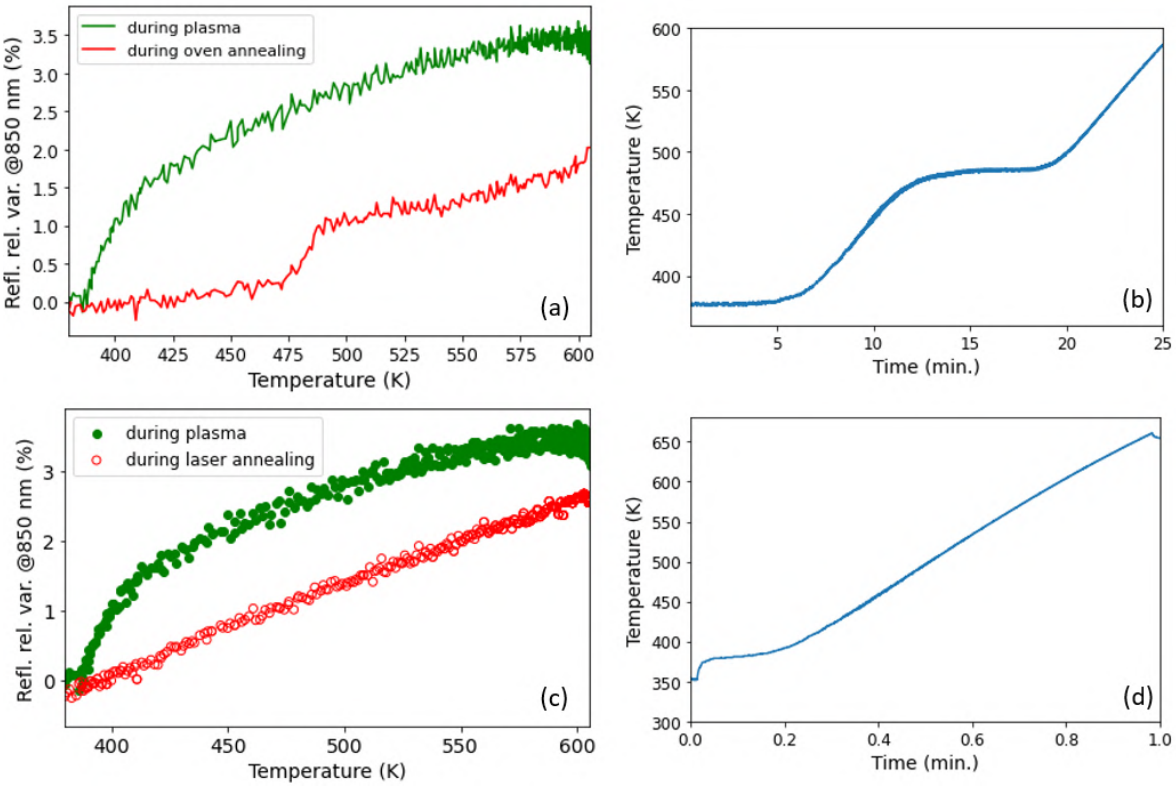


Figure 4.6: Comparison of reflectivity relative variation at 850 nm as a function of temperature (during plasma exposure and during annealing) and correspondent temperature ramps, respectively for the oven annealing (a,c) and for the laser annealing (b,d).

directly related to any physical change or phenomenon modifying the surface. This is why we thought of an alternative way to perform the annealing measurement, namely through an high power laser (the same used in the experimental set-up described in section 2.1.3). In this case, the temperature ramp is much faster, i.e. on the same timescale than the one during plasma exposure, and linear (figure 4.6(d)).

The same quantities that we have represented as a function of time can be also shown in a different way. Since the temperature ramp during the annealing measurement is different from the one we have during plasma exposure, we represent reflectivity variation as a function of temperature for both cases (plasma exposure and annealing measurement), eliminating therefore the temporal dependence. In figure 4.7, the green curve representing reflectivity relative variation at 850 nm refers to the plasma exposure measurement, which can be distinguished into two phases, one (green full dots) corresponding to the plasma exposure, with a temperature rise up until 600 K, the other one (green empty dots) corresponding to phase when the plasma is switched off and the system cools down. The reflectivity relative variation at 850 nm recorded during annealing (red curve in figure 4.7) is an average of the heating ramp and the cooling phase of the laser annealing process. First of all, it is possible to see from the green curve that the heating and cooling phases of the plasma exposure measurement do not follow the same path, suggesting an hysteretic behaviour, in stark contrast to the annealing heating/cooling phases which well overlap (not shown here). We therefore subtract point to point the curve relative to the annealing measurement (red dots)

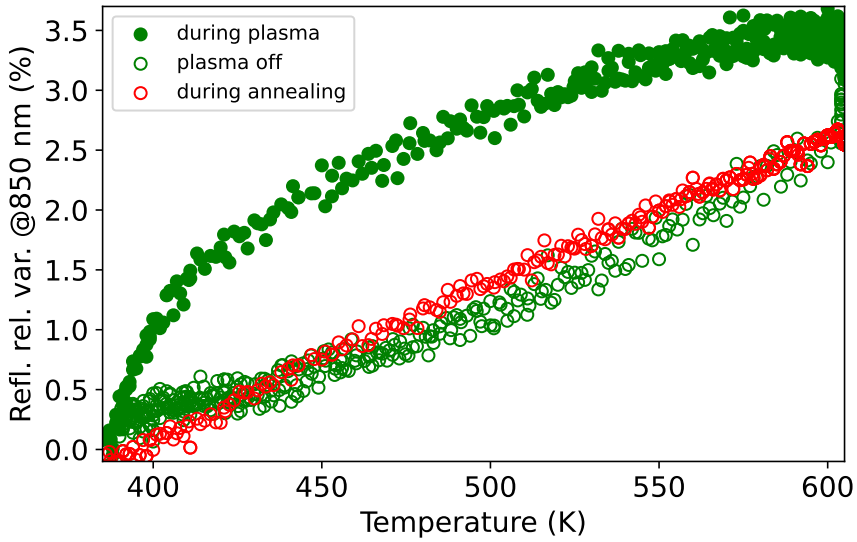


Figure 4.7: Reflectivity relative variation at 850 nm as a function of temperature, during plasma exposure (green full dots), during the cooling phase as the plasma is off (green empty dots) and during laser annealing and cooling phase, averaged (red empty dots).

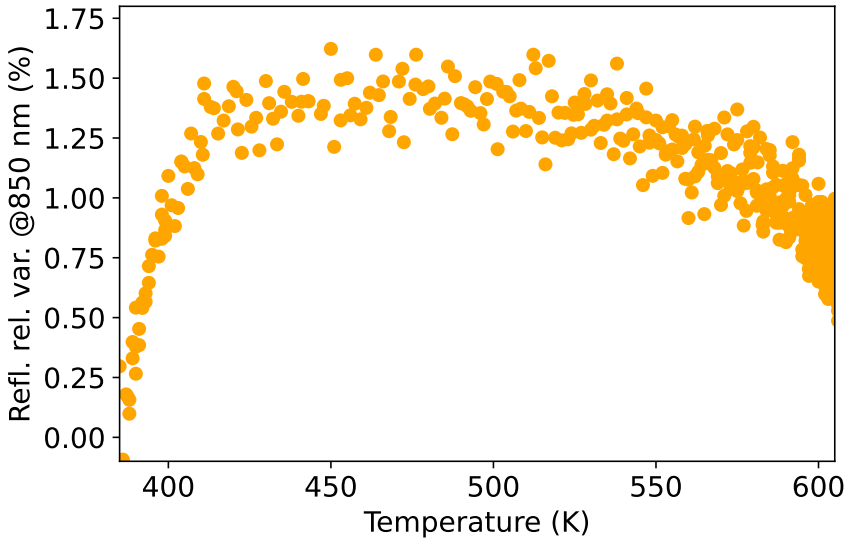


Figure 4.8: Reflectivity relative variation at 850 nm as a function of temperature due to the interaction with D ions, calculated as the subtraction of annealing measurement (red curve of figure 4.7) from the plasma measurement (green curve of figure 4.7).

from the one relative to the plasma exposure (green full dots), assuming that the result of this subtraction is the contribution of D ions only to the modification of W optical properties. The result of this subtraction is represented in figure 4.8, where we plot the reflectivity relative variation at 850 nm due to D/W interaction. From this representation, we can see that this variation reaches the maximum value (around 1.5%) at around 410 K, slowly decreasing afterwards. This would suggest a more important contribution of D/W interaction in the phase in which temperature is rising during the plasma, which would then decrease as soon as the thermal equilibrium is reached.

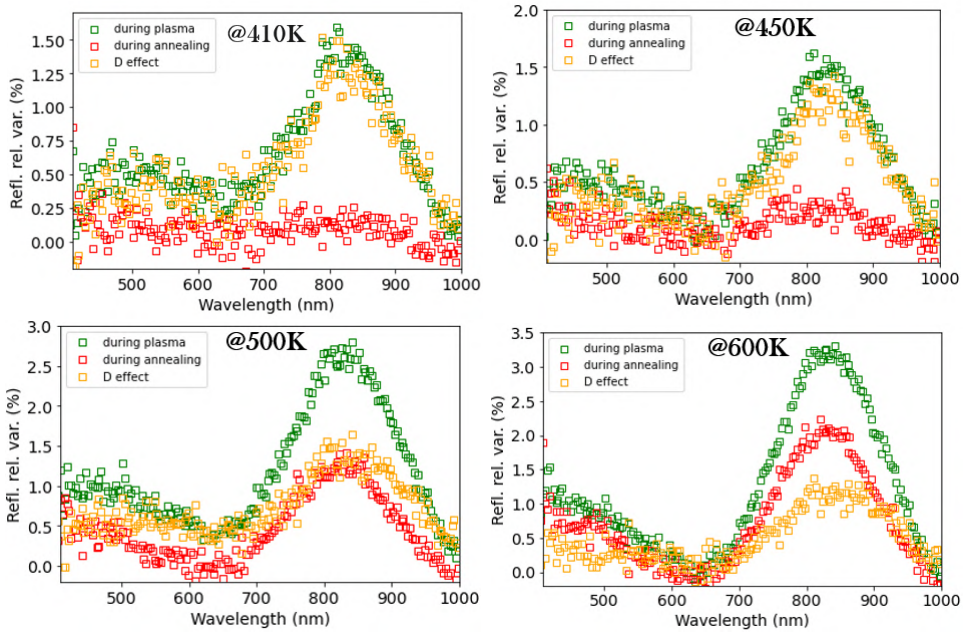


Figure 4.9: Reflectivity relative variation (with respect to the initial value, without plasma and at room temperature) as a function of wavelength, during plasma exposure (green curve), during annealing (red curve) and caused by interactions with D ions (orange curve, derived from a subtraction of the red curve from the green one), for four moments of the plasma implantation, respectively at 410 K, 450 K, 500 K and 600 K.

Figure 4.9 represents the spectral variation of reflectivity with respect to the initial value, taken before plasma for the green curve and before the annealing for the red curve (both at room temperature). In the case of plasma exposure, we calculate the variation of reflectivity in correspondence of different moments of the plasma implantation phase, namely when the temperature is 410 K, 450 K, 500 K and 600 K. In the case of annealing, we calculate the variation of the reflectivity spectrum at the same temperatures (410 K, 450 K, 500 K and 605 K) but without plasma, with respect to the one at room temperature. We then subtract point by point the annealing measurement (red curve) from the plasma one (green curve), in order to estimate the sole contribution of D/W interaction in W reflectivity variation (orange curve). The table 4.1 resumes the values of reflective relative variations at λ=850 nm during plasma, during annealing and due to D ions (coming from a subtraction of the previous two), for the four temperatures of the plasma implantation phase. We can then conclude that the orange curve, representing D ions effect to the reflectivity variation, contributes to almost the total (98%) of the reflectivity variation at 410 K, where it reaches its maximum value. As soon as the temperature rises, it then decreases to the 75% of the total at 450 K, then to the 53% at 500 K, and finally to the 37% at 600 K, when the plateau region is reached.

The fact that the D ions contribution to reflectivity variation has a similar trend as the temperature curve may suggest that the two processes have a similar nature. In absence of a theoretical support, e.g. from first principle calculations of the two processes coupling, we assume that the mathematical functions describing the temperature contribution and the D ions contribution are independent and simply adds up. We prefer

Reflectivity relative variation @850 nm	**T=410 K**	**T=450 K**	**T=500 K**	**T=600 K**
During plasma (%)	1.47	1.47	2.66	3.13
During annealing (%)	0.02 **(2%)**	0.37 **(25%)**	1.24 **(47%)**	1.96 **(63%)**
Due to D ions (%)	1.45 **(98%)**	1.1 **(75%)**	1.42 **(53%)**	1.17 **(37%)**

Table 4.1: Table resuming the reflectivity relative variation during plasma, during annealing and due to D ions, during four temperatures of the implantation phase (410, 450, 500 and 600 K), in percentage.

to continue with this approach as the hypothesis of more complex mathematical relations (multiplication/division, convolution) would require stronger theoretical support that we do not have for the moment. Hence, supposing that temperature and D effect are summing, the reflectivity change could be explained by a modification of W Lorentz-Drude dielectric function, where the electrons of the material are described as damped oscillators. Both processes probably concur in modifying the electron-phonon interaction in the material, in one case because of an increase in the phonon distribution (temperature effect), and in the other case because of a modification of electrons density due to the interaction with D ions coming from the plasma (D effect). The application of the Lorentz-Drude model, including a dependence from the ion-electron (D-W) interaction, will soon start as a continuation and validation of this work. In addition, in the meantime, we encourage theoreticians to investigate the mathematical relations between the two effects based on the total reflectivity variations presented here.

4.4 Estimation of D surface inventory with the code MHIMS

At this point, to validate our assumption that the temperature-induced modification of the W reflectivity can be supplemented by a D plasma contribution, we seek to estimate the amount of D atoms trapped inside the material. As soon as there is an incoming flux of D ions, there is a certain amount of D_2^+ and D_3^+species which will reach the W surface and dissociate in D atoms. Those D atoms can be adsorbed on the surface or be implanted into a specific range in the bulk W material, which depends on the energy of the impinging ions. In our experimental conditions, the implantation range of 12 eV D ions in W (simulated with SRIM) is expected to be <5 nm. On one hand, the implanted D atoms can diffuse deeper into the material through interstitial sites, while being slowed down in their bulk diffusion by trapping at vacancies and other types of lattice defects. On the other hand, implanted D atoms can diffuse towards the surface. Once two D atoms are adsorbed on the surface, they can meet and then recombine and leave the surface as D_2 molecules. The diffusion of D atoms in interstitial sites as well as the trapping of D atoms in W defects could change W electronic distribution and thus its optical response. At the same time, since the detrapping of D atoms is a temperature-driven processes, the temperature rise simultaneous to the D implantation causes desorption of trapped D atoms from the surface, until an equilibrium situation is reached (which would correspond to the plateau region of both optical and thermal signal), in which we have an equal number of D atoms implanting and desorbing from the surface. When the plasma is switched

off, D atoms implantation into W stops (as there is no more source of incoming ions) and the system cools down. However, a certain number of D atoms will stay trapped inside the material, causing an hysteresis of the optical signal, as seen for example in figure 4.7.

The code MHIMS, extensively described in [108], based on a rate equations model, allows to simulate the diffusion and trapping of hydrogen isotopes (HI) inside a material, given as input parameters the ion flux, the ion energy and the temperature ramp during the implantation phase. The model divides HI in W into mobile and trapped species, whose concentrations evolve in space and time. The evolution of these concentration is described by the following equations:

$$\frac{\partial c_m}{\partial t} = (1-r)\phi f(x) + \nu_{diff} \cdot \frac{\partial^2 c_m}{\partial x^2} - \frac{\partial c_t}{\partial t} \tag{4.1}$$

$$\frac{\partial c_t}{\partial t} = \nu_{trap} \cdot \frac{c_m}{n_m} \cdot (n_t - c_t) - \nu_{detrap} \cdot c_t \tag{4.2}$$

The first equation 4.1 describes the temporal variation of the concentration of mobile particles, in which ϕ is the ion flux (in $m^{-2}s^{-1}$), f(x) is the implantation distribution function, depending on the ion energy and approximated as a Gaussian, and r is the ions reflection coefficient (both f(x) and r are calculated with SRIM [28]). Such variation depends on the temperature-dependent diffusion coefficient ν_{diff} in m^2s^{-1} (second term of the equation) and from the HI trapping rate, described by the second equation 4.2. The second equation 4.2 describes the temporal evolution of trapped particles, which is proportional to the fraction of bulk interstitial sites containing an HI (c_m/n_m) and to the concentration of empty trapping sites ($n_t - c_t$), in m^{-3}. n_m is the concentration of bulk interstitial sites (in m^{-3}), while n_t is the concentration of trapping sites (in m^{-3}). Such variation is also proportional to the HI detrapping rate (second term of the equation). The boundary condition is set to $c_m(x = 0) = 0$ (instantaneous desorption), which means that the desorption of HIs from the surface is not the rate limiting step (as experiments also seem to suggest). Furthermore, MHIMS is a 1D model as it considers as spatial dimension only the direction orthogonal to the surface (towards the bulk of the material), assuming an homogeneous flux of incoming ions.

The simulations of the present work have been realized with the help and collaboration of Matthieu Latournerie (PIIM) and Etienne Hodille (CEA Cadarache). The code returns as outputs the desorption rate of D atoms from the surface as well as D depth profiles (concentration of mobile and trapped D atoms in the material, also called inventory, as a function of depth). To simulate the present work we leverage the results of reference [109], which developed a MHIMS model able to reproduce the HI retention behavior of polycristalline W samples. It assumes two kinds of trapping sites: an extrinsic, higher energy one (relative to the native oxide layer, whose thickness is fixed at 5 nm) and two intrinsic, lower energy ones (relative to two kinds of grain boundaries). We use as energies and densities values of the traps the ones retrieved for the modeling of polycristalline W experiments [109].

It is then necessary to specify that the D inventory values retrieved from MHIMS calculations are referred to the concentration of D atoms diffused and trapped in the first few tens µm from the surface (which is the working range of the code, see figure 4.10(a)). Spectroscopic ellipsometry, on the other hand, is a surface sensitive technique

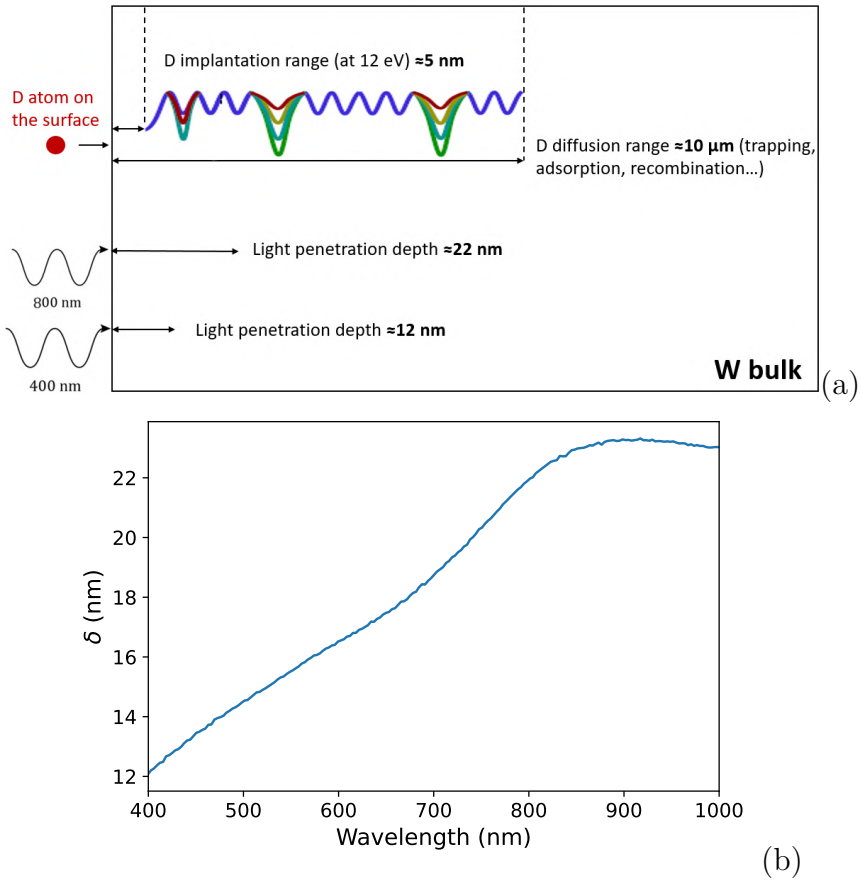


Figure 4.10: Schematics (not in scale) of D atoms implantation, diffusion range and light penetration depth in W (a); light penetration depth in W as a function of wavelength (b).

with a probing range that depends on the absorption properties of the material. For this reason, we calculate what we call the D "surface inventory", which is the inventory of D atoms in the region to which ellipsometry light is sensitive. The penetration depth of light into a material, in fact, depends both on light wavelength λ and on the extinction coefficient k of the material, as:

$$\delta = \frac{\lambda}{4\pi k} \tag{4.3}$$

Moreover, the intensity of light penetrating into the material decays exponentially following the Beer-Lambert law:

$$I(x, \lambda) = I_0(x = 0, \lambda) \exp(-x/\delta) \tag{4.4}$$

where δ is the light penetration depth previously defined and $I_0(x = 0, \lambda)$ is the light intensity of the incident beam at the surface (before it penetrates into the material). From this relation, the penetration depth δ is then defined as the depth below the surface at which the light intensity has fallen to 1/e of the initial value I_0 (about 37%). For bulk W in the working wavelength range of our ellipsometer (400-1000 nm), this depth is represented in figure 4.10(b) and is equal to 23 nm at λ=850 nm. We then calculate the surface inventory from the D depth profiles, as the integral of

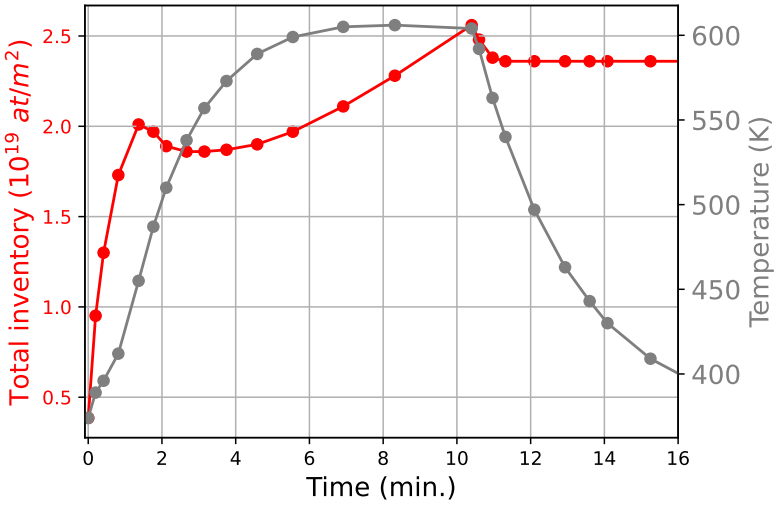


Figure 4.11: D total inventory (left scale) and W surface temperature (right scale), as a function of time. The plasma starts at t=0 min. and ends at t=10 min.

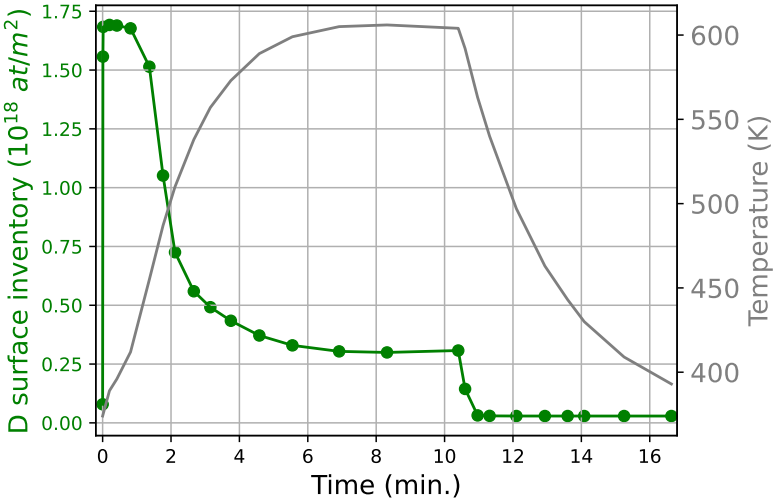


Figure 4.12: D surface inventory in the light penetration depth (left scale) and surface temperature (right scale), as a function of time. The plasma starts at t=0 min. and ends at t=10 min.

D concentration over a depth equal to the light penetration depth δ. To be more precise, the surface inventory is calculated as the weighted sum of the integral of D depth profiles from 0 (the surface) to 23 nm (depth at which the 63% of the incident light interacts with the material, at λ=850 nm) and of the integral of D depth profiles from 23 nm to 106 nm (depth at which the 99.99% of the incident light is lost in the material, at λ=850 nm).

Figure 4.11 represents on the left scale the D total inventory (red curve) as a function of time. On the right scale the temperature ramp during plasma exposure (grey curve) is represented, also as a function of time. Total inventory has a first "local" maximum at around t=1.7 min., corresponding to about 450 K in the temperature ramp, due to the trapping of D atoms below the surface. The temperature increase enhances the degassing of trapped D atoms causing a small decrease in the inventory,

which then increases again because of the predominance of bulk diffusion processes once the temperature is constant. When plasma stops, the total inventory decreases and saturates to a constant value, since the temperature is decreasing and inhibits the de-trapping of D atoms ("freezed" de-trapping). On the other hand, figure 4.12 represents the same kind of plot, but with D surface inventory instead of the total one (green curve). We can see that the D inventory along the penetration depth saturates very fast to the maximum ($1.7\text{x}10^{18} at/m^2$), which corresponds to t=1 min. of the implantation phase, reached at a temperature of 410 K. It decreases afterwards as a consequence of the desorption favoured by the temperature rise, and later stabilizes once the temperature is constant and diffusion in the bulk is predominant (as visible in the same implantation phase for total inventory in figure 4.11). For the same reasons described before for the total inventory, once the plasma stops also the surface inventory decreases, saturating to a constant value ($2.9\text{x}10^{16} at/m^2$).

4.5 Comparison of ellipsometry results and MHIMS modeling

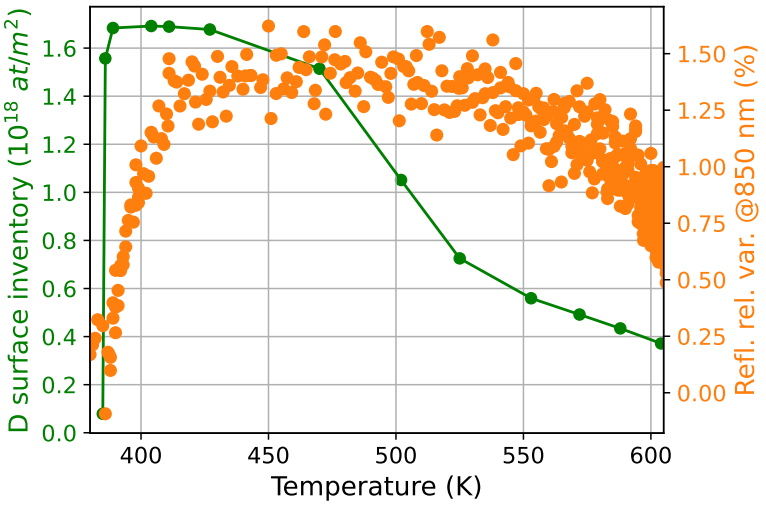


Figure 4.13: D surface inventory in the light penetration depth (green curve, left scale) and reflectivity relative variation at 850 nm measured with ellipsometry (orange curve, right scale), both as a function of surface temperature during plasma implantation phase.

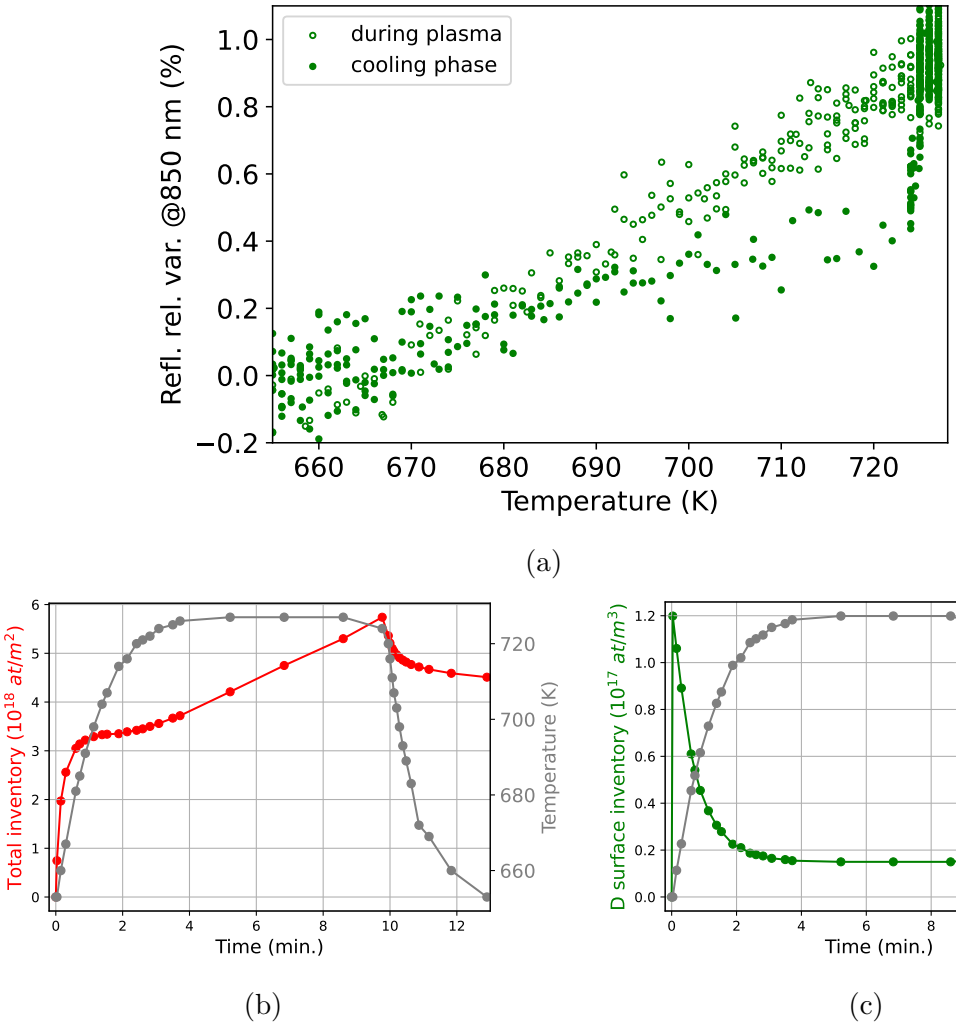
Figure 4.13 represents the D surface inventory modeled with MHIMS (on the left scale) and the reflectivity variation due to D/W interaction measured with ellipsometry (on the right scale), both as a function of temperature. It is possible to notice that they have a similar qualitative trend and both reach the maximum value at around 410 K, suggesting that there is good agreement between the model and the experiments. However, the D surface inventory modeled with MHIMS seems to predict a faster implantation phase with respect to the ellipsometry measurements. The discrepancy between the model and the experiments may be due to two different factors. On one hand, in the first minutes of the implantation phase, we may underestimate the

initial speed of the temperature ramp, as the measuring range of the pyrometer starts at 373 K and the error that we make in determining the temperature is bigger in this range. On the other hand, in the last part of the implantation phase, where desorption and diffusion processes take place, the discrepancy may be due either to the evolution of the native oxide during the exposure (already observed in chapter 3), or to a simplification done by MHIMS in modeling the kinds of traps present in the surface, as we only consider three kinds and only in one dimension (i.e., possible dislocations, dislocation loops, 3D voids or clusters are not taken into account). This would cause a faster saturation of D trapping in the surface followed by an easier de-trapping process.

4.6 Conclusions and perspectives: the effect of temperature

Eventually, as a last test on the effect of temperature on D retention and W reflectivity variation, we perform ellipsometric measurements heating the sample at 673 K before starting the experiment. As we can see in figure 4.14 (a), in this range of temperatures the thermal effect seems to counterbalance the D ions effect, as the total reflectivity variation is smaller in absolute value (1% compared to 3.3% of the room temperature exposure) and the two phases of plasma exposure and cooling seem to flatten and get closer, with a small difference in slope. Moreover, the D total and surface inventory calculated with MHIMS (figure 4.14 (b,c)) show the same qualitative trend of the room temperature plasma case, with smaller absolute values of concentrations (by one order of magnitude) and a less pronounced initial peak due to surface trapping of D atoms. This could be an evidence that the effect of temperature is mainly to accelerate the processes of D diffusion and desorption, smoothing the D total inventory curve and flattening the reflectivity variation curve (as already observed multiple times in this thesis).

In conclusion, in this chapter we have measured the modification of W optical response during D plasma exposure with *in-situ* spectroscopic ellipsometry. We observed a simultaneous and consistent rise of W surface temperature up to 600 K, detected by the pyrometer, and made some efforts in disentangling and estimating quantitatively the contribution of temperature and of D ions in the total W reflectivity variation occurring during the plasma exposure. For this purpose, we have made an annealing calibration measurement in which the sample is heated up to 600 K with an high power laser, without exposing it to plasma, in order to estimate only the temperature effect in reflectivity variation. We have then supposed that the temperature and the D ions effect, occurring simultaneously during plasma exposure, sum each other, and we have thus determined the D contribution by subtracting the annealing calibration measurement to the total reflectivity variation. We have then looked at the D contribution as a function of temperature and wavelength, and observed that it reaches its maximum value at around 410 K where it contributes to almost the total (98%) of W reflectivity variation. As the temperature increases during the exposure, the D contribution decreases to 75% of the total at 450 K, then to the 53% at 500 K and finally at 37% at 600 K, which is the maximum temperature corresponding to the plateau region. We have used the code MHIMS to model the concentration of D



(a)

(b)

(c)

Figure 4.14: (a) Reflectivity relative variation at 850 nm as a function of temperature, during plasma exposure performed at 673 K (green full dots) and during the cooling phase as the plasma is off (green empty dots). (b) D total and (c) surface inventory (left scale) and W surface temperature (right scale), as a function of time, during the plasma exposure at 673 K. The plasma starts at t=0 min. and ends at t=10 min.

atoms being trapped and diffusing in the material. We have found that the D surface inventory (which is equal to the D atoms concentration in the first 23 nm from the surface, i.e. the penetration depth of 850 nm light in W) reaches its maximum at 410 K, indicating a saturation of D trapping in this region, and decreases afterwards as a combined effect of temperature-induced desorption and bulk diffusion. We observe good agreement between MHIMS modeling and ellipsometric measurements, however the modeling predicts slightly faster implantation and desorption phases. We address this discrepancy to a simplification of MHIMS in modeling realistically the kinds of traps present in the material (which would cause a faster de-trapping and desorption phase), and also to a limitation in the measuring range of the pyrometer, which causes a bigger uncertainty on the temperature measured in initial phase of the implantation, and may result in underestimating the slope of the reflectivity variation curve in the phase of temperature rise. We would like to specify that, in our experiments, the

observed increase of surface temperature during plasma exposure was probably due to a non-optimal thermal contact between the sample and the sample-holder (a W foil disk initially designed to support bigger samples than our 10x10 mm^2 ones). We could not succeed in using a chiller in order to cool down the system and prevent such temperature rise, nevertheless we have done the same experiments (which we do not show here) on W samples with a bigger exposed surface (described in section 2.1.1) and managed to have a lower temperature rise (by about 100 K), but still observed the same qualitative behaviour of ellipsometric signal. About the choice of the pyrometer for temperatures measurements, we believe it retrieves a more accurate result of the actual temperature at the surface as compared to the thermocouple, which is placed on the backside of the sample-holder. As it may seems contradictory to use a pyrometer to determine reflectivity and thus emissivity, we stress that the temperature errors bars are just 1-5 K within a variation of W emissivity by 0.1.

In the end, we have demonstrated that *in-situ* spectroscopic ellipsometry is a versatile and convenient tool that allows to characterize W surface state modification during plasma exposure. As D plasma conditions that we have used in this study do not induce any considerable modification in W surface morphology and roughness (confirmed by CM and AFM measurements performed before and after the exposure), we were able to focus on the effect of D/W interaction in the optical response modification and, in addition, to compare such information with the results obtained from a modeling of D surface inventory. As future perspective for a possible continuation of this work, we aim to investigate more in depth on the effect of D ions in modifying W dielectric function, by including a dependence of the oscillators parameters of the Lorentz-Drude model from the D surface inventory, which could affect mostly the plasma frequency as well as the damping factors of the oscillators.

Chapter 5

In-situ monitoring of W oxides reduction by D plasma

In the framework of nuclear fusion reactors such as ITER, especially in the divertor region, the oxidation of W PFCs should also be taken into account, as oxygen can be present inside the reactor at any time as an intrinsic impurity, or during an accidental scenario involving external air and/or water leaks. Knowing that the PFCs surface temperature during discharges can increase up to 1300 K in steady-state [71] and due to the strong chemical affinity of oxygen with W, it is not unlikely to have oxide formation on W walls [76], altering the surface properties of W PFCs and giving rise to issues of fuel retention, material erosion and recycling [110].

Upon W thermal oxidation, the most stable oxide phase in the temperature range 300-1600 K is tungsten trioxide (WO_3), which has a simple cubic perovskite-like crystal structure. The crystal lattice structure, however, strongly depends on the oxidation temperature. As this one increases, in fact, the cubic lattice is distorted, resulting in asymmetric structures with different lattice parameters and angles (in particular, monoclinic, triclinic, orthorombic and tetragonal). The structure of the oxide formed at a specific temperature is then irreversible as the temperature is decreased [111]. In most of the experimental works, the most observed crystal phases of W oxides are: $WO_2, WO_{2.72}, WO_{2.9}, WO_3$. In addition, the oxidation rate is also dependent on W crystal orientation. Previous studies [112] have demonstrated that W oxide thickness is about twice bigger for (100) W crystal grains than (111) ones, resulting in an inhomogeneous oxide growth.

WO_3 is extensively studied in the context of electro-chromic materials, whose optical properties are modified by the insertion/ extraction of ions or electrons, mainly studied for applications in smart windows or low emissivity coatings [113, 114]. Previous studies have already shown the change of WO_3 from transparent to absorbing state (in the visible range) upon hydrogen or lithium intercalation, evidenced by a color change [115]. Furthermore, in the context of fusion it is known that the interaction between WO_3 and D ions can lead, among other things, to a higher fuel retention [116], to oxide erosion [117] (which may then enhance impurities content in the core plasma) and to W bronzes (D_xWO_3) formation [118]. It is clear from such studies that the oxide reduction by D ions is a temperature-driven process. Recently, Kremer et al. [119] exposed thin (<100 nm) thermally grown WO_3 samples to low energy (5 eV/D), low flux ($\simeq 6 \times 10^{19} D/m^2 s$) and high fluence ($\simeq 1 \times 10^{24} D/m^2$) D plasma at 370 K,

and observed with Rutherford Backscattering Spectrocopy (RBS) the appearance of a W-enriched layer about 13 nm thick. In a subsequent study[120], they also observed that the oxygen removal rate could be increased 3 fold when increasing the ions kinetic energy above 35 eV or when increasing the surface temperature to 500 K. However, in the latter case the plasma exposure temperature is relatively close to the growth temperature used for their WO_3 synthesis (600 K), raising questions about thermal stability.

In this study, we aim to contribute to the understanding of WO_3 layers evolution under low energy D plasma. To this end, we prepared thermally grown WO_3 samples synthetized at 1073 K and thermally stable up to 800 K (following a similar procedure as the one described in [49]). Then, we exposed these samples to 15 eV/D plasma at 373 K or 650 K. The novelty of our study is that the surface evolution of WO_3 is followed continuously using *in-situ* spectroscopic ellipsometry. By coupling the results of *in-situ* ellipsometry with *ex-situ* surface characterization methods, our goal is to test the use of *in-situ* ellipsometry as a possible non-contact and non-intrusive diagnostics for the oxidation/reduction evolution of PFCs materials in fusion applications.

5.1 Sample preparation and plasma exposure

We use two W square samples 10x10x0.5 mm^3 provided by GoodFellow, which are mechanically polished to have a mirror-like surface, with a root mean square (RMS) roughness of about 10 nm (on an area of 130x175μm^2). They are then electro-polished using a 1.5% NaOH solution, for 15 s, with a tension of 7 V between the sample and the reference electrode. This is done in order to remove material without inducing mechanical deformation and to better visualize the crystalline grains. The samples are then cleaned in ultra-sound baths of acetone (20 minutes), ethanol (20 minutes) and distilled water (20 minutes), and eventually rinsed with optical paper. They are then annealed in vacuum at 1073 K for 30 minutes with an high power laser, in order to reduce surface contamination.

	Oxide growth conditions				**Plasma conditions**		
	Temp.	**Pressure**	**Time**	**Thickness**	**Flux**	**Fluence**	**Temp**
	K	mbar	s	nm	$D^+ \cdot m^{-2} \cdot s^{-1}$	$D^+ \cdot m^{-2}$	K
Wox1	1073	0.73	20	70± 18 nm	1.7×10^{20}	1×10^{23}	650
Wox2	1073	6.73	5	328 ± 84 nm	2×10^{19}	$1 \times 10^{24*}$	373

Table 5.1: Experimental parameters of the samples oxidation process (temperature, oxygen pressure and time), the thickness of the oxide layer before plamsa exposure and the plasma conditions (ion flux, fluence and temperature). *This is a value of cumulated fluence that was reached with an average ion fluence of $5.5 \times 10^{22} D^+ \cdot m^{-2}$ for each exposure.

The thermal oxidation is performed in the experimental set-up CAsPEr (described in section 2.1.2). The experimental parameters used for W oxidation, resumed in table 5.1, reproduce the realistic temperature conditions in which oxide layers could be formed on W PFCs inside an ITER-like reactor considering water and/or air leak at high temperatures. The samples were oxidized in vacuum (base pressure: 10^{-7} mbar), reaching the oxidation temperature of 1073 K through an oven. Different values of

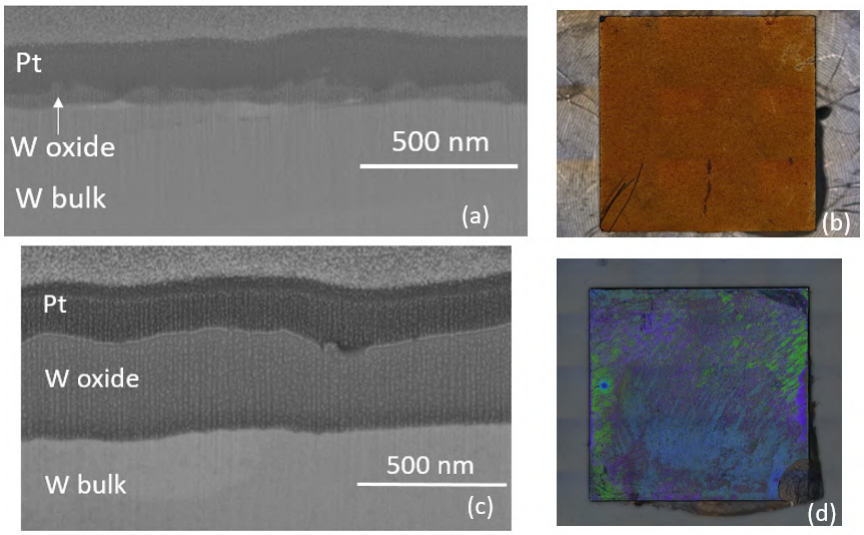


Figure 5.1: FIB-SEM section images of Wox1 (a) and Wox2 (c) samples, before plasma exposure, and their correspondent confocal microscopy images on the right (b,d).

gas pressure and oxidation times were used, in order to grow oxides with different thickness. The purpose of realizing two different thicknesses was to observe a fast reduction by D plasma in the sample Wox1 (exposed at high temperature), in order to extract by ellipsometry the optical indexes of a fully reduced layer. These optical indexes will then be used to estimate with ellipsometry the thickness of the W-enriched layer in the sample Wox2 (exposed at low temperature). As we were not certain of the reduction rate at low temperature, we decided to grow a thicker oxide (300 nm), in order to avoid full reduction upon D plasma exposure.

Figure 5.1 shows FIB-SEM cross-sectional images of the oxides after a FIB cut. The platinum layer, deposited on a few μm^2 area where the cut is performed, has a protective purpose and it is not removed before plasma exposure. The oxide layer thickness of the samples, retrieved with the software ImageJ, is 70±18 nm for Wox1 and 328±84 nm for Wox2. It is possible to see that both oxides presented an irregular structure and were rather inhomogeneous in thickness. Furthermore, they were differently colored (dark gold for Wox1, dark blue for Wox2) which, as it was already observed in previous studies [48], depends both on the layer thickness (causing different light interference phenomena) and on the crystalline structure. Raman spectra (figure 5.2) displayed the typical peaks of WO_3 monoclinic crystalline phase at wavenumbers 218, 327, 434, 715 and 807 cm^{-1} ([121]), which resulted to be quite broad, as compared to the same crystalline phase synthetized at lower temperatures ([110]). This feature suggests a disordered structure with the presence of defects (mostly oxygen vacancies), making us refer to the oxides as WO_{3-x} or, more simply, WO_x.

SEM measurements show crystalline grains with size of about 1-2 µm (figure 5.3(a)) and nanowires structures (typical of thermally evaporated grown oxides [122]), with preferential directions along different grains (figure 5.3(b)).

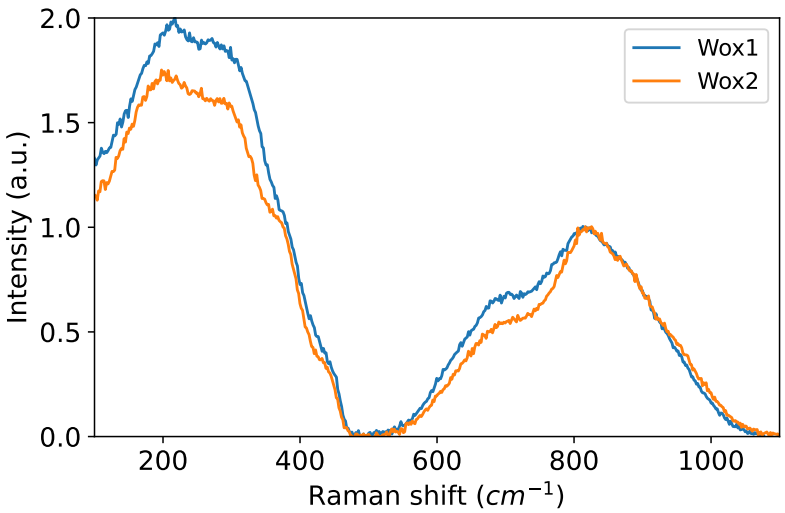


Figure 5.2: Raman spectra of the two samples Wox1 and Wox2, as-synthetized.

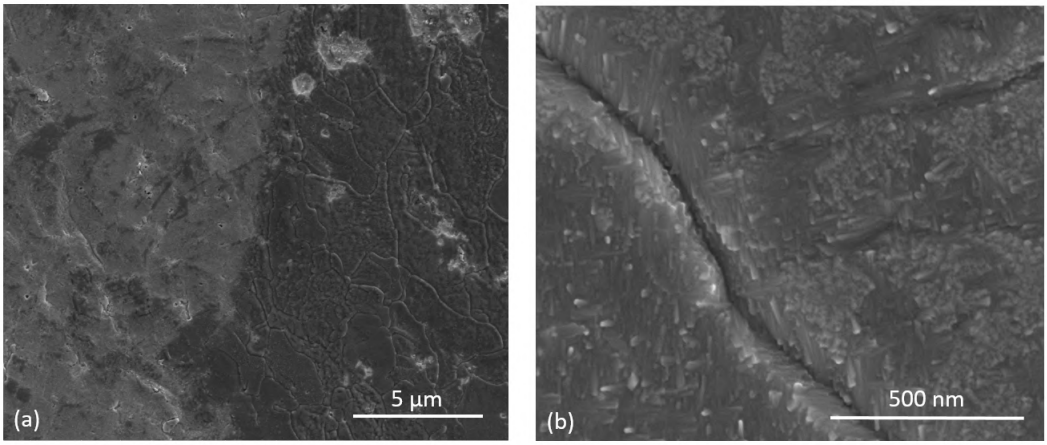


Figure 5.3: SEM images (secondary electron mode) of the sample Wox2 before D plasma exposure, at magnification 50k (a) and 75k (b).

5.2 Oxide reduction by D ions: increase of extinction coefficient k

The experimental parameters of the D plasma exposure are resumed in table 5.1. The sample Wox1 is exposed to D plasma in the CAMITER experimental set-up, with a ion flux of 1.7x10^{20} $D^+ \cdot m^{-2} \cdot s^{-1}$ for 10 minutes, reaching a fluence of 1x10^{23} $D^+ \cdot m^{-2}$ and a maximum temperature of 650 K. The ion energy is around 12 eV since the sample is floating.

As seen in figure 5.4, before D plasma exposure the indexes resemble the ones of a dielectric layer (with extinction coefficient k close to 0), while after the exposure they resemble to the ones typical of a metal (with k increasing at higher wavelengths). The spectral behaviour of the refractive index n is not trivial, hence, even if we show both, we prefer to use k as a clear-cut marker of the electronic properties of the material. For comparison, in figure 5.4 we also show the optical constants n,k of pure W (from Rakic

et al.[123]) and of an ideal WO_3 (from Kulikova et al.[124]), to better highlight the change in the optical constants of Wox1 that we observe after plasma exposure. It is important to specify that in our case even before the exposure we do not have perfectly zero absorption, as our oxides are not perfectly stoichiometric WO_3 and probably have some lattice defects which induce light absorption from color centers. We then fitted the *in-situ* ellipsometric data obtained during D plasma exposure (figure 5.5) using an effective-medium approximation (EMA) layer on a W substrate. As mentioned in section 2.2.4, such layer is composed by two coexisting material phases, in which the material phase A would have optical constants n,k of Wox1 before plasma exposure and the material phase B would have the n,k of Wox1 after plasma exposure. The bigger variation of Ψ and Δ at 400 nm compared to the other wavelengths is probably due to the fact that the penetration depth of 400 nm light in the oxide is closer to its thickness ($\simeq$70 nm), causing light interference effects which thus impact more on this wavelength. In the fitting procedure, the layer thickness was constrained to the thickness range measured with FIB-SEM, resulting in the value 54$\pm$3 nm. The EMA percentage (corresponding to the percentage of the second material, Wox1 after plasma exposure) was left as a free parameter evolving with time. In figure 5.6, we show that the EMA percentage goes from 0% before D plasma exposure (i.e., the EMA layer entirely corresponds to a dielectric layer) and increases during plasma exposure, until it reaches 100% (i.e., the EMA layer resembles to a metallic material) after about 5 minutes, and maintaining this value until the end of D plasma exposure (at t=10 min.) and even after plasma exposure.

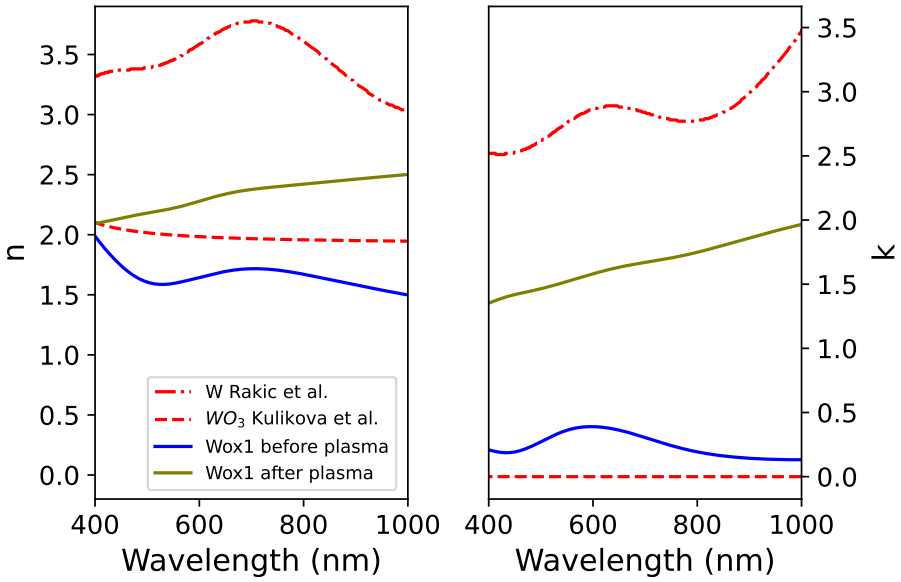


Figure 5.4: Refractive index n (a) and extinction coefficient k (b) of the sample Wox1 before and after plasma exposure, and comparison with the typical indexes values of ideal WO_3 and W (retrieved from Kulikova et al.[124] and Rakic et al.[123], respectively).

We find a good agreement between the model and the experimental data, except during the first 3 minutes of the D plasma exposure, which correspond to an exponential increase of the surface temperature up to 650 K (after 3 minutes, the temperature

remains constant at this value until the end of the plasma exposure). This could be due to the fact that the EMA described in equation 2.26 of section 2.2.4 is only valid when the second material fraction is low in comparison to the first material. Since between 1 and 3 minutes the layer is evolving from the pre-exposure state to the post-exposure state, the two fraction are comparable and the validity of the model is not fulfilled. We presume that the synergistic effect of plasma irradiation and temperature increase causes an abrupt change in the surface state, for which we cannot find a satisfying agreement with other models (i.e. homogeneous layer, graded layer) in this time range. The drastic change in the oxide surface state and optical response is visible by naked eye, since the Wox1, initially dark gold, turned brighter and metallic once exposed to the D plasma (figure 5.7(b)). FIB-SEM measurement (figure 5.7(a)) evidenced a substantial reduction of the oxide layer, as seen by the brighter and more inhomogeneous oxide layer as compared to the pristine one before plasma exposure. As the ion energy is far below the physical sputtering threshold for D ions on W oxide (around 65 eV [125]), we suppose that a chemical sputtering of the oxide by D ions, enhanced by the simultaneous temperature increase, is responsible for the oxide layer reduction. This would result in a more disordered and oxygen-depleted oxide layer due to the creation of defects such as oxygen vacancies, with physical properties that are the ones typical of a metallic surface. We stress that the temperature rise is directly linked to the presence of the plasma and its ion flux, as we do not heat the system before the exposure, and that we could not investigate the two effects separately as in the current version of our set-up it is not possible to efficiently cool down the sample.

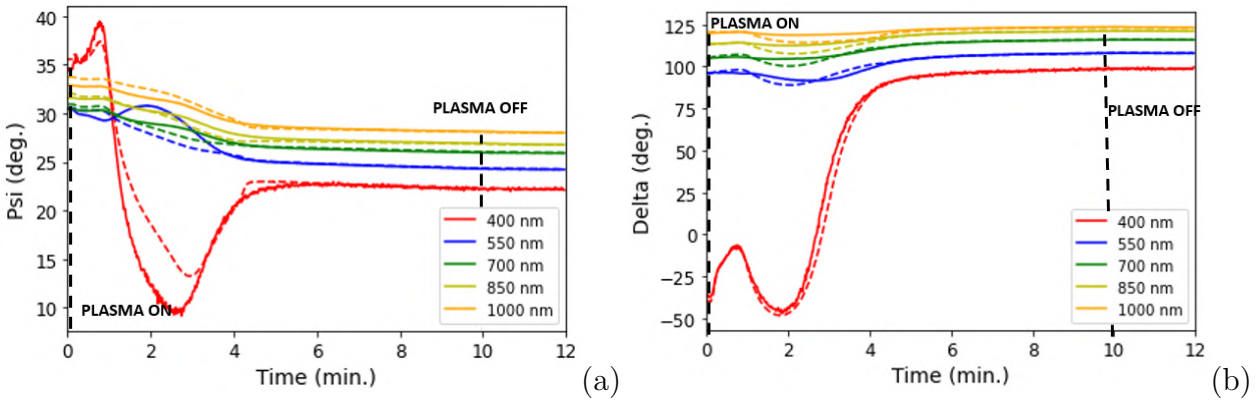


Figure 5.5: Plots of Wox1 experimental (solid lines) and model (dashed lines) Ψ (a) and Δ (b), as a function of time during D plasma exposure (starting at t=0 min. and ending at t=10 min.), for 5 different wavelengths.

5.3 Oxide reduction by D ions: indirect measurement of W enriched layer

In order to slow down the oxide reduction and to follow its evolution with increasing fluence, we exposed the second sample (Wox2) to a "gentle" D plasma, i.e. with a lower ion flux of $2\text{x}10^{19} D^+ \cdot m^{-2} \cdot s^{-1}$, and thus a lower heat flux, as the sample temperature was not exceeding 373 K during this "gentle" D plasma exposure. We performed

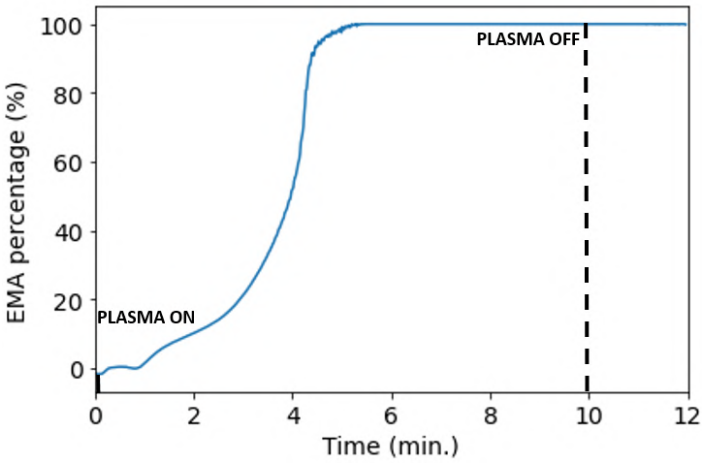


Figure 5.6: EMA percentage (of the metallic WO_x layer) of sample Wox1 as a function of time.

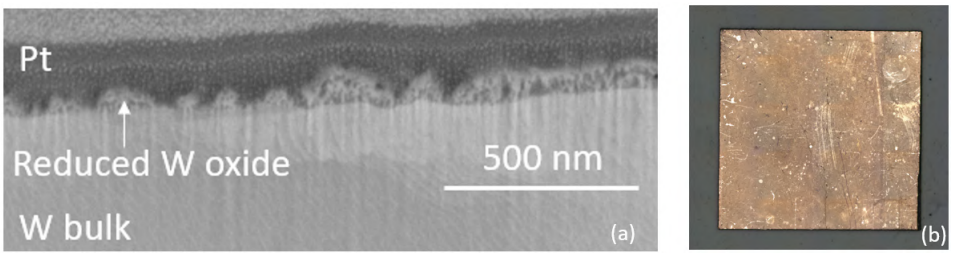


Figure 5.7: Wox1 after D plasma exposure: FIB-SEM image (a) and confocal microscopy image (b).

ellipsometric measurements during 10 successive D plasma exposures of various times, until reaching a cumulated fluence of $1x10^{24} D^+ \cdot m^{-2}$. In addition, between each D plasma exposure, we performed XPS measurements, in order to characterize any change in the W oxidation state. We stress that we do not see any kinetic evolution of the oxide because of the sample transfer between the plasma chamber and the XPS apparatus, since the air transfer was systematically realized in less than a few minutes.

For the Wox2 sample, we do not model the *in-situ* data during each exposure but rather focus on the values of Ψ and Δ after each exposure, as we do not observe big variation of the optical signal during the plasma. In this case, we do not use the EMA model as we do not have two co-exisiting material phases, i.e. the FIB-SEM measurement did not show a full reduction of the oxide but instead a seemingly unmodified oxide. Thus, in a first step, we modeled the system as an homogeneous layer with unknown optical constants, in which we constrained the layer thickness to the range measured with FIB-SEM, resulting in a thickness value of 260±40 nm, and set the optical constants n,k of the layer as free parameters of the fit. We choose to show in figure 5.8 the indexes n and k as a function of wavelength, at the end of each exposure (so with increasing cumulated fluence). While for n the behaviour is not continuous with increasing fluence, it seems here that a similar process as the one occurring in the thin sample Wox1 is taking place, namely a progressive increase of k with increasing cumulated fluence, going from values close to 0 (typical of a dielectric layer) before the exposure, to higher values of k at higher wavelengths (typical of a

metallic surface). We represent in the same graph the extinction coefficient of an ideal WO_3 and a pure W material, to better show the transition from one kind of surface to the other one after each plasma exposure. Considering the similar evolution of n and k observed with Wox1 and Wox2, in the following we will base our discussion on the behaviour of k, as the spectral behaviour of n is not trivial and it is not a clear indicator of the electrical properties of the material, unlike k (which is directly proportional to e.g. the electrical conductivity).

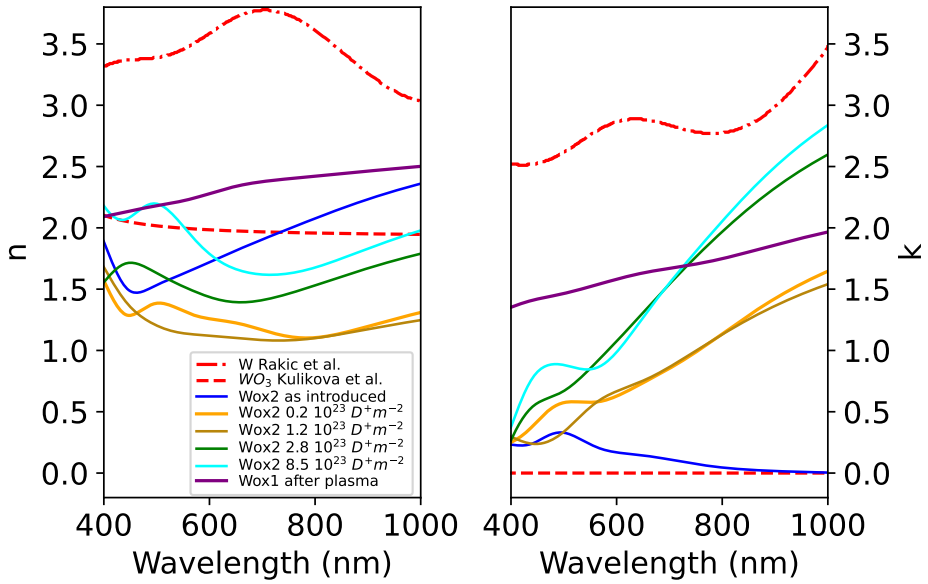


Figure 5.8: Optical indexes n and k of sample Wox2 as a function of wavelength after different plasma exposures (e.g., with increasing cumulated fluence)„ assuming that the oxide layer is homogeneous. These indexes are compared with the ones of ideal WO_3 and W (from Kulikova et al.[124] and Rakic et al.[123], respectively) and of the exposed sample Wox1.

In order to understand the strong variation observed on the extinction coefficient k upon D plasma exposure despite a seemingly unmodified FIB-SEM measurement, we performed XPS measurement to characterize the near-surface region of Wox2. Top panel in figure 5.9 shows XPS spectra in the 28-41 eV binding energy region (W4f) of the sample Wox2, as introduced and after multiple exposures to D plasma (with increasing cumulated fluence). XPS spectra denote a progressive change in the surface chemical environment (W oxidation state) with increasing cumulated fluence. As evidenced in the histogram in the bottom panel of figure 5.9, which depicts the abundance of each W oxidation state (corresponding to a peak at a specific binding energy), we start with a predominance of W^{6+} peak (relative to WO_3, at 35.4 eV) for the as introduced sample, as well as after the first D plasma. With increasing cumulated fluence, also other oxidation levels W^{5+} and W^{4+} (relative to the sub-stoichiometric oxides $WO_{2.72}$ and WO_2, at 33.9 and 32.5 eV, respectively) appear, until reaching, at the end of plasma exposures, a predominance of metallic W 4f peaks (at 31.1 eV), which already start to appear at a cumulated fluence of $2.8 \times 10^{23} D^+ \cdot m^{-2}$.

Figure 5.10 (left side) represents an example of a fit of an XPS spectrum (in particular, the one relative to the sample exposed at a D fluence of $8.5 \times 10^{23} D^+ \cdot m^{-2}$).

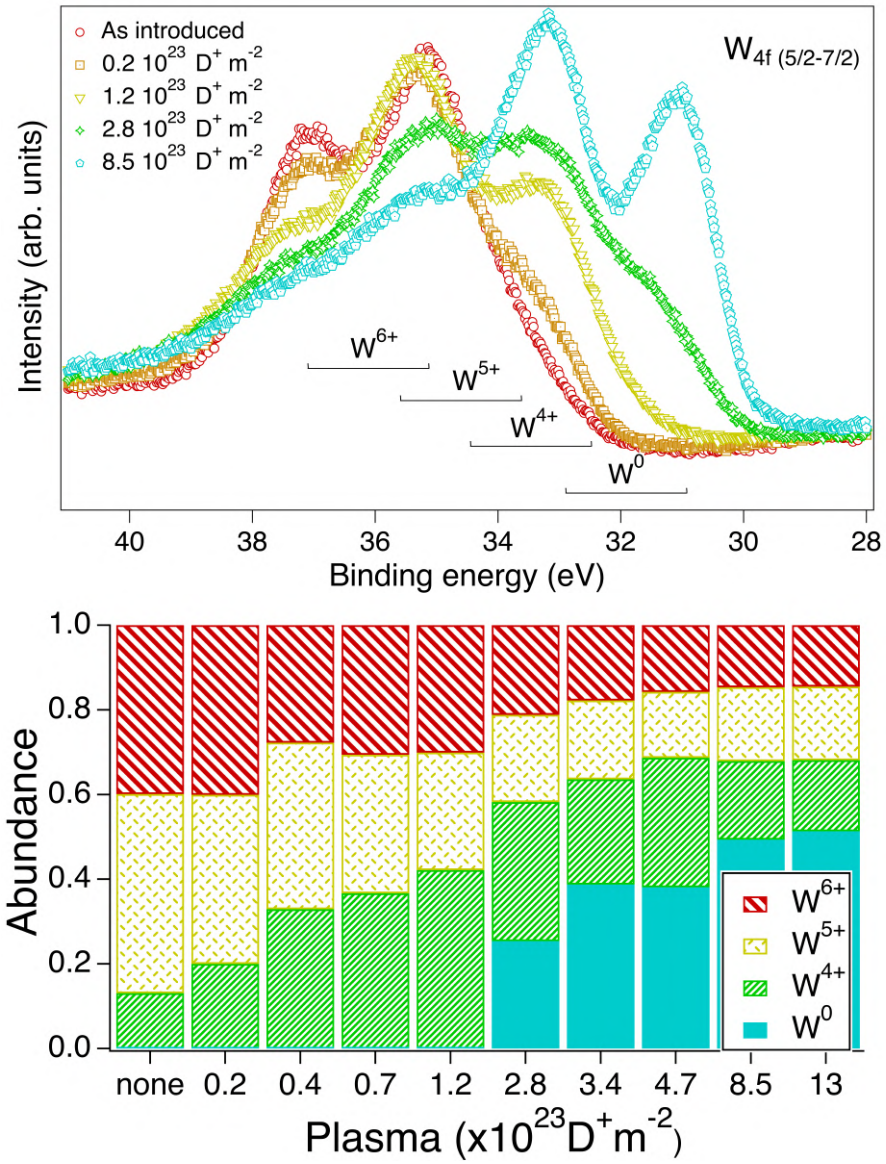
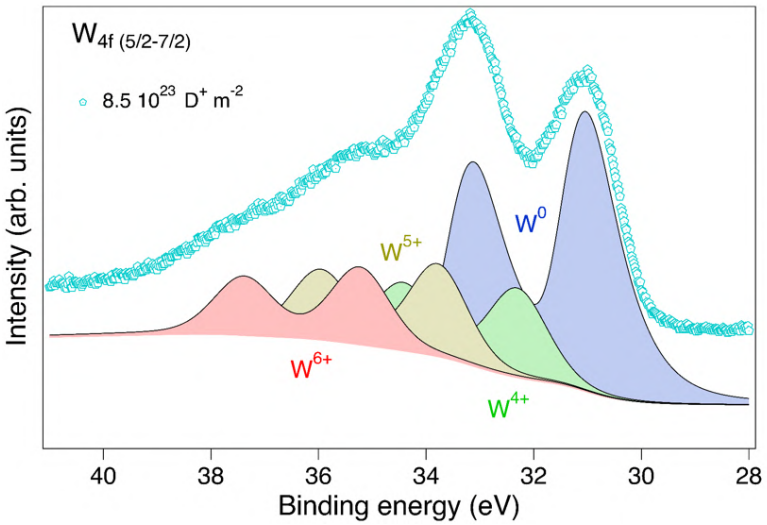


Figure 5.9: Top: XPS spectra of Wox2 for different values of cumulated D fluence. Bottom: Histogram representing the peaks predominance in XPS spectra for each value of cumulated fluence, going from highest binding energy (W^{6+}) to the lowest (W^{4+}), to finally metallic W.

Binding energy values for the $W_{4f7/2}$ and $W_{4f5/2}$ peak-shape are based on a survey of literature values (NIST database [91]). The table in figure 5.10 (right side) contains the binding energy values of the peaks used for the fit. The peak to peak ratio is fixed as well as the doublet energy splitting (2.1 eV). Since in the literature there is no binding energy relative to the peak of sub-stoichiometric oxides, the value we use for $WO_{2.72}$ (correspondent to the oxidation state W^{5+}) was extrapolated from a linear fit between the values relatives to WO_3 and WO_2.

After the multiple D plasma exposures, we measured the oxide layer thickness with FIB-SEM, where we do not observe any thickness variation or other change in the oxide layer morphology (figure 5.11). Therefore, we conclude that the variation in the optical properties and in the chemical composition of the oxide that we detect with



W ox. state	B.E. 7/2 peak (eV)	B.E. 5/2 peak (eV)
W^0	31.1	33.2
W^{4+}	32.5	34.6
W^{5+}	33.9	36.1
W^{6+}	35.4	37.5

Figure 5.10: Example of fit of W 4f peaks relative to the XPS spectrum of the sample Wox2, exposed at a D ion fluence of $8.5 \times 10^{23} D^+ \cdot m^{-2}$, and corresponding table containing the binding energy of each peak.

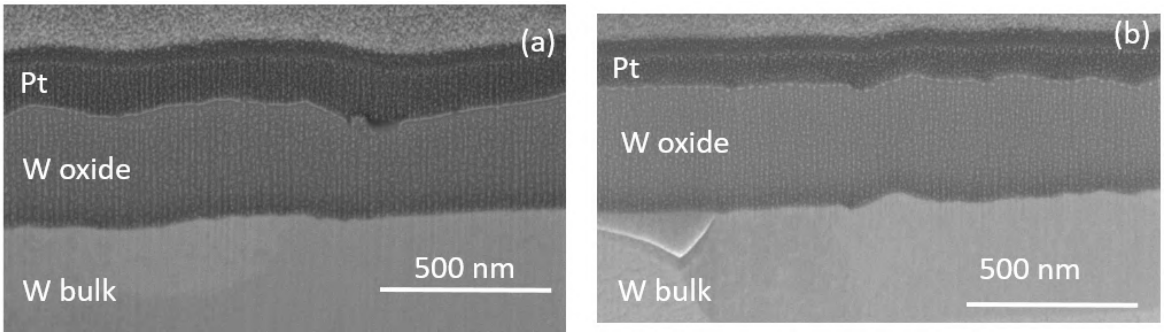


Figure 5.11: FIB-SEM images of Wox2 before (a) and after (b) D plasma exposure.

ellipsometry and XPS, respectively, are related to an oxygen-depleted (or W-enriched) surface layer of no more than 5 nm thick, consistent with previous studies with similar exposure conditions [49, 119]. The formation of such layer could be due to the same chemical sputtering process that occurs in sample Wox1, however with a less drastic change because of the lower sample temperature during D plasma exposure.

In order to confirm the appearance of the W-enriched layer at fluences $> 2.8{\times}10^{23} D^+ \cdot m^{-2}$ observed by XPS, we use ellipsometry to model the system as a stack of layers on a W substrate (figure 5.12(a)). We use for the W-enriched layer the same indexes of sample Wox1, i.e. an oxide fully reduced after the plasma exposure, while we fit its thickness and the indexes n,k of the underlying oxide. We find that the optical indexes of the underlying oxide do not evolve significantly with increasing fluence (figure 5.12(c,d)), while the thickness of the W-enriched layer (reduced oxide) grows up to 4.9±1.9 nm after the last plasma exposure (figure 5.12(b)). To summarize, we are able to detect the presence of a W-enriched layer though ellipsometry and XPS, which are both surface sensitive techniques, while with FIB-SEM we are not able to observe it, as the W-enriched layer thickness should be close to the resolution limit of the microscopy technique ($\simeq$5 nm). We believe that the surface temperature increase

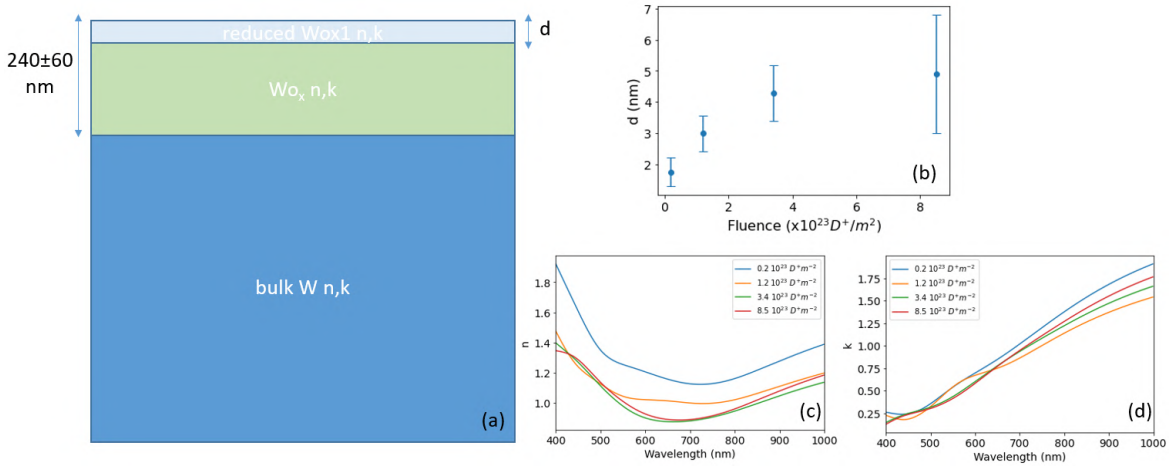


Figure 5.12: Schematic representation of the stack layer model (a) used to fit the W-enriched layer thickness (b) and the optical indexes n,k of the underlying layer WOx (c,d).

during D plasma may be a decisive parameter in determining the surface modification of W oxides and its extension in depth, independently from the thickness of the oxide. This would agree with the studies of Alimov et al.[116] and Tu et al.[117], and complete the ones of Kremer et al.[120] which also explore the role of ion energy. Despite similar experimental conditions, we do not observe a ≃10 nm W-enriched layer as the one in Kremer et al. [119], possibly due to slight differences in the plasma exposure or more significant differences in the thermal growth of the samples.

5.4 Conclusions and perspectives

In conclusion, in this study we performed ellipsometric measurements on W thermally grown (1073 K) W oxides exposed to D plasma at two different surface temperatures of 650 K and 373 K, respectively. In the case of the high temperature exposure, we observed a drastic change in the optical constants n and k, which go from the values typical of a dielectric layer before the exposure, to the ones typical of a metallic surface after plasma exposure. Since the ion energy (12 eV) is below the physical sputtering threshold, we attribute the surface modification to a chemical sputtering of the oxide layer by D ions, confirmed by *ex-situ* FIB-SEM measurements. In the case of the low temperature exposure, we observed a similar change of the optical constants and, in particular, an important increase of the extinction coefficient k in the near infra-red, suggesting again a transition towards a surface with metallic physical properties. XPS measurements also showed a change in W oxidation state with increasing cumulated fluence, in particular, going from a predominance of WO_3 peaks to a mixture of WO_3 and WO_2, and finally to the predominance of metallic W4f peaks at a fluence of $2.8{\times}10^{23} D \cdot m^{-2}$. However, for the low temperature exposure we did not observe any change in the layer morphology and thickness, i.e. the change occurs below the FIB-SEM resolution of ≃5 nm. These results suggest that the W-enriched layer is limited to the near-surface layer (1-5 nm), to which we are sensitive with both ellipsometry and XPS. As for the high temperature exposure sample, the similar optical properties

evolution with D plasma exposure is also due to the chemical change in the near-surface layer, but the thermally accelerated oxide reduction allowed to observe these effects with FIB-SEM on the whole oxide thickness.

Finally, we have proved that we are able to investigate the surface modification of W oxides during D plasma irradiation using an easy, non-destructive and non-invasive technique as *in-situ* ellipsometry, whose results are confirmed by *ex-situ* techniques such as XPS and FIB-SEM. In future works, we aim to investigate on the single and separate effect of ion flux and surface temperature in the oxide reduction, as well as to perform TEM (Transmission Electron Microscopy) measurements on "gentle" plasma exposed oxides, in order to test the presence of <5 nm W-enriched layer. Once the actual value of the thickness of the W-enriched layer is measured, we should be able to model with more precision the optical constants of such layer.

Chapter 6

Microscopic and macroscopic investigation of He bubbles formation in W

In this chapter, we will present the results of *in-situ* ellipsometric measurements realized on W samples exposed to He plasma, under specific conditions of temperature, ion flux, fluence and energy known to induce He bubbles formation and below W fuzz formation threshold [24].

At temperatures lower than 1073 K, exposure to He ions often leads to the formation of so-called "He bubbles". These are 3D voids (W vacancies clusters) that can extend along the W bulk and are filled by He atoms. The He bubbles can be created by self-trapped He atoms at room temperature, where an interstitial He atoms cluster generates a Frenkel pair (W vacancy/interstitial pair) and the He atoms bind to the W vacancy to form a He-vacancy "cluster", to which we refer as "bubble" (each of these self-trapped bubbles has from 2 to 7 He atoms inside, see [126]). At temperatures around 500 K, He bubbles become mobile [127], leading to the coalescence and growth of He bubbles with bigger volume. Such growth process can lead to a high pressure of He gas in the bubble (of the order of GPa [128]), which can then undergo pressure relief emitting dislocation lines, that are in turn able to trap more He atoms and thus enhance the growth of bubbles nearby [129]. The over-pressurized bubbles located close to the surface may then undergo pressure relief via bursting on the surface, displaying what we see as holes on the W surface. The first immediate effect of He bubbles formation on W surface morphology is the increased roughness of W (simultaneous presence of undulating structures and holes). Many factors such as temperature, ion flux and fluence conditions play a role in determining the size, density and depth distribution of He bubbles in W. Previous studies showed the creation of He bubbles with different shapes, either spherical [130] or, more often, faceted (in which facets are aligned along specific crystallographic orientations) [131, 16]. Recent works [132] have studied He bubbles shape evolution with *in-situ* techniques employing X-rays and evidenced the presence of He bubbles made of {110} and {100} oriented facets. However, single crystal W was used and irradiated with He ions with an energy of a few keV, which do not really represent the realistic conditions of W PFCs in the power exhaust region of ITER. Moreover, there are in literature some results that exploit ellipsometry to monitor the surface state of He irradiated W [133, 134],

which evidenced, for example, a correlation between the post-annealed W fuzz layer thickness and the $\Psi - \Delta$ trajectory and/or the extinction coefficient k [135]. Those studies give already an idea of the possible use of spectroscopic ellipsometry and its versatility in studying in real time and in a non-intrusive way surface processes of W PFCs.

In this study, we investigate the formation of He bubbles on different W samples during He plasma with a double purpose: first, to use *ex-situ* imaging techniques to characterize microscopically the size and density of He bubbles as a function of temperature and grain orientation; and secondly, to use *in-situ* spectroscopic ellipsometry to reconstruct the kinetics of bubbles formation and roughness evolution.

6.1 Experimental methods and conditions

Five different GoodFellow round samples with a diameter of 22 mm and a thickness of 0.5 mm are mechanically polished, electro-polished and annealed in vacuum at 1073 K (see section 2.1.1).

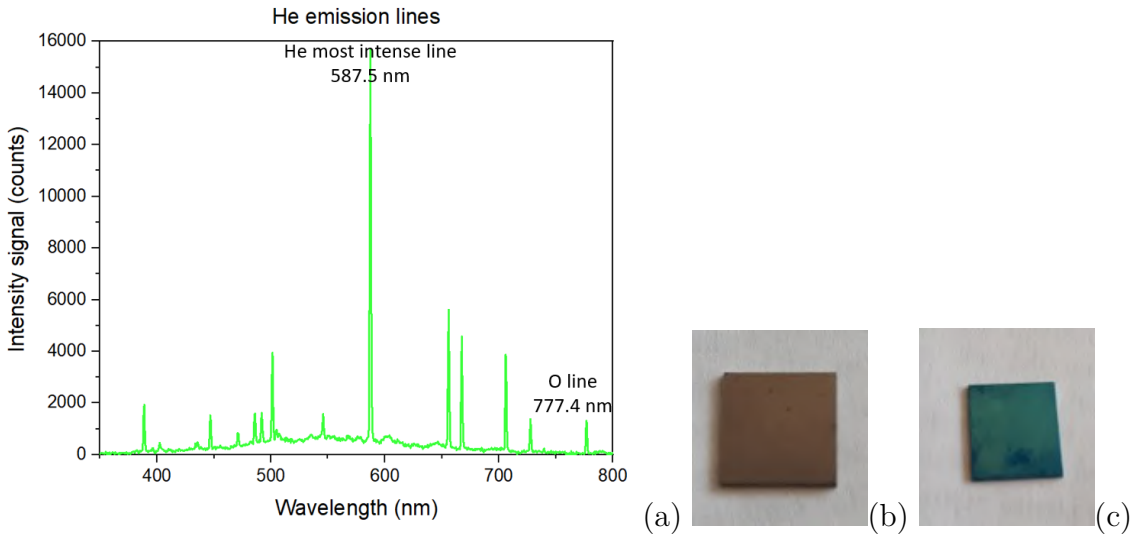


Figure 6.1: Emission spectrum of He plasma contaminated with oxygen, evidenced by the line at 777.4 nm (a); pictures of W sample before (b) and after (c) exposure to the contaminated He plasma.

Before performing systematical optical measurements, we exposed a test W sample to He plasma in CAMITER (section 2.1.4) and observed the formation of a thick blue oxide layer (figure 6.1(c)), realising that the plasma was highly contaminated in oxygen. For this reason, we started to use a spectrophotometer in order to acquire plasma emission spectrum and to check the presence of emission lines due to possible contaminants. Indeed, we realized that there was a leak in the helium gas line, as evidenced by the presence of the emission line of oxygen at 777.4 nm (figure 6.1(a)) and by a change in the color of the plasma (from pink to white-light blue) after the first minute from switching on. After cleaning the gas line and performing several conditioning of the chamber, we managed to have a cleaner He plasma, as the oxygen line was absent in the spectrum. Nevertheless, we later encountered an additional

problem with the oven installed in the plasma chamber of CAMITER. In order to create He bubbles we must reach temperatures <1000 K and high ion fluences which, in our set-up, correspond to exposure times of many hours. A first plasma test in which we programmed the heating ramp up to 1073 K was not successful, since we did not manage to reach the desired temperature and an air leak in the CAMITER plasma chamber occurred, probably caused by a malfunctioning of the oven. Since the use of the high power laser for such long exposure times is not easy to handle and could raise safety concerns, we decided to install the ellipsometry set-up in the plasma chamber PHISIS, in PIIM laboratory, in which we can generate RF plasma with the same principle of CAMITER (a planar coil antenna connected to a RF power generator and a capacitive matching box).

In the PHISIS set-up, the sample is heated by a resistive heater embedded inside the sample holder and the temperature is measured through a thermocouple placed on the backside of the sample holder. A new calibration of the ellipsometer was realized with a sample of 25 nm SiO_2 layer on Si, and the system measured an incident angle of 58°. Each sample is installed once at a time in PHISIS, where it is fixed inside a molybdenum mask. Before the exposure, we heat the sample up to the desired temperature and wait for it to be stable. We then introduce a specific gas pressure and send a specific RF power, in order to have the desired value of He flux (based on previous plasma characterization of this set-up via a Langmuir probe). For all the samples (with the exception of GFW4), the ion flux was 2×10^{19} He^+/m^2s (obtained introducing a gas pressure of 2 Pa and a RF power of 400 W). Once the plasma is on, we bias the sample holder by applying a negative voltage of -75 V (which, as the plasma potential is around 5 eV, results in an ion energy of $\simeq$80 eV). The exposure time is either 8 hours (with the exception of GFW4), in order to reach systematically a fixed fluence of $5.8 \times 10^{23} He^+/m^2$. During the exposure time, the temperature of the sample stays constant.

Samples	**Temp.(K)**	**Ion flux** (He^+/m^2s)	**Ion fluence** (He^+/m^2)	**Ion energy (eV)**	**Surface state**
GFW1	673	2×10^{19}			P
GFW2	823	2×10^{19}			P
GFW3	973	2×10^{19}	5.8×10^{23}	80	P
GFW4	973	4×10^{19}			P
GFW5	973	2×10^{19}			P+R

Table 6.1: Table resuming the experimental parameters of the He plasma exposure and previous W surface state of the samples. "P" is for "polished" and "R" is for recrystallized.

Three parameters were changed independently in the different plasma exposure: the surface temperature, the ion flux and the initial surface state. Table 6.1 resumes the characteristics of each sample and of its He plasma exposure. Three of the five samples (GFW1, GFW2 and GFW3) are exposed to three different temperatures (673, 823 and 973 K, respectively), while the other parameters are identical. Another sample (GFW4) is exposed at 973 K, but using an higher flux ($4 \times 10^{19} He^+/m^2s$) during 4 hours, in order to reach the same fluence. Finally the last sample (GFW5) is exposed at 973 K, with the only difference from the others that it was recrystallized (at 2073

K for 5 minutes, with an high power laser) after the electro-polishing process.

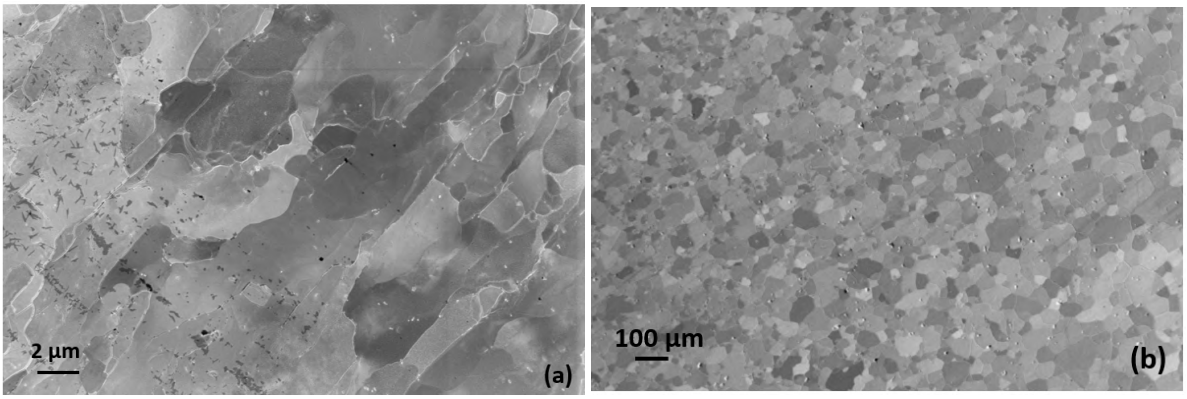


Figure 6.2: SEM images (secondary electron mode) of the samples GFW2 (a) and GFW5 (b), before He plasma exposure.

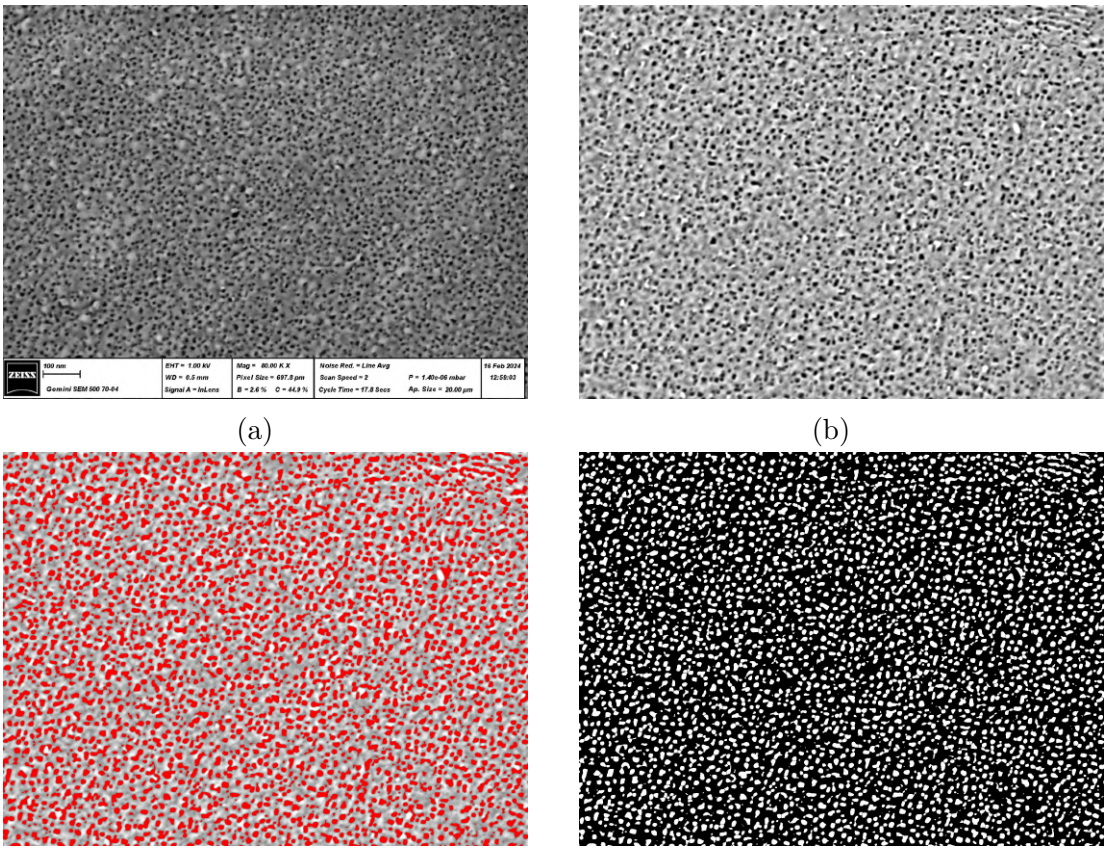
The surface of the samples is analyzed before the plasma exposure using Confocal Microscopy (CM), Atomic Force Microscopy (AFM) and Scanning Electron Microscopy (SEM). Figure 6.2 shows the SEM images of two samples before plasma exposure. For the non recrystallized sample (figure 6.2(a)), we observe crystal grains with average size of around 1-5 µm. For the recrystallized sample (figure 6.2(b)), grains dimensions have an unhomogeneous distribution, going from 30-60 µm (the majority of them) to bigger grains, of 100-200 µm, in proximity of the laser spot ($\simeq$2 mm).

6.2 *Ex-situ* microscopy study on He bubbles size and density

6.2.1 SEM images treatment for He bubbles characterization

The software ImageJ is used to process SEM images of the He exposed samples, in order to obtain the average size of He bubbles and their density distribution. We use a procedure that was already applied in previous studies on He bubbles [49]. The following routine is applied to every image:

- Set scale, associating the unit length to the measured pixel size (information contained in the SEM image, as in figure 6.3(a)).
- Apply FFT band pass filter: this step automatically adjusts the brightness and contrast, and it is done to enhance the contrast between the bubbles and the background (figure 6.3(b)). In our case, the band pass is set as the expected range of our particles size (for example, for samples with the biggest bubbles, we set this interval to 3-50 nm).
- Adjust threshold: a threshold of grey value is chosen manually, after which the software separates the bubbles from the background and the image becomes binary. This is the most delicate and user-dependent step, as different threshold values can be suitable to the image. In general, to attempt to make this step as rigorous as possible, we took the size of a few particles for every image before



(a) (b)

(c) (d)

Figure 6.3: ImageJ analysis routine of a SEM image: raw image (a), after applying FFT band pass filter (b), after applying the threshold (c), after applying the watershed routine on the binary image (d).

applying the threshold, then chose a threshold value which could retrieve an accurate separation of the bubbles and at the same time a particle size not to far from the measured value. The resulting image after applying the threshold is visible in figure 6.3(c).

- Apply the Watershed routine, to separate two or more fused particles that the software recognizes as one (figure 6.3(d)).

- Analyze particles, excluding the ones which are crossing edges of the image. The results of this step are summarized in a .csv file and include the requested quantities (area, major and minor radius, aspect ratio, circularity, etc.) for each particle.

- As most of our bubbles have shapes different from an ideal circle, we take as particle size the average between major and minor radius. We then apply some filters to these values, taking into account only the particles with aspect ratio <2.5 (in order to remove the too elongated bubbles) and with average size>2 nm (in order to remove the too small bubbles, which constitute a background noise).

- An histogram of the particles density is obtained and fitted with a Gaussian distribution.

We take as average bubbles size and its associated error the mean and standard deviation of the Gaussian distribution, and as bubbles density the integral of the Gaussian distribution divided by the surface of the image. Since the choice of the threshold can lead either to an underestimation or an overestimation of the bubbles size, we associate to the measured values an error of the 10% (Alfazzaa et al., submitted to JNME in July 2024).

6.2.2 Impact of temperature

SEM measurements of the samples GFW1, GFW2 and GFW3 (exposed respectively at 673 K, 823 K and 973 K) show that, as expected, the bubbles average size increases with increasing temperature. This is a direct consequences of the thermally-driven He bubbles coalescence process, resulting in bigger clusters which burst faster and more easily at the surface at higher temperatures.

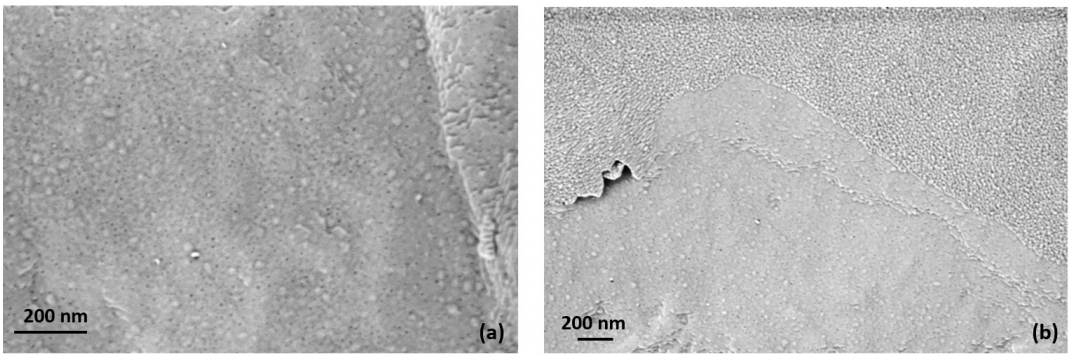


Figure 6.4: SEM images of the sample GFW1 exposed at 673 K on a smooth area of the surface (a) and at the border between a smooth and a rough area (b). We specify that in this case a statistical analysis was not possible, since the bubbles size was too close to the instrument resolution (1-2 nm).

For the sample GFW1, exposed at 673 K, He bubbles are hardly visible and especially on the smooth areas of the surface (figure 6.4(a)). The smooth and rough areas do not appear to have a different crystalline orientation in the EBSD map in figure 6.5, as they both correspond to the purple region which, according to the color scale, is oriented along a direction close to (111). Their size is around 1-5 nm (close to the detection limit of the instrument), with few bigger bubbles of about 9 nm, making it difficult to realise an accurate image treatment and statistical particle analysis.

For the sample GFW2, exposed at 823 K, the average size of He bubbles is around 10 nm (figure 6.6), changing slightly for the two different families of crystal grains that we observe. Finally, for the sample GFW3, exposed at 973 K, we observe bubbles with an average size of around 25 nm (figure 6.7). The SEM image in figure figure 6.7(a) represents a grain border between the two grains (111) and (100), where it is clearly visible that there is a dependence of bubbles size and/or distribution on the crystal orientation, as will be discussed in section 6.2.5. For the sample GFW3, the bubbles shape is not exactly circular but tends to be elongated and we observe a considerable

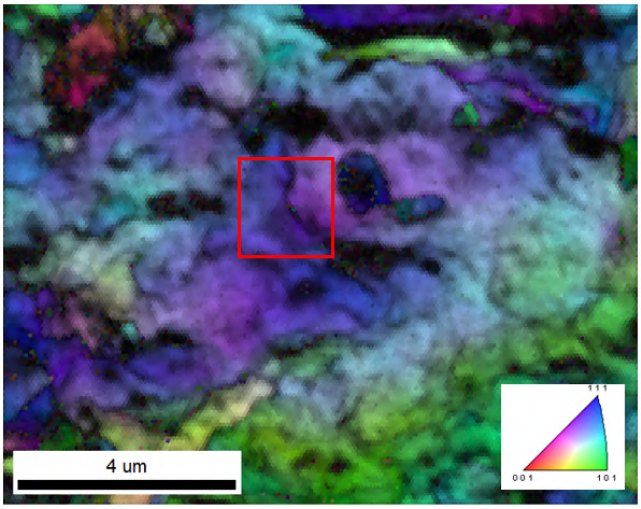


Figure 6.5: EBSD map of GFW1 surface, between a rough and a smooth surface (inside the red square), which do not show a specific difference in crystallographic direction.

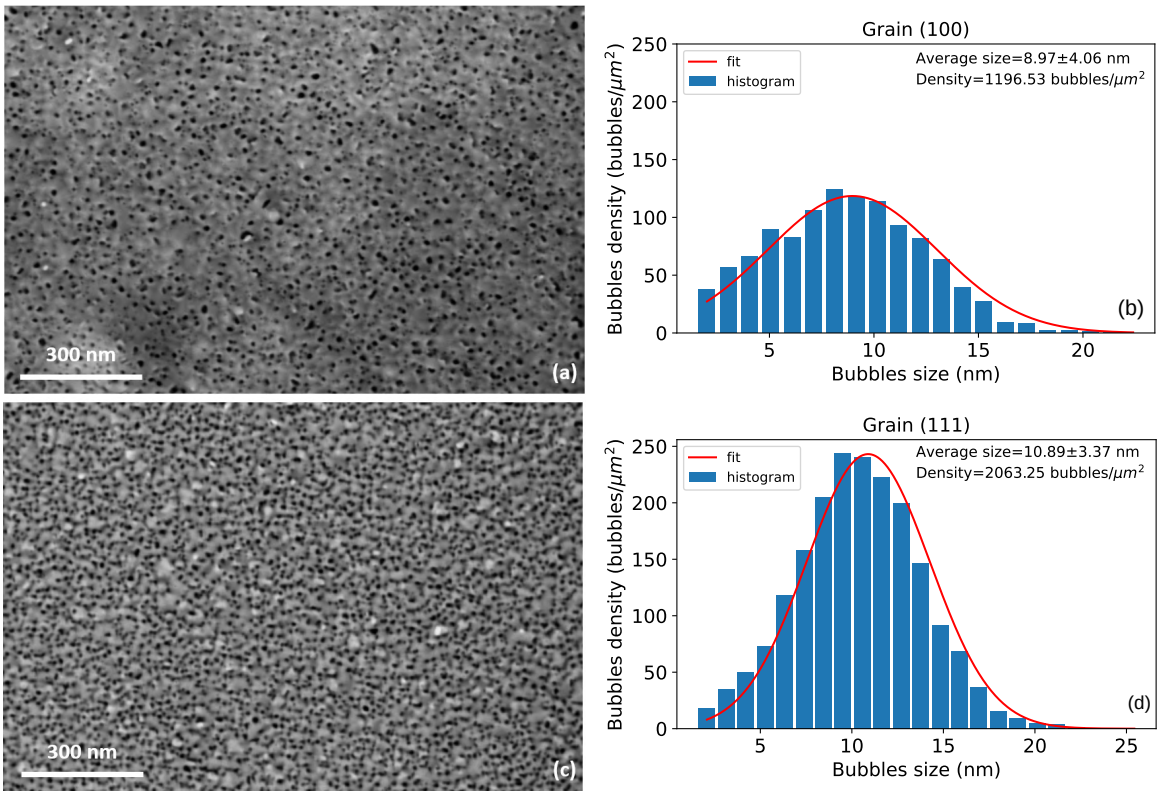


Figure 6.6: SEM images of the sample GFW2, exposed at 823 K, and relative statistics on He bubbles: grain (100) (a,b) and grain (111) (c,d).

number of agglomerates of 2 or more bubbles which probably burst together on the surface. This makes it hard to separate them as single bubbles in order to make a statistics on the size of each one and on their density, using the procedure described before, which was designed to count bubbles with an approximately circular shape. This results in a quite spread values distribution and a probable overestimation of

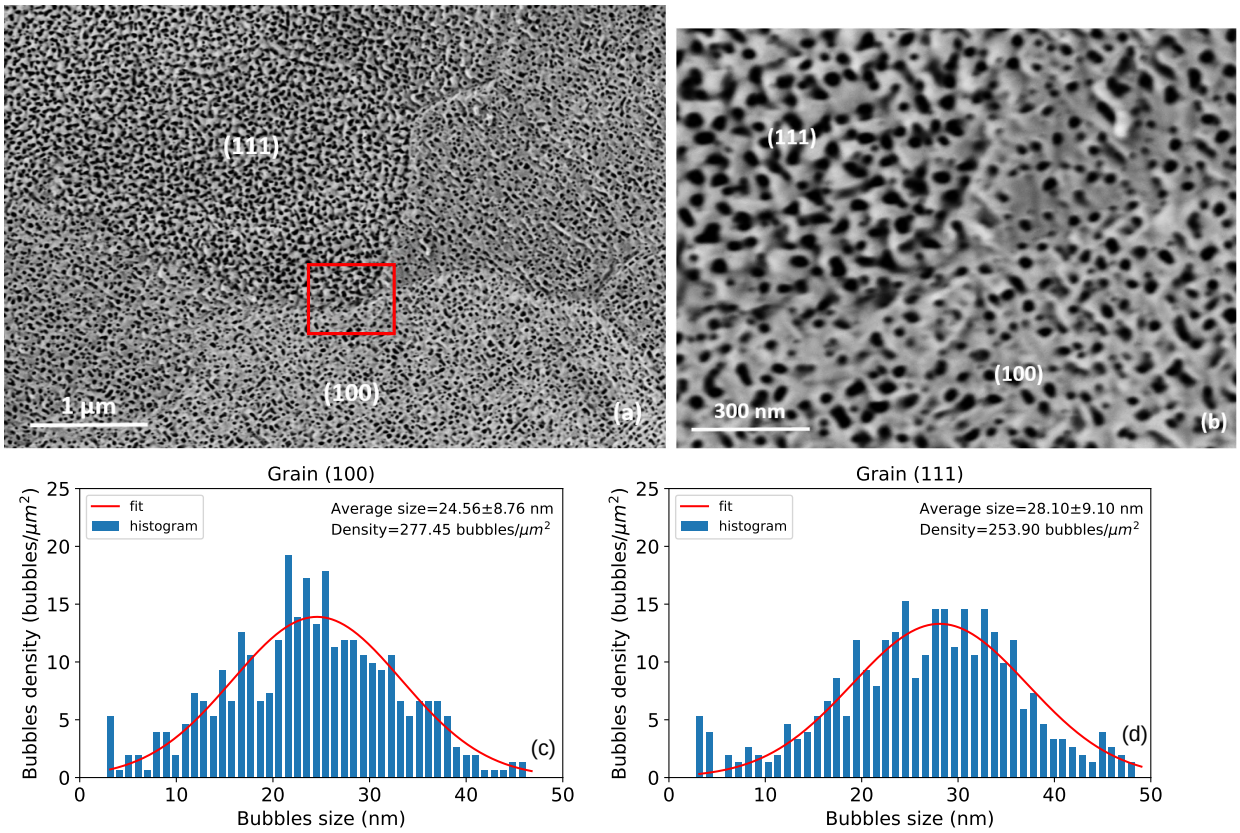


Figure 6.7: SEM images of the sample GFW3 (exposed at 973 K): at magnification 20k (a); of the area in the red square at magnification 80k (b). Relative statistics on He bubbles: grain (100) (c) and grain (111) (d).

the bubbles average size. Moreover, unlike the other samples, the average bubble size is bigger on grains (111) and the bubbles density is smaller as compared to the grain (100), whereas by naked eye it would seem that the bubbles are more densely distributed on the grain (111). This could be due to a failure of the image processing routine in separating the bubbles, which would probably lead to an overestimation on the bubbles size on the grain (111), resulting in a lower density.

6.2.3 Impact of ion flux

In order to test the role of ion flux on He bubbles formation, we expose the sample GFW4 to He plasma to an ion flux of $4\times10^{19} He^{+}/m^{2}s$, reached introducing a He pressure of 2 Pa and adjusting the RF power to 800 W. The exposure time is of 4 hours, in order to reach the same ion fluence of the other samples. It is important to specify that, even if it is higher only by a factor 2, it is obtained using the maximum value of RF power that our experimental set-up can maintain for such long exposure times.

The SEM images of the surface after exposure show a similar morphology of He bubbles as compared to the sample GFW3, with a predominance of groups of agglomerated bubbles. The average size in this case is around 20 nm, slightly smaller compared to the bubbles on the surface of the sample GFW3. This could be due to a lower exposure time (4 hours instead of 8), even if the ion flux was higher by a factor

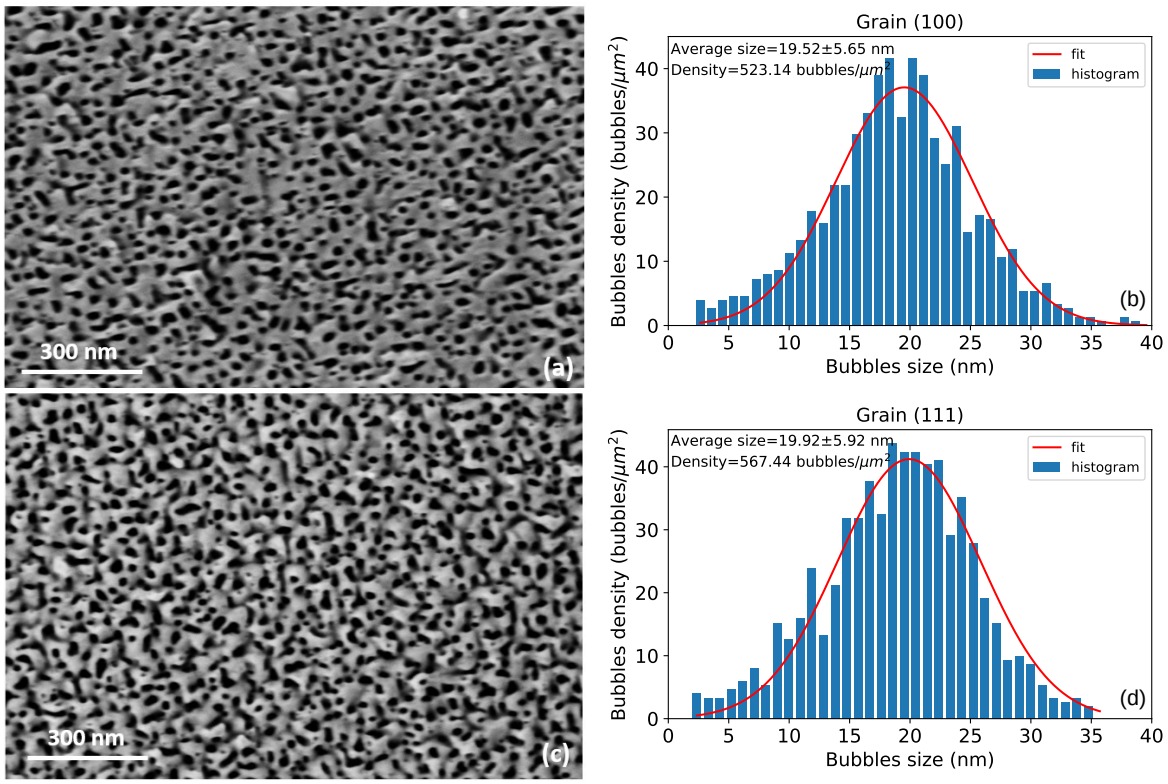


Figure 6.8: SEM images of the sample GFW4, exposed at 973 K and higher flux, and relative statistics on He bubbles: grain (100) (a,b) and grain (111) (c,d).

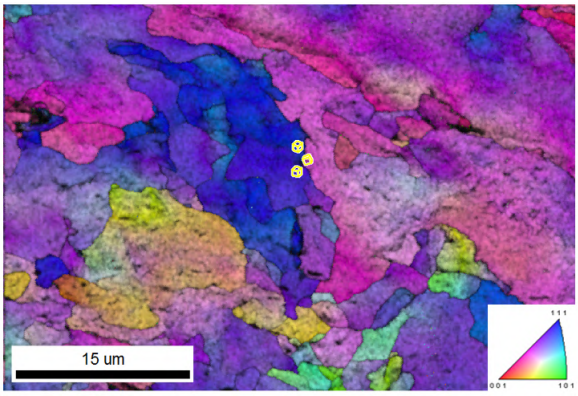


Figure 6.9: EBSD map of the exposed sample GFW4, with marks on the area between the two grains, where the SEM images in figure 6.8 was taken.

2 in order to reach the same ion fluence. In comparing the He bubbles on the two samples, however, another remark must be done. Unlike sample GFW3, there seems not to be a considerable difference in the bubbles density between the grains (111) and (100). However, it is necessary to specify that, for this sample, EBSD measurements (in figure 6.9) did not show grains with a perfect (100) orientation, so the grain that we represent in figure 6.8(a) has rather an intermediate orientation between (111) and (100), resulting in a not so pronounced difference in bubbles density between the two areas investigated.

6.2.4 Impact of surface state

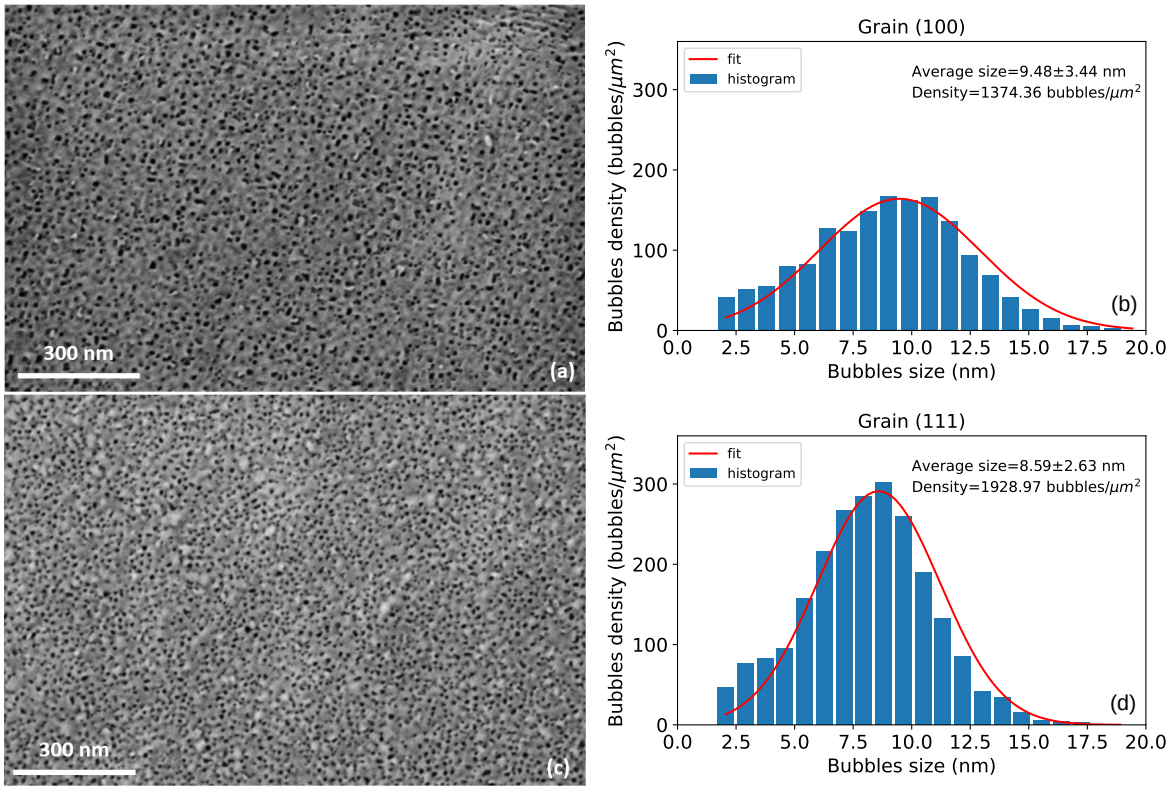


Figure 6.10: SEM images of the sample GFW5, recrystallized and exposed at 973 K, and relative statistics on He bubbles: grain (100) (a,b) and grain (111) (c,d).

Finally, we decided to expose the sample GFW5 to the exact same conditions as the sample GFW3 (same ion flux and energy, exposure time and temperature) but with a difference only in the initial surface state. The sample GFW5, in fact, was mechanically and electro-chemically polished like the other samples, and in addition it was recrystallized with an high power laser (at 2073 K for 5 minutes in high vacuum).

There is no doubt that the initial W surface state has an effect on He bubbles formation. Compared to the sample GFW3, exposed at the exact same conditions, the sample GFW5 shows smaller He bubbles, with an average size of about 10 nm (figure 6.10). Qualitatively, the bubbles size and density are comparable to the ones of the sample GFW2, exposed at 823 K, suggesting that the recrystallized surface, consisting in bigger crystal grains, hence less grain boundaries acting as nucleation and diffusion sites, could have the effect of slowing down the bubbles growth, similar to a situation in which the temperature is lower.

6.2.5 Impact of grain orientation

A common feature of all samples was the difference in He bubbles density depending on the crystalline grain orientation. EBSD measurements, performed along with SEM, evidenced mainly two families of crystal grains, namely the ones oriented along the (111) direction and the ones oriented along the (100) direction. It can be noticed also the presence of a considerable amount of crystal grains with an orientation intermediate

between the two (as visible in figure 6.9). While the crystal orientation does not seem to have an effect on the average bubbles size (or at least, the value remains in the error bar), we observe for every sample an higher bubbles density on the crystal grains oriented along (111) axes with respect to the ones on grains (100). The only exceptions were the sample GFW1, in which it was hardly possible to detect He bubbles in the first place, and the ones we observed where mainly on the less rough areas of the surface (which did not correspond to any specific crystal orientation), and the sample GFW3, for which we observed the opposite behaviour (probably due to the image processing routine, as discussed in section 6.2.2). It is not straightforward to explain the reason of the different density along different crystal orientations based only on the empirical results. Previous molecular dynamics (MD) simulations [136] showed that the displacement energy threshold of He on W depends on the crystal orientation, in particular it is minimum along the (100) direction ($\simeq$68 eV) and maximum for (111) direction ($\simeq$250 eV), suggesting that there would be more bubbles burst on the surface of (100) grains, contrary to what we observe. It is also important to specify that in our study the number of analyzed grains is relatively small to perform statistics and draw solid conclusions, and that additionally studies focused on this topic are needed in order to gain more insight on the bubbles density dependence from the grain orientation.

In conclusions, with *ex-situ* microscopy of the exposed samples we have observed the following features:

- a dependence of He bubbles density from the W crystalline orientation, with systematically bigger values relative to the (111) grains as compared to the (100) ones. We specify that only a few (010) grains were observed, only on a few samples, and the behaviour of the bubbles density on their direction resembled the one on grains (111).

- a dependence of He bubbles size from temperature (from 1-5 nm at 673 K to 20-25 nm at 973 K). We must specifiy, however, that when the bubbles size becomes too big (as for samples GFW3 and GFW4) we start to observe agglomerates of He bubbles that burst together on the surface, hence it is difficult to determinate accurately their average size from SEM images with the procedure previously described.

- an increase by a factor 2 of the ion flux does not change much the He bubbles size or density. They appear slightly smaller as compared to the sample GFW3 exposed at lower flux, possibly due to the lower exposure time (4 hours instead of 8). However, as specified above, we may overestimate the size of the bubbles on sample GFW3 due to their high tendency to agglomerate.

- a dependence of He bubbles size from the initial surface state, in particular for the recrystallized sample GFW5 the bubbles are smaller ($\simeq$10 nm) as compared to non recrystallized sample GFW3 exposed at the same conditions ($\simeq$25 nm), confirming the results of Alfazzaa et al performed on recrystallized samples. This suggests that the temperature is not the only determining factor in the He bubbles formation.

6.3 Optical measurements

6.3.1 Reflectivity variation of the He exposed samples

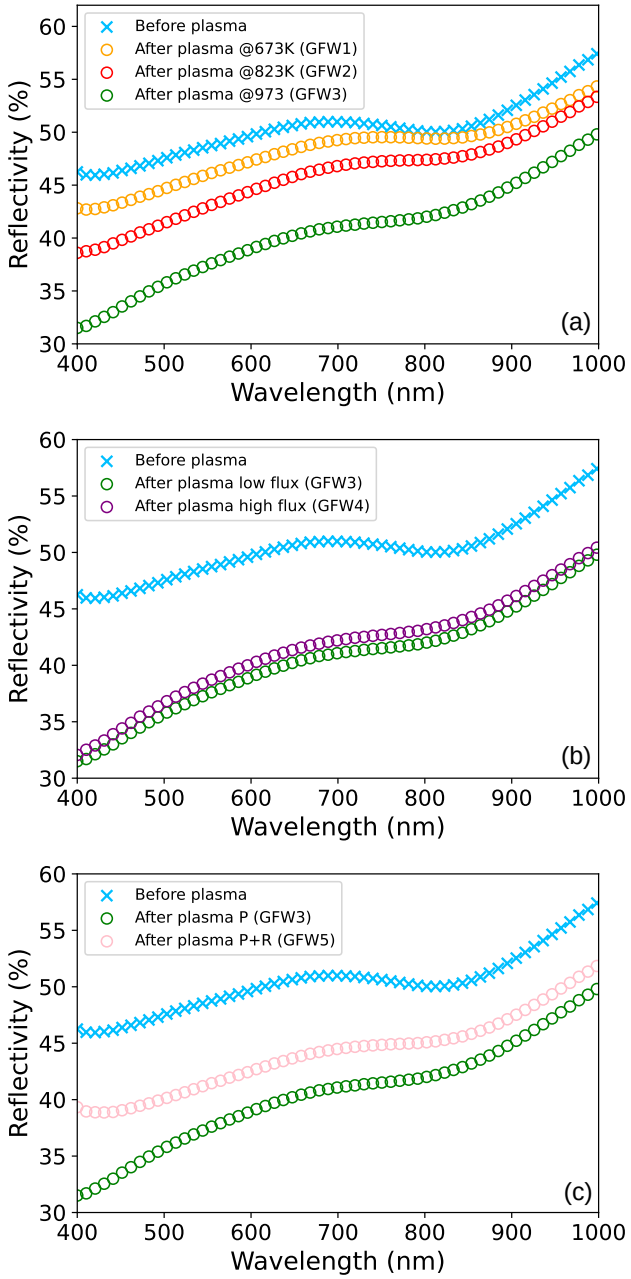


Figure 6.11: Comparison of the reflectivity spectra of W samples before plasma exposure and: the samples GFW1, GFW2 and GFW3 exposed at 673 K, 823 K and 973 K, respectively (a); the sample GFW4 exposed at 973 K to an ion flux higher by a factor 2 (b); of GFW5, exposed at 973 K and previously recrystallized (c).

As specified at the beginning of this chapter, in parallel to the morphology analysis with *ex-situ* electron microscopy, *in-situ* ellipsometric measurements were realized during the exposure.

From the measured Ψ and Δ, we calculated directly the reflectivity, using the

model for bulk W material described in section 2.2.1. A first, immediate information that we can retrieve from the optical measurements is that for every sample there is a decrease in reflectivity after He plasma exposure. Figure 6.11 shows such variation as a function of temperature, ion flux and surface state. In particular, we can observe a bigger decrease of reflectivity with increasing temperature, going from 1% (absolute variation at 550 nm) for the sample GFW1 exposed at 673 K, to around 4% for the sample GFW2 exposed at 823 K and finally 14% for the sample GFW3 exposed at 973 K (figure 6.11(a)). Increasing the ion flux by a factor 2 does not change considerably the reflectivity (figure 6.11(b)), while the previous surface recrystallization determines a lower reflectivity variation as compared to the same exposure performed on a non recrystallized surface (figure 6.11(c)). All these results are coherent with the information retrieved with SEM analysis, i.e. the reflectivity is inversely proportional to the He bubbles size.

6.3.2 Temporal evolution of porosity and surface roughness

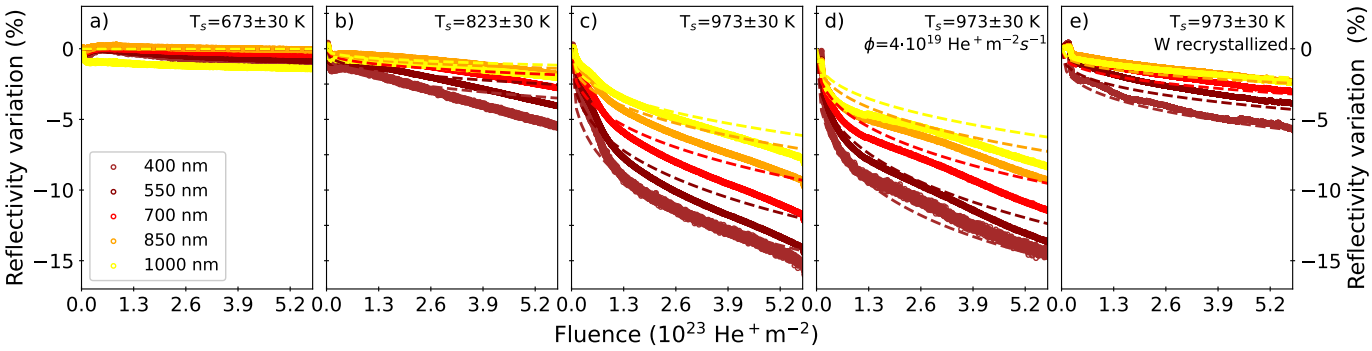


Figure 6.12: Reflectivity variation calculated from the *in-situ* ellipsometric data during He plasma exposure for the sample GFW1 (a), GFW2 (b), GFW3 (c), GFW4 (d) and GFW5 (e), considering an error bar on temperature values of ±30 K. The solid lines refer to the experimental data at different wavelengths, while the dashed lines refer to the correspondent model.

The second aim of the present study is to use *in-situ* ellipsometry to monitor the kinetics of He bubbles formation. Figure 6.12 represents the reflectivity variation calculated from the *in-situ* data during He plasma exposure. The solid lines refer to the experimental data for 5 wavelengths in the measured range, while the dashed lines refer to the fit by the EMA model (described in section 2.2.4). The same features that we highlighted in the section above can be observed even more immediately in the experimental *in-situ* data, where we clearly see the variation of reflectivity increasing with temperature, from sample GFW1 to sample GFW3 (figure 6.12 (a) to (c)), remaining almost unchanged increasing the flux for sample GFW4 (figure 6.12 (d)) and changing significantly for the recrystallized sample GFW5 (figure 6.12 (e)). Moreover, we can observe that the reflectivity variation reaches bigger values at shorter wavelengths (for which the diffused component is more important) and that only for the sample GFW2 (exposed at 823 K) the trend of the *in-situ* data is linear with time.

Afterwards, we fit the optical data using the effective medium approximation (EMA) model, already described in section 2.2.4, which considers the He exposed surface layer as a porous layer in which two material phases, with known dielectric constants, coexist. The host material is assumed to be W, with optical constants directly calculated from an *ex-situ* measurement of Ψ and Δ before the exposure. The material of the inclusions (bubbles) is He, which has a dielectric function similar to the one of air ($\epsilon_{He} = 1$) in a wide range of temperature and pressure [137, 138]. The thickness of the porous layer is constrained to 25±10 nm (from previous TEM observations of He bubbles layer in similar exposure conditions [16]). In addition, we take into account also the surface roughness, using the Bennet-Porteus model already described in section 2.2.3. The time-dependent parameters of the fit are then the porosity (He bubbles volume fraction) and the surface roughness.

To fit the *in-situ* data, we assume a dependency of porosity and roughness from time and temperature. The porosity corresponds to the volume fraction occupied by the He bubbles in the EMA layer. We assume that the bubbles growth takes place in 3D with a temporal dependence of 1/3 and is thermally activated, with an exponential dependence from the temperature and a specific binding energy associated to the process of a bubble formation (in which an He cluster binds to a vacancy). The evolution of porosity with time and temperature is described by the following equation:

$$\delta(t,T) = \delta_0 + A \cdot \left(\frac{t}{t_{end}}\right)^{1/3} \cdot \exp\left(-E_b/k_bT\right) \tag{6.1}$$

assuming that δ_0=0 (no bubbles before exposure), t_{end}=480 min. corresponds to the end of plasma exposure and A is a multiplicative dimensionless constant which does not depend on temperature.

Because the growth of He bubbles, with consequent release of local stress and rupture to holes on the surface, is a temperature driven process, we can assume that also the evolution of surface roughness follows a similar law:

$$\sigma(t,T) = \sigma_0 + B \cdot \left(\frac{t}{t_{end}}\right)^{1/3} \cdot \exp\left(-E_b/k_bT\right) \tag{6.2}$$

where σ_0 is the roughness before exposure and B is a multiplicative factor in nm which does not depend on temperature. While σ_0 value is taken from roughness measurement, the constants A and B are free parameters adjusted manually to retrieve a good fit of the experimental data (values are shown in the table 6.2). The binding energy values of He bubbles were constrained according to previous *ab-initio* simulations of He bubbles growth and coalescence [29], which are in the range 1-2 eV (depending on the number of He atoms in the bubble), hence we found the best fit using the average of such values (1.2 eV). For the recrystallized sample GFW5, we suppose that the binding energy is higher (1.3 eV), as the presence of less defects on the surface and a bigger size of the crystal grains should inhibit and slow down the bubbles growth, resulting in an higher energy required to form He-vacancy clusters.

The fit seems to be in good qualitative agreement with the experimental data for all the exposed samples, especially for the shorter wavelengths, for which the diffused component of reflectivity is more important and which should be more influenced by roughness variation. It has to be remarked that we were not able to obtain a good fit of the samples exposed at 823 K (GFW2) and at 973 K (GFW3, GFW4 and GFW5) with

the same binding energy values, unless we suppose that the exposure temperature of GFW2 is higher than 823 K by at least 70 K. It would seem here either that the model predicts an activation temperature of the He bubbles formation process between 823 K and 890 K (which is not true, since we observe experimentally He bubbles on GFW2 surface with SEM), or that the temperature dependence is actually more complex than the Arrhenius exponential that we assumed. Another explanation could be the error on the temperature measurement made by the thermocouple, which is supposed from previous calibrations [54] to be around ±30 K, due to the uncertainty of the thermal contact between the sample and the sample holder. Considering the error bar on the temperature values, we manage to retrieve a better fit of the experimental data (figure 6.12), using a binding energy of 1.2 eV for the non recrystallized samples exposed at temperatures 673 K (GFW1), 823 K (GFW2) and 973 K (GFW3, GFW4) and of 1.3 eV for the recrystallized sample exposed at temperature 973 K (GFW5).

	E_b **(eV)**	**A (adim.)**	**B (nm)**	σ_0 **(nm)**
Non recr. samples (from GFW1 to GFW4)	1.2	8×10^5	4.3×10^7	15
Recryst. sample (GFW5)	1.3	1.5×10^6	4.5×10^7	15

Table 6.2: Table representing the parameters of the model used to fit the *in-situ* reflectivity data.

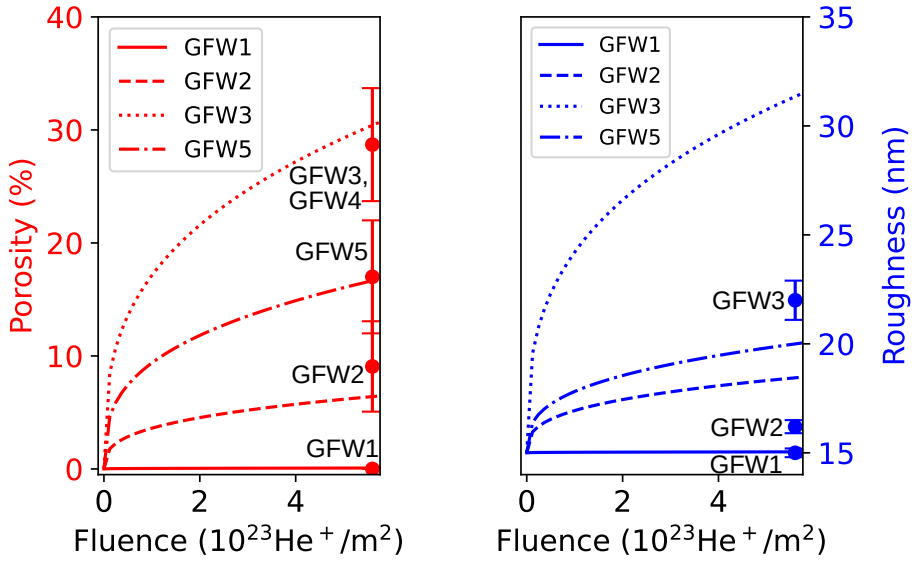


Figure 6.13: Variation of porosity (a) and roughness (b) as a function of He fluence, for the samples GFW1, GFW2, GFW3 and GFW5. The points correspond to the experimental values of porosity (extracted by SEM images) and roughness (measured with AFM), and their correspondent error bars.

We then compared the values of porosity and roughness retrieved from the model with the experimental values obtained by the *ex-situ* characterization of the exposed samples (figure 6.13). We observe a quite good agreement for the porosity of the samples exposed at different temperatures, while we see that the model tends to

overestimate the roughness. However, two aspects must be underlined in this case. Regarding the porosity, the experimental values that we take from the SEM images correspond only to the surface coverage of the burst He bubbles, or, in other words, the percentage of holes on the exposed surface. Hence, we assume that the bubbles fraction is homogeneous throughout the whole layer volume and take this value as upper limit for the porosity of the overall layer. In figure 6.13, we plot the porosity of the samples GFW1, GFW2 and GFW3 (exposed at 673, 823 and 973 K) and the correspondent experimental points of the exposed surfaces, extracted from SEM images. Since the ImageJ process to obtain the porosity parameter sensibly depends on the used threshold, each point corresponds to an average of three values, extracted fixing an upper and lower limit of the selected threshold, and the error bar corresponds to their standard deviation. In particular, for the temperature 973 K, the experimental point of porosity is taken as the average of the images of the exposed samples GFW3 and GFW4. Regarding the surface roughness, both Confocal Microscopy and AFM were used to characterize the surface morphology before and after the exposure. Both measurements showed no visible roughness variation before and after the exposure. An explanation could be that the resolution of the two techniques is not high enough to detect the increase of roughness cause by the He bubbles burst on the surface (measured as holes). The lateral resolution, in fact, is of 130 nm for the used magnification of CM (100x), and of 10 nm for AFM (tip radius size). Only with an additional step in the image treatment, in which a 0.2 µm low-pass filter is applied in order to separate a roughness profile from the waviness profile, AFM showed a small increase of roughness with exposure temperature. We then plot in figure 6.13(b) as experimental points the roughness values measured with AFM of the exposed samples GFW1, GFW2 and GFW3 (with an error bar of 20%). This may be explained by two main reasons: either we are underestimating the bubbles volume fraction over the porous layer, or our model is not complete, hence we are neglecting some other effect, which is not roughness, which would be responsible for the consistent reflectivity variation that we observe during the exposure.

6.4 Conclusions and perspectives

In this study, we have performed *in-situ* ellipsometric measurements on several W samples during He plasma exposure, in order to monitor the He bubbles formation and the roughness evolution. At the same time, we have conducted a microscopy analysis in order to investigate the He bubbles size and density as a function of different parameters (temperature, ion flux, surface state). Such microscopy analysis, realized with SEM, showed an increasing bubbles average size with temperature (from 1-5 nm at 673 K to 20-25 nm at 973 K), with the tendency to burst as agglomerates of two or more bubbles at the highest temperature. No substantial difference in the bubbles morphology was observed for the sample exposed at 973 K to flux higher by a factor 2 (GFW4), while the bubbles size on the recrystallized sample (GFW5) was of the same order as the sample exposed at 823 K (GFW2), suggesting that the previous recrystallization of the surface could slow down the bubbles growth, having a similar effect as a lower temperature. Furthermore, in all the exposed samples, SEM measurements showed a higher bubbles density in (111) crystal grains with respect to (100). The optical measurements performed in parallel reveled to be coherent with

the SEM analysis. Experimentally, we have observed a decrease in reflectivity for all the exposed samples. The reflectivity decrease is more important for higher exposure temperatures, does not change much at higher flux and is for sure influenced by the surface state of W (being lower for the recrystallized sample GFW5, with respect to GFW3, not recrystallized and exposed at the same conditions).

We then focused on the *in-situ* optical measurements, in order to try to reconstruct the kinetics of He bubbles formation during the plasma exposure. For this purpose, we have used a model of a porous layer (EMA) with roughness (both specular and diffused components) to fit the *in-situ* optical data, predicting an evolution of porosity (He bubbles percentage) and surface roughness that has a time dependence of a power law of 1/3 and an exponential dependence on temperature, and in which also the activation energy of the process (binding energy of an He clusters to a vacancy) has a crucial role. Such model retrieves a good qualitative fit of the experimental data, using E_b=1.2 eV for all the samples (except for the recrystallized GFW5, for which we used E_b=1.3 eV) and assuming an error of $\pm$30 K on temperature values. Secondly, we compare the porosity and the roughness obtained from the model with the experimental values (for the porosity, the percentage of bubbles surface coverage in SEM images, and for roughness the values measured by AFM). We observe a quite good agreement for the porosity of the samples exposed at different temperatures, while we see that the model tends to overestimate the roughness. This could be due either to an incompleteness of our model, who does not necessarily take into account all the processes (and relative activation energies) contributing to bubbles formation (He clustering+bubbles formation+bubbles diffusion), or to a possible limitation of the experimental techniques used to measure roughness.

The results discussed here constitute a first attempt of using *in-situ* ellipsometry as a feasible and advantageous diagnostics to monitor He bubbles growth. However, many things are missing in order to have deeper insight: first of all, a more complex model taking into account the single processes contributing in the bubbles formation and second order effects (i.e., dissociation of He bubbles, interaction with W interstitials); secondly, a deeper investigation on the reason of the higher bubbles density in the (111) crystal grains, using He bubbles growth simulations with macroscopic rate equation models; in addition, enrich our experimental characterization by performing TEM measurements of the exposed samples, in order to observe the thickness of the porous layer and the actual volume fraction of He bubbles; finally, performing roughness measurements with SEM, introducing a tilt which would allow to obtain a height map, in order to measure roughness variations at the nanometric scale.

Chapter 7

Conclusions

7.1 Summary

In this PhD thesis, we performed laboratory experiments involving plasma exposure and optical diagnostics, with the aim of exploring the fundamental interactions between ions (D, He) and W surface. Post-exposure characterizations are also realized to assess any change in the surface morphology and chemical composition. In particular, we attempt to reproduce, in the limits of our experimental set-ups, the typical conditions of ITER divertor, where W PFCs are subjected to low energy (<50eV), high particles fluxes and high temperatures (<1000 K). The interest on PFCs optical properties originates from the use of non contact diagnostics for the protection and operation of the machine (mostly pyrometers and cameras, working in the visible and IR range), where any surface state variation due to the tokamak harsh environment causes inevitably variations in the PFCs optical properties (reflectivity, emissivity). In addition, there is a growing necessity to develop non invasive and non destructive techniques which are also able to serve as *in-situ* and real time diagnostics during plasma operation, without the need to conduct post-mortem, possibly destructive analysis.

We will briefly go again through the accomplishments of this study and finally outline some perspective for future works.

In chapter 3, we conducted a parametric study of W reflectivity as a function of roughness and temperature. Since it was intended as a preliminary work previous to proper plasma exposure, we decided to control the roughness variation by chemical etching, in order to simulate the roughness increase effect of He irradiation on W. Then, we measured the reflectivity variation as a function of temperature in the range 300-1000 K during multiple annealing cycles, for different samples with increasing roughness in the range 20-100 nm. In addition, *ex-situ* microscopy techniques (CM, AFM) were used to measure the roughness before and after the annealing cycles. We looked at the reflectivity before and after the annealing cycles and found a relative increase by 5-10%. We fitted the experimental data with the Bennet-Porteus model, which predicts the behaviour of reflectivity as a function of wavelength and roughness, including the contribution of both specular and diffused components, but works only in the limit where $\sigma << \lambda$. Hence, we found a bigger discrepancy in the reflectivity spectral behaviour for the rougher samples, where roughness starts to become of the same order of the used wavelength and more complex models are required. Since the

microscopy techniques did not evidence any roughness variation before and after the annealing, we used XPS technique to detect any change in the surface composition. Indeed, the XPS of the samples post-annealing showed a considerable decrease of contaminants (K and N, coming from the etching solution) and a consistent reduction of the native oxide, visible by the predominance of W 4f metallic peaks. Hence, we explain the reflectivity increase as a consequence of the surface cleaning caused by the annealing, and conclude that roughness variation as little effect in the change of reflectivity in this temperature range.

In chapter 4, we performed the first *in-situ* ellipsometry measurements on W exposed to D plasma, in order to better train on the technique and to prepare for more harsh exposures (He plasma), as we realize exposure conditions in which D ions are not expected to induce a big change in W morphology. Here, we found a relative increase of W reflectivity during D plasma of around 3.5% at 850 nm. Since W surface temperature, monitored at the same time with a pyrometer, increased up to 600 K because of the plasma, following the same trend of the optical signal, we performed some calibrations in order to quantify the temperature and the D ions contributions to the total reflectivity variation during plasma. We then used ellipsometry to measure the reflectivity variation during annealing, either with an oven or with an high power laser, and subtracted the temperature contribution to the reflectivity variation observed during plasma, assuming that the result of this subtraction is the effect of D ions in the change of reflectivity (hence, assuming that the two effects sum up). Looking at the reflectivity variation as a function of wavelength, we observed that it is maximum at 850 nm just like the temperature contribution, suggesting that the two effects have the same nature, in particular they change the phonon-electron interactions contributing to change W dielectric function. We also looked at the same reflectivity variation as a function of temperature during plasma exposure. Here, we observe a fast growth in the first minute of the exposure, when it reaches a maximum at 410 K. Afterwards, the D ions effect decreases and it is counterbalanced by the temperature rise. In order to gain more insight on the absorption and desorption of D atoms on the surface, we used the code MHIMS to model the D inventory (concentration of D atoms retained in the material) during the plasma exposure. To be able to compare such results with the ellipsometric data, which depend on the light absorption properties of the specific material, we modelled the D surface inventory, i.e. the concentration of D atoms retained in the first 23 nm from the surface (penetration depth at the first order of 850 nm light in W). Here, we observed a quite good agreement between the model and the ellipsometric data, as the D surface inventory is maximum in the first minute of the plasma exposure (at 410 K) after which it decreases for a combined effect of thermally-induced desorption and bulk diffusion of D atoms.

In chapter 5, we spent some time on the synthesis and characterization of thick (>50 nm) W oxide layers thermally grown on W substrates. As the presence of oxide layers raises issues on the lifetime of PFCs inside the tokamak and on a possible contamination of the plasma, we use *in-situ* ellipsometry during D plasma exposure coupled to *ex-situ* characterizations to assess any change in the oxide surface state caused by the D plasma irradiation. The optical measurements evidenced a substan-

tial change of the optical constants n and k of the oxide, which after exposure take values typical of a metallic surface. This suggested a general reduction of W oxides by D ions, which was also confirmed by *ex-situ* techniques (FIB-SEM) and which we attribute to a chemical sputtering process, since we perform exposure at ion energies of around 15 eV (far below the sputtering threshold). Furthermore, the oxide reduction is a thermally enhanced process, clearly visible from FIB-SEM measurements only in case of oxides irradiated at high temperatures (600 K). For oxides irradiated with D plasma at low temperature (373 K), FIB-SEM did not detect any change in the oxide morphology, while both ellipsometry and XPS showed the typical features of an oxide reduction process, respectively an increase in the extinction coefficient k and a predominance of metallic W 4f peaks over the oxide ones, suggesting that such changes occur in the near-surface layer ($\simeq$5 nm) which is close to the resolution of FIB-SEM. We concluded then that the temperature has en effect on the extension in depth of the oxide reduction, and that *in-situ* ellipsometry can be a useful tool to detect it even when it is below the resolution of *ex-situ* microscopy techniques such as FIB-SEM.

In chapter 6, we finally performed *in-situ* ellipsometry measurements of W during He plasma exposure, in conditions similar to the harsh environment of the tokamak divertor, in which we expect a consistent change of W surface morphology because of He induced damage (in particular, at temperatures <1000K, where we expect the formation of He bubbles). The aim was to use ellipsometry to investigate the kinetics of He bubbles formation and the evolution of surface roughness. Also in this case, *ex-situ* microscopy of the exposed samples is systematically coupled to the *in-situ* measurements. We performed He plasma exposures changing independently different parameters, namely the temperature, the ion flux and the initial W surface state. *In-situ* ellipsometry coupled with SEM measurements of the irradiated surfaces show a decrease of W reflectivity during He plasma exposure. In particular, such absolute decrease in reflectivity is higher with increasing temperature, going from 1% (for 550 nm light) at 673 K to 14% at 973 K, and also the He bubbles size follows this trend (going from 1-5 nm at 673 K to 20-25 nm at 973 K). Furthermore, increasing the ion flux of a factor 2 does not change much the reflectivity variation as well as the bubbles size. Finally, performing the exposure on a previously recrystallized W surface results in a lower decrease of reflectivity as well as smaller He bubbles. We model the *in-situ* data with a porous layer (EMA) representing the near-surface layer of the exposed samples containing He bubbles, considering also the surface roughness. We assume that the evolution of porosity (volume fraction of He bubbles over the porous layer) and of surface roughness depends on an Arrhenius law, hence it is thermally activated and the activation energy of the process correspond to the biding energy of He clusters to a vacancy (bubble formation). The model has a good qualitative agreement with the experimental data, using binding energy of 1.2 eV for all the samples (except the recrystallized one, for which we used a binding energy of 1.3 eV) and assuming an error of $\pm$30 K on the temperature values. We then compared the results of the fit with the experimental values of porosity and roughness, retrieved respectively from the analysis of the SEM images and from AFM measurements. While porosity values seem to have a good agreement with the experimental values, considered as upper limits for the porosity as they refer to the bubbles surface coverage, we find that we overestimate roughness. We then conclude with two possible explanations: either our model is not

complete, as it does not necessarily take into account all the processes (and relative activation energies) contributing to bubbles formation (He clustering+bubbles formation+bubbles diffusion), or our roughness measurements suffer from the resolution limitations of the experimental techniques.

7.2 Perspectives

The objective of this PhD work was to prove the advantage and feasibility of using non-contact, non-invasive optical diagnostics to study plasma-surface interactions, mostly for applications in the PFCs of tokamaks such as ITER. As the most used technique was ellipsometry, a few words should be said about the possibility to adapt such technique to a tokamak environment.

The use of *in situ* ellipsometry to follow the first wall erosion and co-deposition was tested in the tokamak TEXTOR in 2009 by Dittmar et al. [107]. In general, the issues which could derive by the use of ellipsometry as a real time diagnostics during plasma operation in a tokamak geometry are the following:

- the reflection geometry of conventional ellipsometry is difficult to realize in a toroidal plasma chamber
- the high magnetic fields present during operation can cause a change in the polarization of the ellipsometer light source
- in addition, the rotating elements such as polarizers and analyzers present in the ellipsometer source and detector units are not compatible with magnetic fields.

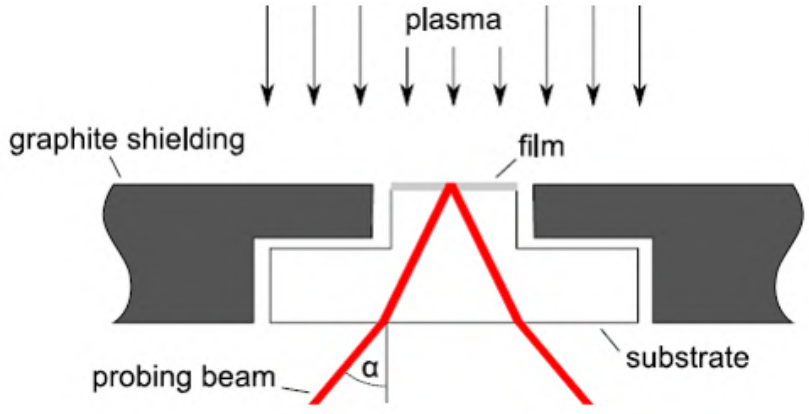


Figure 7.1: Reverse ellipsometric configuration implemented by Dittmar et al. [107] in TEXTOR.

Previous works such as [107] made an attempt to test the compatibility of ellipsometry to the tokamak environment, for example by realizing a reverse configuration (in which the ellipsometry light hits the PFC from the backside, passing through a transparent substrate) and isolating all the optical components of the ellipsometry set-up in an actively cooled and atmospheric pressure environment (in order to protect it from the magnetic fields and the heat loads). However, the quality of ellipsometry signal was inevitably influenced by the high thermal loads and the small angle of incidence

(which is a constraint of using a reverse geometry). It should be specified, however, that nowadays there should be specific available rotating components with a higher compatibility with ultra-high vacuum environment and relatively high magnetic fields, and therefore they could be, in principle, installed even inside the vacuum vessel of a fusion device.

Such results and the poor quantity of further experimental investigations are an evidence of how the adaptation of *in-situ* ellipsometry as a tokamak diagnostics constitutes a significant scientific challenge. Recent, breakthrough works [139] show the simplification of an *in situ* spectroscopic ellipsometer set-up, with the aim of conducting real time thickness monitoring in conditions of limited space such as fusion devices. The proposed set-up has been valitdated for calibration with SiO2 film and could work in a situation of relatively low radioactivity levels, which would allow layer measurements with a hand-held device between experimental campaigns. However, also in this case, further research are necessary on other materials (steel, tungsten, graphite) and conditions of higher radiation levels (which would imply either a hardening of the ellipsometry set-up or the possibility to use remote handling for the analysis). While further studies on possible optimizations of ellipsometry design are encouraged, we stress the relevance and the valuability of such diagnostics in a tokamak environment even for *ex situ* analysis. If not performed during operation (i.e., in presence of high magnetic fields and heat loads), the use of ellipsometry, validated by complementary non destructive techniques (such as LIBS), could still be a valid characterization technique and avoid the removal of PFCs for post mortem analysis (often destructive and expensive) after the experimental campaigns. For this reason, we believe our studies could offer a first attempt of using ellipsometry to characterize the exposed PFCs and study ion-surface interactions in order to improve our knowledge of physical processes such as He bubbles formation in W, oxide erosion and redeposition.

Finally, we would like to outline some perspectives that could be implemented to continue and improves the present studies. In particular:

1. *In-situ* ellipsometric measurements on W during D plasma exposure:
    - Manage to perform plasma exposures with no temperature rise using a chiller or a cooling system, in order to measure directly the effects of D plasma on W optical response.
    - Include the D surface inventory in a temperature-dependent Lorentz-Drude model of the W dielectric function, already developed by [80], in order to investigate on the physical nature of the interaction between implanted D atoms and W electrons.
2. *In-situ* ellipsometric measurements on W oxides during D plasma exposure:
    - Perform TEM measurements on the oxide sample exposed at low temperature, to observe the W-enriched and directly extract its thickness.
    - Once we are sure of the real thickness of the W-enriched layer, use ellipsometry to model its optical constants.
3. *In-situ* ellipsometric measurements on W during He plasma exposure:

- Build a more complete model that is able to explain the spectroscopic measurements. A collaboration with LSPM in Paris, that use FENICS code to model He bubbles growth kinetics, will soon start for this purpose.
- Perform TEM measurements of the He exposed samples, in order to measure the actual depth of the porous layer and the bubbles distribution over the whole layer.
- Perform SEM measurements introducing a small tilt, which would allow to obtain a 3D image of the surface and thus to probe possible roughness variations at a nanometric scale.
- Investigate on the He bubbles density on W crystalline orientation.

In addition, in the analysis of the reflectivity of our exposed and/or heated samples, little has been done to model the diffused component of reflectivity. In order to do so, as Bennet-Porteus model is limited to the situations in which $\sigma << \lambda$, other models such as Harvey-Stack approach [140], which uses Bidirectional Reflectance Distribution Function (BRDF) and improves the scattering prediction even for $\sigma \simeq \lambda$ and large scattering angles, could be implemented. Another approach could be Mueller matrix ellipsometry, used to quantify depolarization (percentage of light that has become unpolarized after reflection from the sample), which could be important in case of non uniform surfaces causing wide angular spread, and thus could allow to model the diffused component of reflectivity.

Bibliography

[1] "Advantages of fusion." https://www.materiel-metallographie.com/wp-content/uploads/2016/12/SAPHIR-520_-5Ja09w.pdf. Accessed: 2022-09-30.

[2] A. S. Eddington, "The internal constitution of the stars," in *A Source Book in Astronomy and Astrophysics, 1900–1975*, pp. 281–290, Harvard University Press, 1979.

[3] S. Atzeni, J. Meyer ter Vehn, *et al.*, *The physics of inertial fusion-Hydrodynamics, dense plasma physics, beam-plasma interaction*. Clarendon Press-Oxford University Press, 2004.

[4] S. E. Wurzel and S. C. Hsu, "Progress toward fusion energy breakeven and gain as measured against the lawson criterion," *Physics of Plasmas*, vol. 29, no. 6, 2022.

[5] J. D. Lawson, "Some criteria for a power producing thermonuclear reactor," *Proceedings of the physical society. Section B*, vol. 70, no. 1, p. 6, 1957.

[6] R. Aymar, P. Barabaschi, and Y. Shimomura, "The iter design," *Plasma Physics and Controlled Fusion*, vol. 44, p. 519, apr 2002.

[7] Y. Xu, "A general comparison between tokamak and stellarator plasmas," *Matter and Radiation at Extremes*, vol. 1, no. 4, pp. 192–200, 2016.

[8] G. Dubus, *From Plain Visualisation to Vibration Sensing: Using a Camera to Control the Flexibilities in the ITER Remote Handling Equipment (Doctoral Dissertation)*. PhD thesis, Tampere University of technology, 10 2014.

[9] X. Bonnin, R. Pitts, V. Komarov, F. Escourbiac, M. Merola, L. Bo, L. Wei, L. Pan, and A. Kukushkin, "Iter divertor plasma response to time-dependent impurity injection," *Nuclear Materials and Energy*, vol. 12, 03 2017.

[10] J. Roth, E. Tsitrone, A. Loarte, T. Loarer, G. Counsell, R. Neu, V. Philipps, S. Brezinsek, M. Lehnen, P. Coad, *et al.*, "Recent analysis of key plasma wall interactions issues for iter," *Journal of nuclear materials*, vol. 390, pp. 1–9, 2009.

[11] E. Tsitrone, C. Brosset, B. Pégourié, E. Gauthier, J. Bouvet, J. Bucalossi, S. Carpentier, Y. Corre, E. Delchambre, L. Desgranges, *et al.*, "Deuterium inventory in tore supra: reconciling particle balance and post-mortem analysis," *Nuclear Fusion*, vol. 49, no. 7, p. 075011, 2009.

[12] E. Lassner and W.-D. Schubert, *Tungsten: properties, chemistry, technology of the element, alloys, and chemical compounds*. Springer Science & Business Media, 2012.

[13] T. Tanabe, N. Noda, and H. Nakamura, "Review of high z materials for psi applications," *Journal of nuclear materials*, vol. 196, pp. 11–27, 1992.

[14] C. Ren, Z. Fang, M. Koopman, B. Butler, J. Paramore, and S. Middlemas, "Methods for improving ductility of tungsten - a review," *International Journal of Refractory Metals and Hard Materials*, vol. 75, pp. 170–183, 2018.

[15] G. Federici, C. H. Skinner, J. N. Brooks, J. P. Coad, C. Grisolia, A. A. Haasz, A. Hassanein, V. Philipps, C. S. Pitcher, J. Roth, *et al.*, "Plasma-material interactions in current tokamaks and their implications for next step fusion reactors," *Nuclear Fusion*, vol. 41, no. 12, p. 1967, 2001.

[16] M. Ialovega, E. Bernard, M.-F. Barthe, R. Bisson, A. Campos, M. Cabié, T. Neisius, R. Sakamoto, A. Kreter, C. Grisolia, *et al.*, "Helium-induced morphology evolution in tungsten under thermal treatment," *Nuclear Fusion*, vol. 62, no. 12, p. 126022, 2022.

[17] "Iaea. atomic and plasma-material interaction data for fusion, vienna, 2001." https://www.iaea.org/publications/4709/atomic-and-plasma-material-interaction-data-for-fusion. Accessed: 2024-01-30.

[18] M. Zibrov, M. Balden, T. Morgan, and M. Mayer, "Deuterium trapping and surface modification of polycrystalline tungsten exposed to a high-flux plasma at high fluences," *Nuclear Fusion*, vol. 57, no. 4, p. 046004, 2017.

[19] A. Haasz, M. Poon, and J. Davis, "The effect of ion damage on deuterium trapping in tungsten," *Journal of Nuclear Materials*, vol. 266, pp. 520–525, 1999.

[20] W. Wang, J. Roth, S. Lindig, and C. Wu, "Blister formation of tungsten due to ion bombardment," *Journal of nuclear materials*, vol. 299, no. 2, pp. 124–131, 2001.

[21] K. Ouaras, K. Hassouni, L. C. Delacqua, G. Lombardi, D. Vrel, and X. Bonnin, "Tungsten dust nanoparticles generation from blistering bursts under hydrogen environment in microwave ecr discharge," *Journal of Nuclear Materials*, vol. 466, pp. 65–68, 2015.

[22] D. Nishijima, M. Tokitani, D. Nagata, T. Schwarz-Selinger, A. Založnik, F. Chang, R. Doerner, M. Patino, M. Simmonds, M. Baldwin, *et al.*, "Deuterium supersaturated surface layer in tungsten: ion energy dependence," *Nuclear Fusion*, vol. 63, no. 12, p. 126003, 2023.

[23] L. Gao, W. Jacob, U. Von Toussaint, A. Manhard, M. Balden, K. Schmid, and T. Schwarz-Selinger, "Deuterium supersaturation in low-energy plasma-loaded tungsten surfaces," *Nuclear Fusion*, vol. 57, no. 1, p. 016026, 2016.

[24] R. Sakamoto, E. Bernard, A. Kreter, and N. Yoshida, "Surface morphology of tungsten exposed to helium plasma at temperatures below fuzz formation threshold 1073 k," *Nuclear fusion*, vol. 57, no. 1, p. 016040, 2016.

[25] L. Sedano, G. Esteban, M. Cavaro, E. Iraola, A. Abdulrahman, L. Batet, and M. Guasch, "The solubility of helium in lead–lithium eutectic alloy," *Nuclear Materials and Energy*, vol. 31, p. 101185, 2022.

[26] G. J. Thomas, "Experimental studies of helium in metals," *Radiation Effects*, vol. 78, no. 1-4, pp. 37–51, 1983.

[27] S. Kajita, W. Sakaguchi, N. Ohno, N. Yoshida, and T. Saeki, "Formation process of tungsten nanostructure by the exposure to helium plasma under fusion relevant plasma conditions," *Nuclear Fusion*, vol. 49, p. 095005, aug 2009.

[28] J. F. Ziegler, M. D. Ziegler, and J. P. Biersack, "Srim–the stopping and range of ions in matter (2010)," *Nuclear Instruments and Methods in Physics Research Section B: Beam Interactions with Materials and Atoms*, vol. 268, no. 11-12, pp. 1818–1823, 2010.

[29] C. Becquart, C. Domain, U. Sarkar, A. DeBacker, and M. Hou, "Microstructural evolution of irradiated tungsten: Ab initio parameterisation of an okmc model," *Journal of Nuclear Materials*, vol. 403, no. 1, pp. 75–88, 2010.

[30] K. O. Henriksson, K. Nordlund, A. Krasheninnikov, and J. Keinonen, "The depths of hydrogen and helium bubbles in tungsten: a comparison," *Fusion science and technology*, vol. 50, no. 1, pp. 43–57, 2006.

[31] W. Wilson, C. Bisson, and M. Baskes, "Self-trapping of helium in metals," *Physical Review B*, vol. 24, no. 10, p. 5616, 1981.

[32] C. M. Parish, H. Hijazi, H. Meyer, and F. W. Meyer, "Effect of tungsten crystallographic orientation on he-ion-induced surface morphology changes," *Acta Materialia*, vol. 62, pp. 173–181, 2014.

[33] K. D. Hammond, S. Blondel, L. Hu, D. Maroudas, and B. D. Wirth, "Large-scale atomistic simulations of low-energy helium implantation into tungsten single crystals," *Acta Materialia*, vol. 144, pp. 561–578, 2018.

[34] G. De Temmerman, K. Bystrov, J. J. Zielinski, M. Balden, G. Matern, C. Arnas, and L. Marot, "Nanostructuring of molybdenum and tungsten surfaces by low-energy helium ions," *Journal of Vacuum Science I& Technology A*, vol. 30, p. 041306, 06 2012.

[35] M. Baldwin, R. Doerner, W. Wampler, D. Nishijima, T. Lynch, and M. Miyamoto, "Effect of he on d retention in w exposed to low-energy, high-fluence (d, he, ar) mixture plasmas," *Nuclear Fusion*, vol. 51, no. 10, p. 103021, 2011.

[36] M. Shimada and C. N. Taylor, "Improved tritium retention modeling with reaction-diffusion code tmap and bulk depth profiling capability," *Nuclear Materials and Energy*, vol. 19, pp. 273–278, 2019.

[37] D. Nishijima, M. Patino, and R. Doerner, "Development of a libs system for in situ surface measurements during plasma exposure in pisces-a," *Review of Scientific Instruments*, vol. 89, no. 10, 2018.

[38] J. Yu, M. Baldwin, M. Simmonds, and A. Založnik, "Time-resolved laser-induced desorption spectroscopy (lids) for quantified in-situ hydrogen isotope retention measurement and removal from plasma facing materials," *Review of Scientific Instruments*, vol. 90, no. 7, 2019.

[39] X. Courtois, M. H. Aumeunier, C. Balorin, J. Migozzi, M. Houry, K. Blanckaert, Y. Moudden, C. Pocheau, A. Saille, E. Hugot, *et al.*, "Full coverage infrared thermography diagnostic for west machine protection," *Fusion Engineering and Design*, vol. 146, pp. 2015–2020, 2019.

[40] J. Gaspar, M.-H. Aumeunier, M. Le Bohec, F. Rigollet, S. Brezinsek, Y. Corre, X. Courtois, R. Dejarnac, M. Diez, L. Dubus, *et al.*, "In-situ assessment of the emissivity of tungsten plasma facing components of the west tokamak," *Nuclear Materials and Energy*, vol. 25, p. 100851, 2020.

[41] J. Gaspar, C. Pocheau, Y. Corre, N. Ehret, D. Guilhem, M. Houry, T. Loarer, T. Loewenhoff, C. Martin, C. Pardanaud, G. Pintsuk, M. Richou, F. Rigollet, H. Roche, G. Sepulcre, and M. Wirtz, "Emissivity measurement of tungsten plasma facing components of the WEST tokamak," *Fusion Engineering and Design*, vol. 149, p. 111328, Dec. 2019.

[42] G. De Temmerman, T. Hirai, and R. Pitts, "The influence of plasma-surface interaction on the performance of tungsten at the iter divertor vertical targets," *Plasma Physics and Controlled Fusion*, vol. 60, no. 4, p. 044018, 2018.

[43] G. Wright, H. Barnard, L. Kesler, E. Peterson, P. Stahle, R. Sullivan, D. Whyte, and K. Woller, "An experiment on the dynamics of ion implantation and sputtering of surfaces," *Review of Scientific Instruments*, vol. 85, no. 2, 2014.

[44] K. Hattar, D. C. Bufford, and D. L. Buller, "Concurrent in situ ion irradiation transmission electron microscope," *Nuclear Instruments and Methods in Physics Research Section B: Beam Interactions with Materials and Atoms*, vol. 338, pp. 56–65, 2014.

[45] "Saphir20." https://www.iter.org/sci/Fusion#:~:text=The%20following%20advantages%20make%20fusion,reactions%20(at%20equal%20mass). Accessed: 2021-12-02.

[46] "Presi resin." https://www.presi.com/en/product/pack-1-kg-de-poudre-500-cc-de-catalyseur-de-resine-km-back/. Accessed: 2024-07-02.

[47] "Electropolishing." https://www.substech.com/dokuwiki/doku.php?id=electropolishing. Accessed: 2024-03-08.

[48] Y. Addab, *WO_3 thin films formation, characterisation and ion bombardments of interest for magnetic fusion*. PhD thesis, Aix-Marseille Université, 2016.

[49] M. Ialovega, *Surface conditions of tungsten components: impact on hydrogen inventory*. PhD thesis, CEA Cadarache, 2021.

[50] F. Pappalardo, F. Romero Lairado, C. Louis de Canonville, C. Martin, G. Giacometti, G. Serin, E. Salomon, T. Angot, L. Gallais, R. Bisson, and M. Minissale, "Optical properties of tungsten: A parametric study to characterize the role of roughness, surface composition and temperature," *Optics*, vol. 3, no. 3, pp. 216–224, 2022.

[51] *Principles of Spectroscopic Ellipsometry*, ch. 4, pp. 81–146. John Wiley and Sons, Ltd, 2007.

[52] H. Tompkins and E. A. Irene, *Handbook of ellipsometry*. William Andrew, 2005.

[53] X. Yang, *Study of the hydrogen-tungsten interaction for fusion: measurement of the atomic reflection coefficient by laser spectroscopy*. PhD thesis, Aix-Marseille, 2017.

[54] G. Cartry, D. Kogut, K. Achkasov, J.-M. Layet, T. Farley, A. Gicquel, J. Achard, O. Brinza, T. Bieber, H. Khemliche, *et al.*, "Alternative solutions to caesium in negative-ion sources: a study of negative-ion surface production on diamond in h2/d2 plasmas," *New Journal of Physics*, vol. 19, no. 2, p. 025010, 2017.

[55] *Direct Current (DC) Sheaths*, ch. 6, pp. 165–206. John Wiley I& Sons, Ltd, 2005.

[56] J. A. Bittencourt, *Fundamentals of plasma physics*. Springer Science & Business Media, 2013.

[57] "Nist: Atomic spectra database." https://physics.nist.gov/PhysRefData/ASD/lines_form.html. Accessed: 2022-06-22.

[58] "S neox 3d optical profilometer." https://www.sensofar.com/metrology/industry-research/sneox/. Accessed: 2021-12-13.

[59] "Digital surf." https://www.digitalsurf.com/software-solutions/scanning-probe-microscopy/. Accessed: 2023-01-12.

[60] "Atomic force microscopy." https://en.wikipedia.org/wiki/Atomic_force_microscopy. Accessed: 2024-03-04.

[61] N. A. Geisse, "Afm and combined optical techniques," *Materials Today*, vol. 12, no. 7, pp. 40–45, 2009.

[62] J. I. Goldstein, D. E. Newbury, J. R. Michael, N. W. Ritchie, J. H. J. Scott, and D. C. Joy, *Scanning electron microscopy and X-ray microanalysis*. springer, 2017.

[63] M. Minissale, E. Salomon, F. Pappalardo, C. Martin, M. Muntwiler, T. Angot, and G. Le Lay, "The renaissance and golden age of epitaxial dry germanene," *Crystals*, vol. 13, no. 2, 2023.

[64] J. F. Moulder, *Handbook of X-ray Photoelectron Spectroscopy*, ch. 1. Perkin-Elmer Corporation, 1992.

[65] E. Salomon, M. Minissale, F. R. Lairado, S. Coussan, P. Rousselot-Pailley, F. Dulieu, and T. Angot, "Pyrene adsorption on a ag (111) surface," *The Journal of Physical Chemistry C*, vol. 125, no. 20, pp. 11166–11174, 2021.

[66] E. D. Palik, *Handbook of optical constants of solids*. Academic Press, 1991.

[67] "Relation between surface roughness and specular reflectance at normal incidence," *Journal of the Optical Society of America*, vol. 51, no. 2, pp. 123–129, 1961.

[68] *Principles of Spectroscopic Ellipsometry*, ch. 5, pp. 177–184. John Wiley and Sons, Ltd, 2007.

[69] R. Abernethy, "Predicting the performance of tungsten in a fusion environment: a literature review," *Materials Science and Technology*, vol. 33, no. 4, pp. 388–399, 2017.

[70] R. K. Freeman, F. A. Rigby, S. E. Doerr, L. E. Grimes, and D. B. Ward, "Reflectance of laser-damaged spacecraft thermal control materials," in *High-Power Laser Ablation*, vol. 3343, pp. 983–994, SPIE, 1998.

[71] E. Brodu, M. Balat-Pichelin, J.-L. Sans, and J. Kasper, "Evolution of the emissivity of tungsten at high temperature with and without proton bombardment," *Acta Materialia*, vol. 84, pp. 305–316, Feb. 2015.

[72] M. Balden, A. Manhard, M. Mayer, S. Elgeti, A. Kleyn, P. Z. Van Emmichoven, *et al.*, "Surface morphology and deuterium retention of tungsten after low-and high-flux deuterium plasma exposure," *Nuclear Fusion*, vol. 54, no. 8, p. 083014, 2014.

[73] E. Gao, W. Nadvornick, R. Doerner, and N. M. Ghoniem, "The influence of low-energy helium plasma on bubble formation in micro-engineered tungsten," *Journal of Nuclear Materials*, vol. 501, pp. 319–328, 2018.

[74] Q. Yang, Y. Huang, J. Sun, L. Liu, W. Ni, H. Fan, and D. Liu, "Surface degeneration of tungsten wires irradiated with low-energy (12–220 ev) helium ions," *Nuclear Instruments and Methods in Physics Research Section B: Beam Interactions with Materials and Atoms*, vol. 437, pp. 48–52, 2018.

[75] M. Ialovega, E. Bernard, R. Bisson, C. Martin, R. Sakamoto, A. Kreter, E. Hodille, T. Angot, and C. Grisolia, "Hydrogen trapping in tungsten: impact of helium irradiation and thermal cycling," *Physica Scripta*, vol. 2020, no. T171, p. 014066, 2020.

[76] C. Martin, M. Diez, A. Campos, M. Cabié, G. Giacometti, M. Balden, A. Gallo, B. Pegourié, E. Bernard, and E. Tsitrone, "First post-mortem analysis of deposits collected on ITER-like components in WEST after the C3 and C4 campaigns," *Physica Scripta*, vol. 96, p. 124035, Dec. 2021.

[77] J. Gaspar, Y. Corre, F. Rigollet, M.-H. Aumeunier, E. Bernard, S. Brezinsek, X. Courtois, R. Dejarnac, M. Diez, L. Dubus, *et al.*, "Overview of the emissivity measurements performed in west: in situ and post-mortem observations," *Nuclear Fusion*, vol. 62, no. 9, p. 096023, 2022.

[78] T. Matsumoto, A. Cezairliyan, and D. Basak, "Surface morphology and deuterium retention of tungsten after low-and high-flux deuterium plasma exposure," *International Journal of Thermophysics*, vol. 20, pp. 943–952, 1999.

[79] A. F. Borghesani and G. Carugno, "Temperature dependent polarization of the thermal radiation emitted by thin, hot tungsten wires," 2015.

[80] M. Minissale, C. Pardanaud, R. Bisson, and L. Gallais, "The temperature dependence of optical properties of tungsten in the visible and near-infrared domains: an experimental and theoretical study," *Journal of Physics D: Applied Physics*, vol. 50, p. 455601, Nov. 2017.

[81] L. Cao and K. Sendur, "Surface roughness effects on the broadband reflection for refractory metals and polar dielectrics," *Materials*, vol. 12, no. 19, p. 3090, 2019.

[82] Y. Fujii, "Influence of surface roughness on near-surface depth analysis from x-ray reflectivity measurements," *Surface and interface analysis*, vol. 42, no. 10-11, pp. 1642–1645, 2010.

[83] E. Brodu, M. Balat-Pichelin, J.-L. Sans, and J. Kasper, "Influence of roughness and composition on the total emissivity of tungsten, rhenium and tungsten–25% rhenium alloy at high temperature," *Journal of alloys and compounds*, vol. 585, pp. 510–517, 2014.

[84] M. Le Bohec, R. Steiner, H. Natsume, S. Kajita, M. B. Yaala, L. Marot, and M.-H. Aumeunier, "Relationship between topographic parameters and brdf for tungsten surfaces in the visible spectrum," *Optik*, p. 171750, 2024.

[85] H. Bolt, V. Barabash, G. Federici, J. Linke, A. Loarte, J. Roth, and K. Sato, "Plasma facing and high heat flux materials–needs for iter and beyond," *Journal of Nuclear Materials*, vol. 307, pp. 43–52, 2002.

[86] A. Manhard, M. Balden, and U. von Toussaint, "Blister formation on rough and technical tungsten surfaces exposed to deuterium plasma," *Nuclear Fusion*, vol. 57, p. 126012, Dec. 2017.

[87] G. M. Alonzo-Medina, A. González-González, J. L. Sacedón, and A. I. Oliva, "Understanding the thermal annealing process on metallic thin films," *IOP Conference Series: Materials Science and Engineering*, vol. 45, p. 012013, June 2013.

[88] I. Misumi, K. Sugawara, R. Kizu, A. Hirai, and S. Gonda, "Extension of the range of profile surface roughness measurements using metrological atomic force microscope," *Precision Engineering*, vol. 56, pp. 321–329, 2019.

[89] A. Krywonos, J. E. Harvey, and N. Choi, "Linear systems formulation of scattering theory for rough surfaces with arbitrary incident and scattering angles," *J. Opt. Soc. Am. A*, vol. 28, pp. 1121–1138, Jun 2011.

[90] M. Minissale, C. L. De Canonville, C. Pardanaud, B. Butoi, R. Bisson, and L. Gallais, "The role of defects, deuterium, and surface morphology on the optical response of beryllium," *Nuclear Fusion*, vol. 62, no. 5, p. 056012, 2022.

[91] "Nist: X-ray photoelectron spectroscopy database." https://srdata.nist.gov/xps/. Accessed: 2023-02-22.

[92] M. B. Johansson, B. Zietz, G. A. Niklasson, and L. Österlund, "Optical properties of nanocrystalline wo3 and wo3-x thin films prepared by dc magnetron sputtering," *Journal of Applied Physics*, vol. 115, no. 21, 2014.

[93] M. Yoshimizu, Y. Hotori, and H. Irie, "Ohmic hetero-junction of n-type silicon and tungsten trioxide for visible-light sensitive photocatalyst," *Journal of Materials Science and Chemical Engineering*, vol. 5, no. 8, pp. 33–43, 2017.

[94] C. Pardanaud, D. Dellasega, M. Passoni, C. Martin, P. Roubin, Y. Addab, C. Arnas, L. Couëdel, M. Minissale, E. Salomon, *et al.*, "Post-mortem analysis of tungsten plasma facing components in tokamaks: Raman microscopy measurements on compact, porous oxide and nitride films and nanoparticles," *Nuclear fusion*, vol. 60, no. 8, p. 086004, 2020.

[95] R. Pitts, S. Carpentier, F. Escourbiac, T. Hirai, V. Komarov, S. Lisgo, A. Kukushkin, A. Loarte, M. Merola, A. Sashala Naik, R. Mitteau, M. Sugihara, B. Bazylev, and P. Stangeby, "A full tungsten divertor for iter: Physics issues and design status," *Journal of Nuclear Materials*, vol. 438, pp. S48–S56, 2013. Proceedings of the 20th International Conference on Plasma-Surface Interactions in Controlled Fusion Devices.

[96] P. Moreau, J. Bucalossi, M. Missirlian, F. Samaille, X. Courtois, C. Gil, P. Lotte, O. Meyer, E. Nardon, R. Nouailletas, N. Ravenel, J. Travere, T. Alarcon, S. Antusch, M. Aumeunier, P. Barjat, S. Belsare, J. Bernard, M. Bhandarkar, C. Bottereau, C. Bourdelle, S. Brémond, Y. Camenen, V. Chaudhari, C. Chavda, M. Chernyshova, F. Clairet, J. Colnel, T. Czarski, M. Choi, G. Colledani, Y. Corre, R. Daniel, D. Davis, R. Dejarnac, P. Devynck, J. Dhongde, D. Douai, D. Elbeze, A. Escarguel, C. Fenzi, W. Figacz, Z. Guangwu, J. Giacalone, R. Guirlet, J. Gunn, S. Hacquin, X. Hao, J. Harris, G. Hoang, M. Houry, F. Imbeaux, S. Jablonski, A. Jardin, H. Joshi, G. Kasprowicz, C. Klepper, E. Kowalska-Strzeciwilk, M. Kubkowska, A. Kumar, V. Kumar, P. Kumari, H. Laqua, A. LeLuyer, W. Lee, M. Lewerentz, B. Lyu, P. Malard, L. Manenc, I. Mansuri, Y. Marandet, H. Masand, D. Mazon, D. Molina, G. Moureau, Y. Nam, H. Park, J. Pascal, K. Patel, M. Patel, K. Pozniak, D. Radloff, S. Ranjan, C. Rapson, G. Raupp, M. Rieth, R. Sabot, B. Santraine, D. Sestac, M. Sharma, J. Shen, J. Signoret, J. Soni, A. Spring, P. Spuig, R. Sugandhi, W. Treuterrer, E. Tsitrone, S. Varshney, S. Vartanian, D. Volpe, F. Wang, A. Werner, G. Yun, W. Zabolotny, and W. Zhao, "Measurements and controls implementation for west," *Fusion Engineering and Design*, vol. 123, pp. 1029–1032, 2017. Proceedings of the 29th

Symposium on Fusion Technology (SOFT-29) Prague, Czech Republic, September 5-9, 2016.

[97] T. J. Kim, T. H. Ghong, Y. D. Kim, D. E. Aspnes, M. V. Klein, D.-S. Ko, Y.-W. Kim, V. C. Elarde, and J. J. Coleman, "Investigation of effective-medium approximation, alloy, average-composition, and graded-composition models for interface analysis by spectroscopic ellipsometry," *Journal of Applied Physics*, vol. 102, p. 063512, Sept. 2007.

[98] F. Kaïl, A. Fontcuberta I Morral, A. Hadjadj, P. Roca I Cabarrocas, and A. Beorchia, "Hydrogen-plasma etching of hydrogenated amorphous silicon: a study by a combination of spectroscopic ellipsometry and trap-limited diffusion model," *Philosophical Magazine*, vol. 84, pp. 595–609, Feb. 2004.

[99] P. Y. Kuryoz, L. V. Poperenko, and V. G. Kravets, "Correlation between dielectric constants and enhancement of surface plasmon resonances for thin gold films: Surface plasmon resonances for thin Au films," *physica status solidi (a)*, vol. 210, pp. 2445–2455, Nov. 2013.

[100] I. Valyukh, S. Green, H. Arwin, G. Niklasson, E. Wäckelgård, and C. Granqvist, "Spectroscopic ellipsometry characterization of electrochromic tungsten oxide and nickel oxide thin films made by sputter deposition," *Solar Energy Materials and Solar Cells*, vol. 94, pp. 724–732, May 2010.

[101] M. Horprathum, P. Chindaudom, P. Limnonthakul, P. Eiamchai, N. Nuntawong, V. Patthanasettakul, A. Pokaipisit, and P. Limsuwan, "Dynamic *in situ* spectroscopic ellipsometric study in inhomogeneous TiO2 thin-film growth," *Journal of Applied Physics*, vol. 108, p. 013522, July 2010.

[102] P. Janicek, M. Putri, K. H. Kim, H. J. Lee, M. Bouska, S. Šlang, and H. Y. Lee, "Spectroscopic Ellipsometry Characterization of As-Deposited and Annealed Non-Stoichiometric Indium Zinc Tin Oxide Thin Film," *Materials*, vol. 14, p. 578, Jan. 2021.

[103] A. Sato, S. Sekine, and M. Ohkawa, "Measurement of Complex Refractive Index of Tungsten by Using Ellipsometry," *IEEJ Transactions on Fundamentals and Materials*, vol. 124, no. 2, pp. 114–119, 2004.

[104] D. E. Aspnes, J. B. Theeten, and F. Hottier, "Investigation of effective-medium models of microscopic surface roughness by spectroscopic ellipsometry," *Physical Review B*, vol. 20, pp. 3292–3302, Oct. 1979.

[105] J. Y. Jung, "OPTICAL MODELING OFF-STOICHIOMETRIC AMORPHOUS AL2O3 THIN FILMS DEPOSITED BY REACTIVE SPUTTERING,"

[106] T. Gu, E.-T. Hu, S. Guo, Y. Wu, J. Wang, Z.-Y. Wang, K.-H. Yu, W. Wei, Y.-X. Zheng, S.-Y. Wang, and L.-Y. Chen, "Ellipsometric study on optical properties of hydrogen plasma-treated aluminum-doped ZnO thin film," *Vacuum*, vol. 163, pp. 69–74, May 2019.

[107] T. Dittmar, A. Kreter, and A. von Keudell, "Development of an in situ ellipsometer for deposition and erosion studies at the first wall of a tokamak," *Nuclear Fusion*, vol. 49, p. 045004, Apr. 2009.

[108] E. Hodille, X. Bonnin, R. Bisson, T. Angot, C. Becquart, J. Layet, and C. Grisolia, "Macroscopic rate equation modeling of trapping/detrapping of hydrogen isotopes in tungsten materials," *Journal of Nuclear Materials*, vol. 467, pp. 424–431, Dec. 2015.

[109] E. Hodille, F. Ghiorghiu, Y. Addab, A. Založnik, M. Minissale, Z. Piazza, C. Martin, T. Angot, L. Gallais, M.-F. Barthe, *et al.*, "Retention and release of hydrogen isotopes in tungsten plasma-facing components: the role of grain boundaries and the native oxide layer from a joint experiment-simulation integrated approach," *Nuclear Fusion*, vol. 57, no. 7, p. 076019, 2017.

[110] C. Martin, H. Hijazi, Y. Addab, B. Domenichini, M. E. Bannister, F. W. Meyer, C. Pardanaud, G. Giacometti, M. Cabié, and P. Roubin, "Tungsten oxide thin film bombarded with a low energy He ion beam: evidence for a reduced erosion and W enrichment," *Physica Scripta*, vol. T170, p. 014019, Dec. 2017.

[111] S. Yih and C. Wang, "Tungsten: Sources, metallurgy, properties, and applications, 1979."

[112] K. Schlueter and M. Balden, "Dependence of oxidation on the surface orientation of tungsten grains," *International Journal of Refractory Metals and Hard Materials*, vol. 79, pp. 102–107, 2019.

[113] R. Bringans, H. Höchst, and H. Shanks, "Defect states in w o 3 studied with photoelectron spectroscopy," *Physical Review B*, vol. 24, no. 6, p. 3481, 1981.

[114] H. Camirand, B. Baloukas, J. E. Klemberg-Sapieha, and L. Martinu, "In situ spectroscopic ellipsometry of electrochromic amorphous tungsten oxide films," *Solar Energy Materials and Solar Cells*, vol. 140, pp. 77–85, Sept. 2015.

[115] M. Lagier, A. Bertinotti, O. Bouvard, L. Burnier, and A. Schüler, "Optical properties of in vacuo lithiated nanoporous wo3: Mo thin films as determined by spectroscopic ellipsometry," *Optical Materials*, vol. 117, p. 111091, 2021.

[116] V. Alimov, B. Tyburska, M. Balden, S. Lindig, J. Roth, K. Isobe, and T. Yamanishi, "Surface morphology and deuterium retention in tungsten oxide layers exposed to low-energy, high flux D plasma," *Journal of Nuclear Materials*, vol. 409, pp. 27–32, Feb. 2011.

[117] H. Tu, C. Li, W. Ding, L. Shi, and Y. Zhang, "The erosion and retention properties of tungsten trioxide films exposed to low energy deuterium ions: Temperature dependence," *Journal of Nuclear Materials*, vol. 562, p. 153590, 2022.

[118] Y. Addab, C. Martin, C. Pardanaud, J. Khayadjian, K. Achkasov, D. Kogut, G. Cartry, G. Giacometti, M. Cabié, J. L. Gardarein, and P. Roubin, "Formation of thin tungsten oxide layers: characterization and exposure to deuterium," *Physica Scripta*, vol. T167, p. 014036, Feb. 2016.

[119] K. Kremer, T. Schwarz-Selinger, and W. Jacob, "Influence of thin tungsten oxide films on hydrogen isotope uptake and retention in tungsten – Evidence for permeation barrier effect," *Nuclear Materials and Energy*, vol. 27, p. 100991, June 2021.

[120] K. Kremer, T. Schwarz-Selinger, and W. Jacob, "Deuterium plasma exposure of thin oxide films on tungsten-oxygen removal and deuterium uptake," *Nuclear Materials and Energy*, vol. 35, p. 101406, 2023.

[121] M. Daniel, B. Desbat, J. Lassegues, B. Gerand, and M. Figlarz, "Infrared and raman study of wo3 tungsten trioxides and wo3, xh2o tungsten trioxide tydrates," *Journal of Solid State Chemistry*, vol. 67, no. 2, pp. 235–247, 1987.

[122] K. Hong, M. Xie, R. Hu, and H. Wu, "Synthesizing tungsten oxide nanowires by a thermal evaporation method," *Applied physics letters*, vol. 90, no. 17, 2007.

[123] A. D. Rakić, A. B. Djurišić, J. M. Elazar, and M. L. Majewski, "Optical properties of metallic films for vertical-cavity optoelectronic devices," *Applied optics*, vol. 37, no. 22, pp. 5271–5283, 1998.

[124] D. P. Kulikova, A. A. Dobronosova, V. V. Kornienko, I. A. Nechepurenko, A. S. Baburin, E. V. Sergeev, E. S. Lotkov, I. A. Rodionov, A. V. Baryshev, and A. V. Dorofeenko, "Optical properties of tungsten trioxide, palladium, and platinum thin films for functional nanostructures engineering," *Optics express*, vol. 28, no. 21, pp. 32049–32060, 2020.

[125] M. Guseva, A. Suvorov, S. Korshunov, and N. Lazarev, "Sputtering of beryllium, tungsten, tungsten oxide and mixed w–c layers by deuterium ions in the near-threshold energy range," *Journal of nuclear materials*, vol. 266, pp. 222–227, 1999.

[126] A. Dunand, M. Minissale, T. Angot, and R. Bisson, "Flux dependence of helium retention in clean w (1 1 0): Experimental evidence for he self-trapping," *Nuclear Materials and Energy*, vol. 34, p. 101324, 2023.

[127] P. Lhuillier, T. Belhabib, P. Desgardin, B. Courtois, T. Sauvage, M. Barthe, A. Thomann, P. Brault, and Y. Tessier, "Trapping and release of helium in tungsten," *Journal of Nuclear Materials*, vol. 416, no. 1, pp. 13–17, 2011. Nuclear Materials IV.

[128] F. Sefta, N. Juslin, and B. D. Wirth, "Helium bubble bursting in tungsten," *Journal of Applied Physics*, vol. 114, p. 243518, 12 2013.

[129] L. Sandoval, D. Perez, B. P. Uberuaga, and A. F. Voter, "Formation of helium-bubble networks in tungsten," *Acta Materialia*, vol. 159, pp. 46–50, 2018.

[130] R. W. Harrison, G. Greaves, J. Hinks, and S. Donnelly, "A study of the effect of helium concentration and displacement damage on the microstructure of helium ion irradiated tungsten," *Journal of Nuclear Materials*, vol. 495, pp. 492–503, 2017.

[131] F. Zhu, D. Wang, W. Wang, J. Wu, X. Ma, Z. Xie, and Z. Zhang, "Microstructure and mechanical property evolution of he-implanted nanochannel w film under post-annealing," *Journal of Nuclear Materials*, vol. 572, p. 154065, 2022.

[132] L. Corso, S. Curiotto, E. Bernard, M. Cabie, C. Martin, L. Martinelli, F. Cheynis, P. Muller, and F. Leroy, "Tungsten evolution under helium irradiation: Shape of bubbles by tem and in-situ gisaxs analysis," *Nuclear Materials and Energy*, vol. 37, p. 101533, 2023.

[133] C.-S. Wong, J. A. Whaley, T. Wada, S. Harayama, Y. Oya, and R. D. Kolasinski, "Changes in surface morphology of helium-induced tungsten nanostructure during high-temperature annealing," *Nuclear Materials and Energy*, vol. 22, p. 100730, 2020.

[134] R. D. Kolasinski, C.-S. Wong, J. A. Whaley, and F. I. Allen, "In-situ spectroscopic ellipsometry for real-time characterization of the effects of high-flux helium plasmas on tungsten surfaces," tech. rep., Sandia National Lab.(SNL-CA), Livermore, CA (United States), 2020.

[135] R. D. Kolasinski, C.-S. Wong, A. Engel, J. A. Whaley, F. I. Allen, and D. A. Buchenauer, "Deciphering the influence of high-flux helium plasma exposure on tungsten nanostructure growth using real-time, in situ spectroscopic ellipsometry," *Journal of Applied Physics*, vol. 131, no. 6, 2022.

[136] Q. Xu, T. Yoshiie, and H. Huang, "Molecular dynamics simulation of vacancy diffusion in tungsten induced by irradiation," *Nuclear Instruments and Methods in Physics Research Section B: Beam Interactions with Materials and Atoms*, vol. 206, pp. 123–126, 2003.

[137] C. Chase, E. Maxwell, and W. Millett, "The dielectric constant of liquid helium," *Physica*, vol. 27, no. 12, pp. 1129–1145, 1961.

[138] J. W. Schmidt and M. R. Moldover, "Dielectric permittivity of eight gases measured with cross capacitors," *International Journal of Thermophysics*, vol. 24, pp. 375–403, 2003.

[139] M. Krychowiak, "Spectral in situ ellipsometer for thin layer measurements in thermonuclear fusion applications," *Review of Scientific Instruments*, vol. 95, p. 113511, 11 2024.

[140] J. E. Harvey, N. Choi, and A. Krywonos, "Scattering from moderately rough interfaces between two arbitrary media," in *Optical System Contamination: Effects, Measurements, and Control 2010*, vol. 7794, pp. 218–228, SPIE, 2010.

List of Figures

1 Représentation schématique des composants du tokamak ITER. vi

2 Représentation schématique d'un monoblock en W, sa taille caractéristique et sa position dans la structure du divertor. viii

3 Lignes de vue de l'endoscope supérieur dans le tokamak WEST (a) et image IR de la zone du divertor lors d'une décharge plasma (b). x

1.1 Triple products $n_{i0}T_{i0}\tau_E^*$ and $n < T_i >_n \tau$ (for inertial confinement devices and magnetic confinement devices, respectively) reached by different reactors vs year achieved, from Wurzel et al. [4]. 3

1.2 Schematics of two magnetic confinement configuration [7]: tokamak (a) and stellerator (b). 4

1.3 Schematics of ITER tokamak components [8]. 5

1.4 Schematic picture of a W monoblock, its characteristic dimensions and its location in the divertor structure [9]. 5

1.5 SEM images of He irradiated tungsten samples with different fluences and temperatures, from [24]. 7

1.6 Upper port endoscope fields of view in the tokamak WEST (a) and IR image of the divertor area during a plasma pulse [39]. 9

2.1 Schematic diagram of the electro-chemical polishing process [47]. 14

2.2 A schematic representation of the experimental set-up CAsPEr used for thermal oxidation [49]. 15

2.3 Schematic of the experimental setup: HPL, high power laser; SCL, supercontinuum laser; P, polarizer; BS, beam splitter; M1 and M2, fixed and removable silver mirrors, respectively; IS1 and IS2, integrating spheres of reference and sample side, respectively; FS1 and FS2, fiber-optic spectrometers connected to IS1 and IS2, respectively. 16

2.4 Calibration curves of HPL power with respect to a calorimeter (a) and of the pyrometer temperature with respect to a thermocouple (b). . . . 17

2.5 Schematic representation of the measurement principle of ellipsometry [51]. 18

2.6 Ellipsometer source and detector units installed on the plasma chamber. 19

2.7 CAMITER experimental set-up: plasma chamber, load-lock chamber for samples insertion, capacitance matching box and pyrometer. 21

2.8 Schematic representation of: the W on Si(100) wafer with the W sample placed on top (a) and the stainless steel wafer with the holes to fix the sample (b). 21

2.9 Typical I-V curve obtained with a Langmuir probe (in this case, for D plasma). 22

2.10 Ion flux plots as a function of power and pressure for D (a,c) and He (b,d) plasma. The points refer to the experimental data while the solid lines refer to a linear fit (in the case of the power plots) and a logarithmic fit (in the case of the pressure plots). 24
2.11 Ion energy plots as a function of power and pressure for D (a,c) and He (b,d) plasma. 25
2.12 Contribution of H^+, H_2^+ and H_3^+ to the total ion population, as a function of pressure (a) and power (b), for two gas temperatures [53]. . 26
2.13 Schematic image of S-neox SENSOFAR Confocal microscopy instrumental set-up [58]. 27
2.14 An example of CM images of a W sample: raw image (a) and corrected image with roughness parameters table (b). 28
2.15 A simplified scheme of AFM instrumental set-up [60]. 29
2.16 An example of AFM images of a W sample: raw (a) and corrected (b) image. 30
2.17 SEM image in BSE mode (a) and SE mode (b) of a thin Au film on Ge(111) surface upon annealing [63]. 32
2.18 SEM images of a He exposed W surface acquired by different detectors: SE image (a) and EBSD pattern (b). 32
2.19 Cross-section SEM view of WO_3 layer on W substrate (with the Pt protection layer on top). 33
2.20 Example of a fit of the XPS spectrum of the W 4f peaks of a WO_3 sample. 35
2.21 Optical model for an air/thin film/substrate structure [51]. 36
2.22 Schematic depiction of the EMA layer. 37

3.1 RMS roughness AFM (a) and CM (b) measurements as a function of samples etching time, before and after the annealing. 41
3.2 AFM images of samples W1 (a, b), W3 (c, d) and W5 (e, f), before (left) and after (right) annealing. 42
3.3 Experimental reflectivity spectra measured at room temperature (solid lines) for unpolarized light before (green) and after laser annealing (blue), and theoretical curves (dashed lines) obtained with equation 2.25. 43
3.4 Percent weight of the diffused component on the total reflectivity (obtained from Bennet-Porteus model) as a function of wavelength, for the 5 samples, before (solid curves) and after (dashed curves) the annealing. For W2 and W3, solid and dashed curves overlap, as their roughness is unchanged after the annealing. 44
3.5 Relative reflectivity variation (with respect to the RT curve) at 840 nm as a function of temperature, during the first annealing (black squares) and the second and third ones (averaged, open red circles). Each point was obtained by averaging over the five samples, the error bar being the standard deviation. 44
3.6 Relative reflectivity variation (with respect to room temperature measurement) at 600 nm (a) and 1000 nm (b) as a function of the samples temperature, during first annealing (black squares) and during second and third annealing (averaged, open red circles). 45

3.7 XPS spectra of sample W5 as a function of binding energy, showing the core levels of W 4f (a), C 1s and K 2p (b), N 1s (c), and O 1s (d) before (green open circles) and after annealing (blue squares). 46

4.1 Ψ and Δ relative variation at 450 nm (a) and 950 nm (b) as a function of time. The plasma starts at t=0 min. and stops at t=10 min. 50

4.2 Ψ and Δ relative variation at 850 nm (blue curves, left scale) and simultaneous W surface temperature (black curve, right scale) as a function of time. 50

4.3 W reflectivity spectra calculated from ellipsometric measurements during oven annealing, for 9 temperatures in the range 300 K (RT)-773 K. 51

4.4 Absolute variation of Ψ caused by D plasma during "dark" measurement, as a function of wavelength (a) and as a function of time for two wavelengths (b), together with the temporal evolution of the signal intensity (integrated over the whole wavelength range). The plasma takes place between t=1.5 min. and t=2.5 min. 52

4.5 W reflectivity relative variation at 850 nm (with respect to the initial value, before plasma) as a function of time. 53

4.6 Comparison of reflectivity relative variation at 850 nm as a function of temperature (during plasma exposure and during annealing) and correspondent temperature ramps, respectively for the oven annealing (a,c) and for the laser annealing (b,d). 54

4.7 Reflectivity relative variation at 850 nm as a function of temperature, during plasma exposure (green full dots), during the cooling phase as the plasma is off (green empty dots) and during laser annealing and cooling phase, averaged (red empty dots). 55

4.8 Reflectivity relative variation at 850 nm as a function of temperature due to the interaction with D ions, calculated as the subtraction of annealing measurement (red curve of figure 4.7) from the plasma measurement (green curve of figure 4.7). 55

4.9 Reflectivity relative variation (with respect to the initial value, without plasma and at room temperature) as a function of wavelength, during plasma exposure (green curve), during annealing (red curve) and caused by interactions with D ions (orange curve, derived from a subtraction of the red curve from the green one), for four moments of the plasma implantation, respectively at 410 K, 450 K, 500 K and 600 K. 56

4.10 Schematics (not in scale) of D atoms implantation, diffusion range and light penetration depth in W (a); light penetration depth in W as a function of wavelength (b). 59

4.11 D total inventory (left scale) and W surface temperature (right scale), as a function of time. The plasma starts at t=0 min. and ends at t=10 min. 60

4.12 D surface inventory in the light penetration depth (left scale) and surface temperature (right scale), as a function of time. The plasma starts at t=0 min. and ends at t=10 min. 60

4.13 D surface inventory in the light penetration depth (green curve, left scale) and reflectivity relative variation at 850 nm measured with ellipsometry (orange curve, right scale), both as a function of surface temperature during plasma implantation phase. 61

4.14 (a) Reflectivity relative variation at 850 nm as a function of temperature, during plasma exposure performed at 673 K (green full dots) and during the cooling phase as the plasma is off (green empty dots). (b) D total and (c) surface inventory (left scale) and W surface temperature (right scale), as a function of time, during the plasma exposure at 673 K. The plasma starts at t=0 min. and ends at t=10 min. 63

5.1 FIB-SEM section images of Wox1 (a) and Wox2 (c) samples, before plasma exposure, and their correspondent confocal microscopy images on the right (b,d). 67

5.2 Raman spectra of the two samples Wox1 and Wox2, as-synthetized. . . 68

5.3 SEM images (secondary electron mode) of the sample Wox2 before D plasma exposure, at magnification 50k (a) and 75k (b). 68

5.4 Refractive index n (a) and extinction coefficient k (b) of the sample Wox1 before and after plasma exposure, and comparison with the typical indexes values of ideal WO_3 and W (retrieved from Kulikova et al.[124] and Rakic et al.[123], respectively). 69

5.5 Plots of Wox1 experimental (solid lines) and model (dashed lines) Ψ (a) and Δ (b), as a function of time during D plasma exposure (starting at t=0 min. and ending at t=10 min.), for 5 different wavelengths. 70

5.6 EMA percentage (of the metallic WO_x layer) of sample Wox1 as a function of time. 71

5.7 Wox1 after D plasma exposure: FIB-SEM image (a) and confocal microscopy image (b). 71

5.8 Optical indexes n and k of sample Wox2 as a function of wavelength after different plasma exposures (e.g., with increasing cumulated fluence)„ assuming that the oxide layer is homogeneous. These indexes are compared with the ones of ideal WO_3 and W (from Kulikova et al.[124] and Rakic et al.[123], respectively) and of the exposed sample Wox1. 72

5.9 Top: XPS spectra of Wox2 for different values of cumulated D fluence. Bottom: Histogram representing the peaks predominance in XPS spectra for each value of cumulated fluence, going from highest binding energy (W^{6+}) to the lowest (W^{4+}), to finally metallic W. 73

5.10 Example of fit of W 4f peaks relative to the XPS spectrum of the sample Wox2, exposed at a D ion fluence of $8.5 \times 10^{23} D^+ \cdot m^{-2}$, and corresponding table containing the binding energy of each peak. 74

5.11 FIB-SEM images of Wox2 before (a) and after (b) D plasma exposure. 74

5.12 Schematic representation of the stack layer model (a) used to fit the W-enriched layer thickness (b) and the optical indexes n,k of the underlying layer WOx (c,d). 75

6.1 Emission spectrum of He plasma contaminated with oxygen, evidenced by the line at 777.4 nm (a); pictures of W sample before (b) and after (c) exposure to the contaminated He plasma. 78
6.2 SEM images (secondary electron mode) of the samples GFW2 (a) and GFW5 (b), before He plasma exposure. 80
6.3 ImageJ analysis routine of a SEM image: raw image (a), after applying FFT band pass filter (b), after applying the threshold (c), after applying the watershed routine on the binary image (d). 81
6.4 SEM images of the sample GFW1 exposed at 673 K on a smooth area of the surface (a) and at the border between a smooth and a rough area (b). We specify that in this case a statistical analysis was not possible, since the bubbles size was too close to the instrument resolution (1-2 nm). 82
6.5 EBSD map of GFW1 surface, between a rough and a smooth surface (inside the red square), which do not show a specific difference in crystallographic direction. 83
6.6 SEM images of the sample GFW2, exposed at 823 K, and relative statistics on He bubbles: grain (100) (a,b) and grain (111) (c,d). 83
6.7 SEM images of the sample GFW3 (exposed at 973 K): at magnification 20k (a); of the area in the red square at magnification 80k (b). Relative statistics on He bubbles: grain (100) (c) and grain (111) (d). 84
6.8 SEM images of the sample GFW4, exposed at 973 K and higher flux, and relative statistics on He bubbles: grain (100) (a,b) and grain (111) (c,d). 85
6.9 EBSD map of the exposed sample GFW4, with marks on the area between the two grains, where the SEM images in figure 6.8 was taken. . 85
6.10 SEM images of the sample GFW5, recrystallized and exposed at 973 K, and relative statistics on He bubbles: grain (100) (a,b) and grain (111) (c,d). 86
6.11 Comparison of the reflectivity spectra of W samples before plasma exposure and: the samples GFW1, GFW2 and GFW3 exposed at 673 K, 823 K and 973 K, respectively (a); the sample GFW4 exposed at 973 K to an ion flux higher by a factor 2 (b); of GFW5, exposed at 973 K and previously recrystallized (c). 88
6.12 Reflectivity variation calculated from the *in-situ* ellipsometric data during He plasma exposure for the sample GFW1 (a), GFW2 (b), GFW3 (c), GFW4 (d) and GFW5 (e), considering an error bar on temperature values of ±30 K. The solid lines refer to the experimental data at different wavelengths, while the dashed lines refer to the correspondent model. 89
6.13 Variation of porosity (a) and roughness (b) as a function of He fluence, for the samples GFW1, GFW2, GFW3 and GFW5. The points correspond to the experimental values of porosity (extracted by SEM images) and roughness (measured with AFM), and their correspondent error bars. 91

7.1 Reverse ellipsometric configuration implemented by Dittmar et al. [107] in TEXTOR. 97

List of Tables

1.1 Main physical properties of W [12]. 6

2.1 Table resuming the five steps of mechanical polishing of W samples. . . 13

4.1 Table resuming the reflectivity relative variation during plasma, during annealing and due to D ions, during four temperatures of the implantation phase (410, 450, 500 and 600 K), in percentage. 57

5.1 Experimental parameters of the samples oxidation process (temperature, oxygen pressure and time), the thickness of the oxide layer before plamsa exposure and the plasma conditions (ion flux, fluence and temperature). *This is a value of cumulated fluence that was reached with an average ion fluence of $5.5 \times 10^{22} D^{+} \cdot m^{-2}$ for each exposure. 66

6.1 Table resuming the experimental parameters of the He plasma exposure and previous W surface state of the samples. "P" is for "polished" and "R" is for recrystallized. 79

6.2 Table representing the parameters of the model used to fit the *in-situ* reflectivity data. 91